Universitá degli studi di Pisa
Facoltá di Scienze M. F. N.
Corso di laurea in Fisica
a.a. 1990/91

TESI DI LAUREA:

**Emilio Meschi**

Under the supervision of dr. **Mauro Dell'Orso**

# A Study of QCD radiation in jet events at the Fermilab $p\bar{p}$ collider

University of Pisa, "laurea" thesis; November 20, 1991

# Contents

**1 Theoretical Frame** **1**

1.1 Introduction . . . . . . . . . . . . . . . . . . . . . . . . . . . . 1

1.2 High energy hadron-hadron collisions . . . . . . . . . . . . . . . . . . 2

1.2.1 Structure functions . . . . . . . . . . . . . . . . . . . . . . . . 9

1.3 Description of higher order processes: Shower Montecarlos versus Parton Level Calculations . . . . . . . . . . . . . . . . . . . . . . . 10

**2 The Collider Detector at Fermilab** **14**

2.1 Calorimetry . . . . . . . . . . . . . . . . . . . . . . . . . . . . 15

2.2 Tracking system . . . . . . . . . . . . . . . . . . . . . . . . . . 20

2.3 Beam-Beam Counters . . . . . . . . . . . . . . . . . . . . . . . . 22

2.4 Trigger and data acquisition structure . . . . . . . . . . . . . . . . 23

2.4.1 General architecture of the data acquisition . . . . . . . . . . 23

2.4.2 Level 0 . . . . . . . . . . . . . . . . . . . . . . . . . . . . 24

2.4.3 Level 1 . . . . . . . . . . . . . . . . . . . . . . . . . . . . 25

2.4.4 Level 2 . . . . . . . . . . . . . . . . . . . . . . . . . . . . 25

2.4.5 Level 3 . . . . . . . . . . . . . . . . . . . . . . . . . . . . 27

**3 Jets at CDF** **28**

3.1 Jet reconstruction . . . . . . . . . . . . . . . . . . . . . . . . . 28

3.1.1 Clustering algorithms . . . . . . . . . . . . . . . . . . . . . 28

3.1.2 Jet energy resolution . . . . . . . . . . . . . . . . . . . . . . 32

3.1.3 Energy scale . . . . . . . . . . . . . . . . . . . . . . . . . . 34
3.2 Data selection and simulated samples . . . . . . . . . . . . . . . . . 40
3.2.1 Data Sample . . . . . . . . . . . . . . . . . . . . . . . . . . 40
3.2.2 Background study . . . . . . . . . . . . . . . . . . . . . . . . 43
3.2.3 Kinematic cuts . . . . . . . . . . . . . . . . . . . . . . . . . . 48
3.2.4 Simulated samples . . . . . . . . . . . . . . . . . . . . . . . . 50
3.2.5 Simulated events vs. real data . . . . . . . . . . . . . . . . . . 53

**4 Effects of QCD radiation on jet measurements 55**
4.1 Importance of radiation . . . . . . . . . . . . . . . . . . . . . . . . 55
4.2 Spatial correlation between radiated energy and final state partons . 59
4.3 The influence of radiation on the dijet invariant mass . . . . . . . . . 62
4.4 Gluon radiation in the measurement of $\frac{d\sigma}{dM_{jj}}$ . . . . . . . . . . . . . . 66
4.4.1 Dependence on the cone size . . . . . . . . . . . . . . . . . . . 66
4.4.2 Predictions compared to data on absolute scale . . . . . . . . 70
4.5 Conclusions . . . . . . . . . . . . . . . . . . . . . . . . . . . . . . 72

**5 Interference effects in QCD radiation 74**
5.1 Colour topology and interference in the QCD processes . . . . . . . 74
5.1.1 Coloured Feynman diagrams and interference . . . . . . . . . 76
5.1.2 The interference pattern: angular distribution of bremsstrahlung gluons. Herwig and Isajet . . . . . . . . . . . . . . . . . . 78
5.2 A study of radiation by means of the third jet . . . . . . . . . . . . . 83
5.2.1 Kinematic variables for the description . . . . . . . . . . . . . 83
5.2.2 Data sample and selection cuts . . . . . . . . . . . . . . . . . 83
5.2.3 Simulated samples . . . . . . . . . . . . . . . . . . . . . . . . 85
5.2.4 Angular distribution of the third jet around the second jet: the $R, \alpha$ space . . . . . . . . . . . . . . . . . . . . . . . . 93

5.2.5 Study of $R$, the distance between the $3^{rd}$ jet and the $2^{nd}$ jet in the $\eta, \phi$ space . . . . . . . . . . . . . . . . . . . . . . . . . 96

5.2.6 A variable sensitive to the colour interference . . . . . . . . . . 101

5.2.7 Comparison of the measured $\alpha$ distribution with the Herwig and Isajet simulations . . . . . . . . . . . . . . . . . . . . . . . 101

5.2.8 Sensitivity to $R_{cone}$ and to the $\Delta\phi$ cut . . . . . . . . . . . . . . 105

5.2.9 Selection of coherent and incoherent hard subprocesses: $\alpha$ distributions for selected samples . . . . . . . . . . . . . . . . 109

5.2.10 Pseudorapidity of the third jet . . . . . . . . . . . . . . . . . . 112

5.2.11 Quarks and gluons in the $\alpha$ spectrum . . . . . . . . . . . . . 112

5.3 Conclusions . . . . . . . . . . . . . . . . . . . . . . . . . . . . . 115

# Preface

> Testing Quantum Chromodynamics (QCD) is particularly important in that it represents the less established sector of the standard model. Testing QCD is however difficult. It is more difficult than testing the electro-weak sector, because there the interaction is so weak that perturbation theory is almost always reliable and moreover the leptons are at the same time the fields in the Lagrangian and the particles in our detectors. On the contrary QCD is a theory of quarks and gluons while the real world is made up of hadrons. Also perturbative methods, our almost unique tools, are only applicable in those particular domains of strong interaction physics where the freedom, which is only asymptotic, can actually be reached.(...)
>
> The difficulty of testing QCD is reflected in the fact that no single process provides by itself a clearcut and definite experimental proof of the theory, at least when practical limitations in the experimental possibilities are taken into account. In view of a number of ifs and buts that can be raised against any given experiment it is clear that our confidence in QCD rests at present on the overall picture as is emerging from several processes and many different kinds of tests.

G. Altarelli In *Partons in Quantum ChromoDynamics* Phys. Rep. **81**, 1(1982) p. 4

The phrases by G. Altarelli quoted above give an extremely clean picture of the problems faced by experimentalists and theorists in the field. We shall face these problems in this thesis, which describes an experimental study on some effects of QCD radiation in the analysis of hadronic jet events at the Collider Detector at Fermilab (CDF). CDF is a multipurpose detector built to study proton-antiproton interactions at the Fermilab Tevatron Collider, which provides a center of mass energy of 1.8 TeV, the highest available in the world.

Effects of the radiation on inclusive measurements are studied and their agreement with predictions from theoretical perturbative calculations and Montecarlos is shown.

An exclusive study on spatial correlations in multi-jet events is performed giving evidence for the presence of colour interference effects, in agreement with latest theoretical implementations of QCD coherence in Montecarlos (Herwig).

The importance of this analysis is twofold: On one side it constitutes a test of perturbative QCD predictions on effects of higher than simple leading order. On the other side this is a test of our ability to detect effects predicted in the framework of a theory working on quarks and gluons which, by virtue of confinement, are not directly observable.

The fact that colour interference, predicted at the parton level, is still visible even after the hadronization stage is a non-trivial result which should motivate the efforts for refined theoretical calculations of elementary QCD processes. The good agreement of the detected effect with Herwig predictions confirms the validity of its approach to the approximation of interference. This is a significant result, since the Montecarlos are important (and widely used) tools, necessary in the process of data reduction and understanding of the underlying physics.

Chapter 1 shortly summarizes some elements of the parton model and its development to QCD. The Leading Log Approximation (LLA) is successively compared to the Parton Level (PL) calculation approach. The style of the presentation is inspired to the papers cited in references [57,29,30,80], which succeeded in giving a short and compact, but clear exposition of the matter.

Chapter 2 is a synthetic description of the CDF detector, and emphasis is posed in describing the detector components relevant in the selection and measurements of jet events in this thesis: the 'projective towers' calorimeter, the 'tracking' system and the trigger system. A short section is devoted to the description of a trigger component, namely the "Main Ring Veto", to development of which the candidate has contributed.

Chapter 3 is composed of two main sections.

In the first, operational definition and methods for the measurement are discussed. Particular care is taken in describing the *fixed cone* algorithm used for jet reconstruction. Systematic erros sources are discussed in some deep. In the second part the experimental sample and selection cuts are described and characteristics of the simulated samples discussed.

In Chapter 4 a study is presented of the effects of gluon radiation on the measurement of inclusive quantities like $d\sigma/dM_{jj}$, the dijet differential cross section as a function of the dijet invariant mass. Extensive comparisons of the data to Leading Order QCD, Next-to-Leading Order QCD, and shower Montecarlo predictions, support the analysis.

In Chapter 5 a more exclusive analysis of radiation effects is made, concerning the experimental observation of colour interference effects. The interference pattern is detected in the angular distribution of the third jet in multijet events. It is also shown that this pattern is reproduced by the Montecarlo Herwig, which implements colour coherence in the LLA, and not reproduced by the Montecarlo Isajet, which does not implement colour coherence.

# Chapter 1

# Theoretical Frame

## 1.1 Introduction

A vast quantity of knowledge about elementary particles and forces has been incorporated into a simple framework known as the "Standard Model".

According to the Standard Model, all matter is composed of two basic types of particles, quarks and leptons, and their corresponding antiparticles. The quarks and leptons come in several varieties ( "flavours" ), as listed in table 1.1. The standard model describes three forces (interactions) these particles experience: the electromagnetic interaction between charged particles and photons, described by Quantum Electrodynamics (QED) [1]; the weak interaction, unified with QED in the Glashow-Weinberg-Salam $SU(2) \times U(1)$ model [2]; and the strong interaction between quarks and gluons, which causes the forces between nucleons, described by the $SU(3)$ gauge theory Quantum ChromoDynamics (QCD) [3].

The subject of this thesis deals with the strong interaction. QCD [4,5] is a renormalizable field theory similar to QED, in that quarks[1], which carry a different kind of charge called 'colour', interact with gluons (analogous to photons in QED) via a Lagrangian similar in appearance to the QED Lagrangian. Unlike QED, the gauge symmetry is non-Abelian, causing gluons also to possess colour charge and consequently interact with gluons as well as quarks. The basic interactions among

---

[1] For simplicity, both quarks and antiquarks will be referred to as quarks in the discussion

| QUARKS | | | | |
|---|---|---|---|---|
| | | | | *charge* |
| *down-type quarks* | d | s | b | $-\frac{1}{3}$ |
| *up-type quarks* | u | c | t | $+\frac{2}{3}$ |
| LEPTONS | | | | |
| | | | | *charge* |
| *Charged leptons* | e | $\mu$ | $\tau$ | $-1$ |
| *Neutrinos* | $\nu_e$ | $\nu_\mu$ | $\nu_\tau$ | 0 |

Table 1.1: Fundamental matter particles of the standard model

gluons and quarks are the Feynman vertices shown in fig. 1.1. The additional gluon-gluon interactions cause the strong coupling constant $\alpha_s = g_s^2/4\pi$ to have a qualitatively different behaviour with $Q^2$ (the interaction momentum transfer scale) than the QED coupling constant $\alpha_{QED} = e^2/4\pi$. The $Q^2$ dependence of the strong coupling constant $\alpha_s$,illustrated in fig. 1.2, is approximately:

$$\alpha_s(Q^2) = \frac{4\pi}{(11 - \frac{2}{3}N_f)ln(Q^2/\Lambda_{QCD}^2)}$$

where $N_f$ is the number of quark flavours with mass less than $Q$ and $\Lambda_{QCD}$ is a constant determined experimentally to be about 0.2 GeV.

The *running* of the strong coupling constant causes the strong interaction to be very different at small versus large $Q^2$. In the infinite $Q^2$ limit, quarks and gluons are *asymptotically free* particles, and the theory is well behaved [6]. Below about 1 $GeV^2$, however, the coupling becomes large and the techniques of perturbation theory can not be applied; it is believed that this causes the quarks and gluons to be confined into hadrons and not to be observable in isolation.

## 1.2 High energy hadron-hadron collisions

QCD is the evolution of the *parton model* first introduced in order to explain results of Deep Inelastic Scattering (DIS) experiments [7]. The essence of the parton model is to regard a high-energy hadron as a collection of quasi-free partons, which share

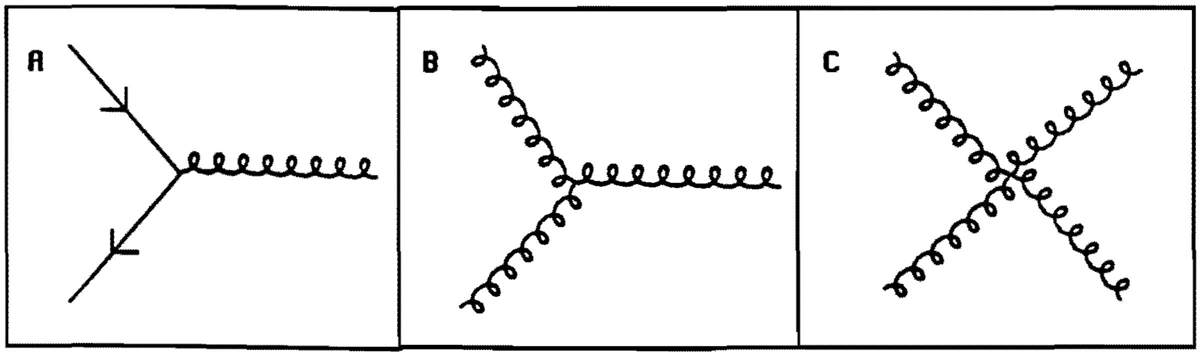

Figure 1.1: Interactions of quarks and gluons in Quantum ChromoDynamics

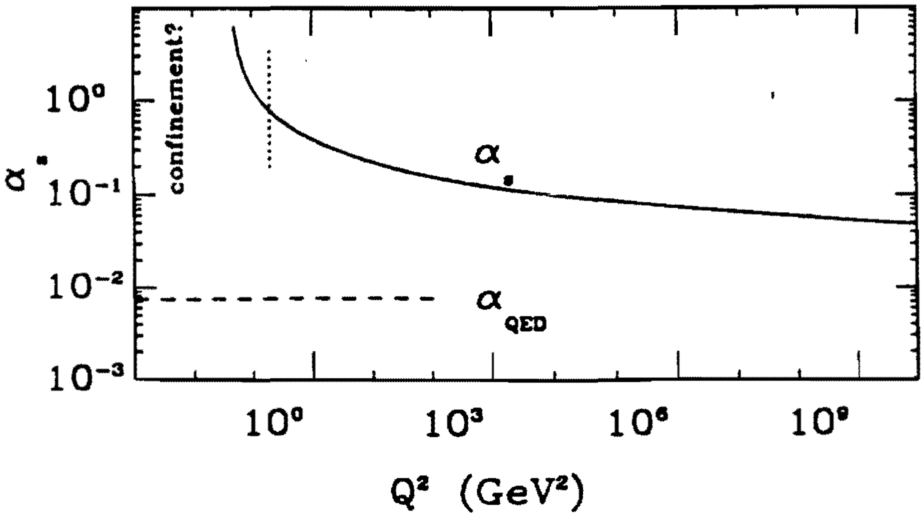

Figure 1.2: $Q^2$ dependence of the strong coupling constant $\alpha_s$ and the QED coupling constant $\alpha$.

its momentum. Thus we envisage a proton of momentum $P$ as being made of partons carrying longitudinal momentum $x_i P$, where the momentum fractions $x_i$ satisfy $0 \leq x_i \leq 1$ and $\sum_i x_i = 1$.

The prototype hadron-hadron reaction is depicted in fig. 1.3. A hard scattering occurs between the partons $i, j$ which are separated from the 'spectator' partons. The probability that parton $i$ carries a momentum fraction $x_i$ is descibed by the distribution $F(x_i)$: $F(x)\,dx$ is the number of partons with momentum fraction between $x$ and $x + dx$ [8]. The final state partons (1, 2 in fig. 1.3) *fragment* forming a cascade as they "dress" themselves into the final state hadrons. The time and energy scale of the final state cascade is set by the *confinement* size of the hadron and is characterized by the properties of the 'normal' soft interactions; therefore the momentum transverse to the direction of the original parton is expected to be limited, thus giving rise to a "jet" of highly collimated hadrons.

Interference between these three stages would be suppressed by the large differences in the time scales.

The main features of the parton model as described remain in the QCD approach, but are cast in a slightly different language. There are two types of partons, as seen in the previous section: the quarks, and gluons. The distribution functions of parton momenta, $f(x)$, are related to the momentum distributions for gluons and each of the quark flavours and are $Q^2$ dependent in QCD. The structure functions are defined as $F(x_i, Q^2) = x_i f(x_i, Q^2)$. The dynamics of the hard scattering of the partons are described in detail by the perturbative expansion of the QCD Lagrangian [9]. The two are tied together with the theorem of factorization [10] which states that since the initial and final distributions of partons interact on time scales that are vastly different from that of the hard scattering, the interference between the hard scattering and the initial and final states should be small; therefore one may sum up over the individual momentum densities of the incoming constituents $f(x_i, Q^2)$ of all the 'subprocesses' and add the cross sections (the interaction cross

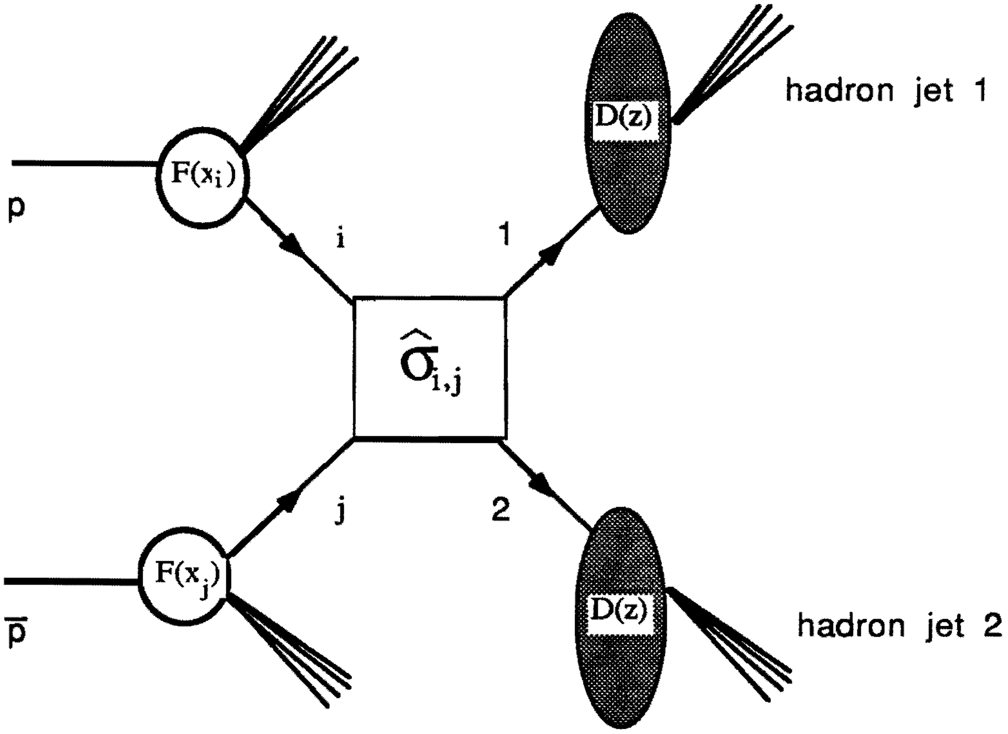

Figure 1.3: High energy hadron-hadron collision in the parton model

section of parton i with parton j is called a 'subprocess cross section' and is written $\hat{\sigma}(i,j \rightarrow 1,2))$ [11]. The expression for the production of two jets, where we are considering a definite final state $(1,2)$ may be written schematically as:

$$\sigma(\bar{p}p \rightarrow 1,2) = \sum_{ij} \int f_i(x_l, Q^2) f_j(x_k, Q^2) \hat{\sigma}(i,j \rightarrow 1,2) dx_l \, dx_k$$

The parton flavours are denoted by i,j. The probability of the incoming partons $i$ $(j)$ to have momentum fraction $x_l$ $(x_k)$ has been indicated by $f_i(x_l, Q^2)$. The hard scattering parton cross section is given by $\hat{\sigma}(i,j \rightarrow 1,2)$ and the scale at which the interaction occurs is given by $Q^2$.

### LOWEST ORDER QCD

The subprocess cross sections and evolution of the structure functions with $Q^2$ are predicted by perturbative QCD. The Feynman rules for calculating the cross section in terms of a perturbation expansion in the strong coupling $\alpha_s$ are determined from the QCD Lagrangian. This is analogous to perturbative QED [18]. For our jet events $\alpha_s \simeq .1$, so it is plausible that the lowest order of expansion provide a reasonable approximation. Theoretical ignorance of higher order terms in the perturbative expansion is generally represented by an ambiguity in the $Q^2$ scale at which $\alpha_s$ and the structure functions are evaluated. This is because the cross sections are in principle independent of the $Q^2$ scale, but the $Q^2$ dependence appears on the truncated expansion.

The lowest order expression for the subprocess cross sections have been calculated [19] for all contributing Feynman diagrams, shown in fig. 1.4.

### QCD RADIATION AND HIGHER ORDER PROCESSES

In the previous discussion we treated two jet production as originating exclusively from a $2 \rightarrow 2$ process. This is approximately correct; however there are some important exceptions which modify the basic parton model of fig. 1.3. The basic

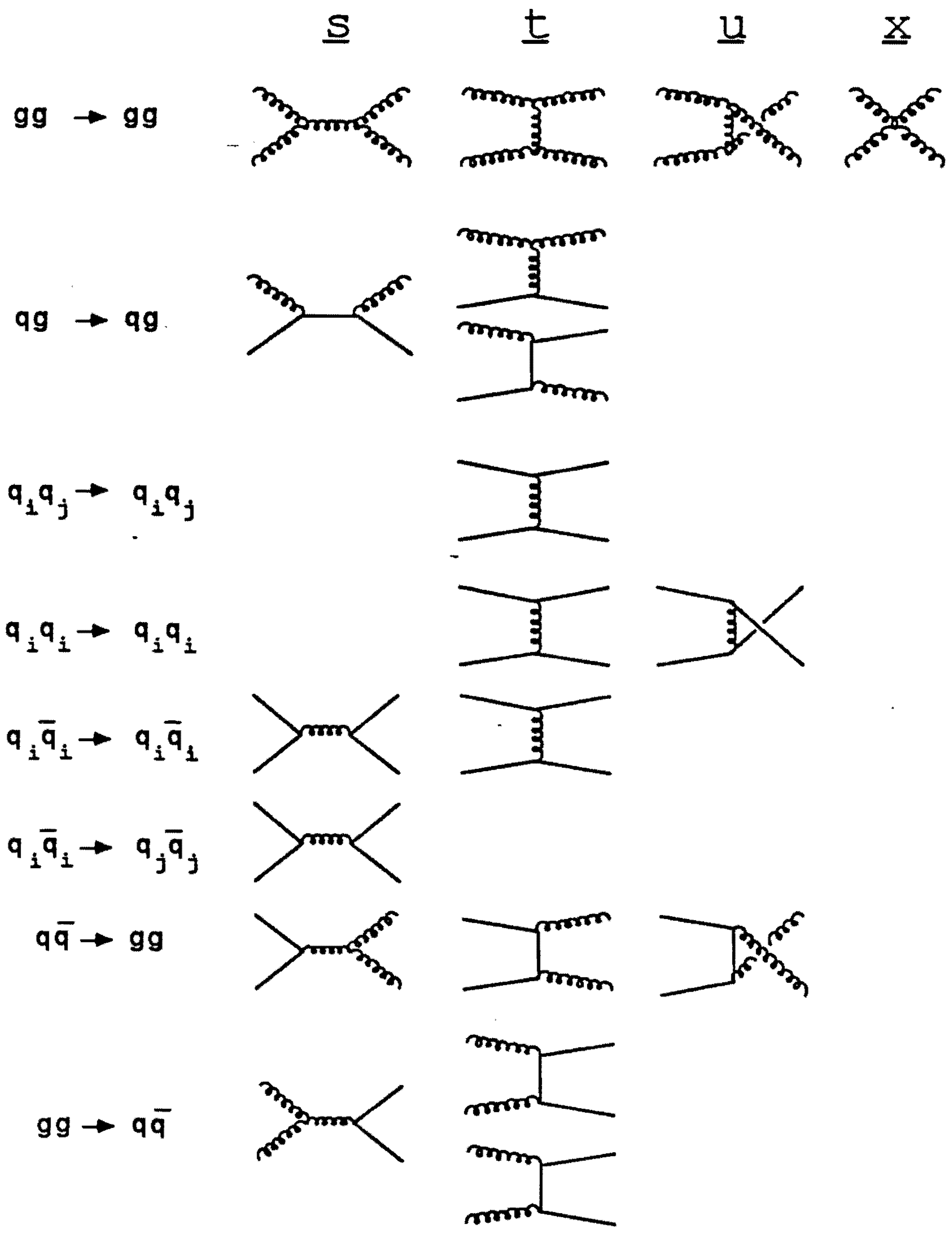

Figure 1.4: Lowest order QCD Feynman diagrams for all contributing subprocesses (gluon-gluon, quark-gluon, and quark-quark interactions). Rows are distinct subprocesses and columns are s, t , u and x channel contributing diagrams.

$2 \to 2$ interaction, or *hard scattering*, is a QCD interaction. In QCD the interacting quarks and gluons can radiate gluons in both the initial state, before the hard scatter, and in the final state, after the hard scatter. The frequency of occurrence of this *initial and final state QCD radiation* falls sharply with the transverse momentum $p_\perp$ of the radiated gluon with respect to the parent parton direction. In addition, there can be one or more extra partons produced within the hard scatter itself, in which case we are dealing with parton subprocesses of the form $2 \to 3$, $2 \to 4$ etc. Hard *higher order processes* are rare compared to the basic $2 \to 2$ interaction of partons. As a very crude rule of thumb they are produced with relative frequency $\alpha_s^n$ where $n$ is the number of partons in the final state minus 2. The dividing line between initial and final state gluon radiation and hard higher order processes is theoretically and experimentally ambiguous.

### JET FRAGMENTATION

Up to now we have totally neglected the third phase of the process shown in fig. 1.3, assuming that there is a one-to-one correspondence between final state partons and jets. This simple approximation is not able to predict internal features of jets, such as the 'fragmentation function' $D(z)$ describing the momentum distribution of hadrons from an outgoing parton.

The fragmentation properties of jets should be entirely specified by QCD (with the exception of effects due to weak and electromagnetic decays), if QCD is indeed the correct theory of strong interactions. Fully understanding the phase transition in which hadrons are formed is beyond the capabilities of the present approach.

At higher and higher jet momenta, QCD is able to make more solid predictions about jet properties [21]. As illustrated in fig. 1.5, the development of a jet can be schematically separated into three stages:

1) the production of a parton in an hard collision, with a virtual mass of the order of the collision momentum transfer;

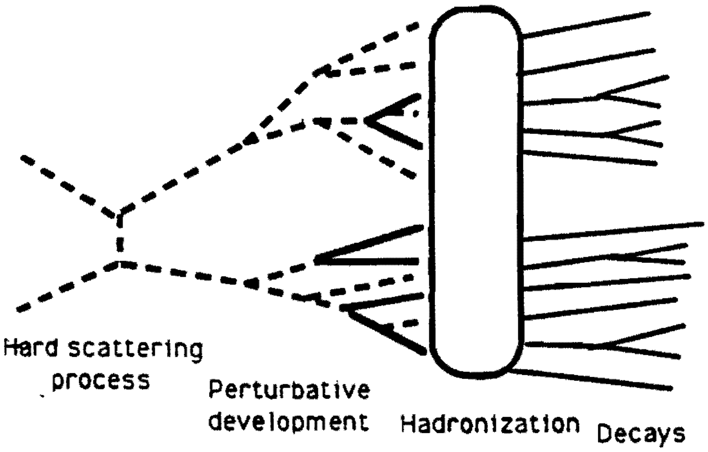

Figure 1.5: Schematic development of partons into jets of hadrons indicating the three phases of development.

2) perturbative evolution of the parton to a lower virtual mass ($\sim 1 GeV$), through gluon *bremsstrahlung* and quark-antiquark pair production;

3) the transition into hadrons.

We will refer often to the term 'fragmentation' meaning the result of both phase 2 and 3 of the jet development. We will use 'shower development' to indicate phase 2, the *perturbative* development, and 'hadronization' to identify phase 3, that is the non-perturbative transition from the parton shower to hadrons. With increasing jet energy, as the tools of perturbation theory become applicable to a larger portion of the jet development, QCD is able to make predictions on jet shape and its internal features [20].

### 1.2.1 Structure functions

The structure functions summarize the complex interactions among the hadron constituents by giving the probability distribution of the momentum fraction $x$ carried by each parton type. In principle they are completely determined by the QCD is the use of shower Montecarlos [22].

For PL calculations one evaluates in perturbation theory (PT) matrix elements between 'free' on-shell partons, and assumes that infrared physics (perturbative or not) will not affect the distributions. This is true for some inclusive distributions (e.g. the inclusive jet $p_t$), but certainly not for exclusive ones, say multiplicities or fragmentation functions. This technique has the advantage of allowing exact calculations of higher order processes, and maintains the full quantum properties of the theory (e.g. the quantum interferences between different diagrams). It is absolutely needed for precise tests and measurements. On the other hand it has the disadvantage of not describing in a complete fashion the final state, and the generated events cannot then be interfaced in a meaningful way with a detector simulation.

In shower Montecarlos [23] one starts from the simplest hard scattering that leads to the desired process, and then evolves initial and/or final states in a unitary way with branching probabilities given by the Altarelli-Parisi splitting functions. This is a fully exclusive description of the process, realized in the Leading Logarithmic Approximation (LLA), in which all of the dominant infrared and collinear logarithms are accounted for, at any order in perturbation theory. This is the approximation in which higher order processes are handled in a shower Montecarlo. Therefore large-$p_t$ branchings (leading to production of multiple-jets) are in principle not described correctly and hard to implement consistently.

Therefore PL calculations and Shower Montecarlos appear as complementary tools in the analysis of higher order processes, and since none of the two approaches is entirely satisfactory, each of them having its own drawbacks, cross checks between the two become extremely important.

- Parton level calculations

  Enormous progress was made in the past few years in the calculation of multiparton processes [24]. Exact analytic expressions are available for processes lagrangian, but bound states imply small $Q^2$ scales and therefore non-perturbative calculations. Structure functions cannot therefore be obtained theoretically in QCD, but rather they must be extracted from experimental data. Data cover, of course, a finite range of $Q^2$. The evolution of the structure functions with $Q^2$, anyway, can be calculated in perturbation theory, with the aid of the Altarelli-Parisi equation [13]. The input of this equation are structure function measurements,e.g from DIS experiments. Since the gluon distribution functions cannot be directly extracted from the data (because of the use of lepton probes which do not couple directly to the gluon) they have to be somehow inferred; furthermore there is uncertainty in the choice of a proper scale of momentum transfer. Different parametrizations of the structure functions are available, obtained from different sets of experimental data; they also come in different sets intended to bracket uncertainties on the gluon structure functions and on the choice of the proper $Q^2$ scale for evolution; finally, different solutions are obtained depending on the order of perturbation theory at which the functions are obtained. There exist therefore Leading Order structure function parametrizations such as Duke & Owens (DO) sets 1 and 2 (different gluon distribution) [14], Eichten, Hinchliffe, Lane & Quigg sets 1 and 2 [12]. There exist also higher order parametrizations from recent studies by Diemoz, Ferroni, Longo & Martinelli (DFLM) [15] and Martin, Roberts & Stirling (MRS). Most recent works profit of new experimental data and of understanding of some inconsistencies between different old DIS experiments: these are parametrizations by Harriman, Martin, Roberts & Stirling (HMRS) [16] and Morfin & Tung [17].

## 1.3 Description of higher order processes: Shower Montecarlos versus Parton Level Calculations

In the study of large $p_t$ phenomena, depending on the kind of variables or distributions one is interested in, two different approaches are available for theoretical predictions: one is the calculation of Parton Level (PL) amplitudes, and the other with up to 6 gluons in the final state [25], and very compact and reliable approximations have been introduced to speed up and simplify the simulations [26]. These calculations are fundamental for reliable estimates of multijet backgrounds to new physics (e.g. $t\bar{t} \to 6jets$, $(W \to e\nu) + jets$,......), since in principle they contain ingredients missing in the shower Montecarlos, such as the correct treatment of the large-$p_t$ branchings. These multi-parton calculations are quite difficult to implement in a consistent way in a shower Montecarlo, because of problems such as double counting of similar configurations. At the same time, parton level multi-parton calculations are affected by the presence of IR and collinear singularities, which are cured in the Montecarlo. Proper isolation and 'hardness' cuts guarantee the finiteness of the PL calculation, but the sensitivity to these cuts is not entirely physical in absence of the full set of virtual corrections.

A complete calculation of QCD matrix elements for parton-parton scattering to the order $\alpha_s^3$ was recently completed by K. Ellis and J. Sexton [27]. It is being used by two groups [28] for the calculation of the inclusive jet cross section at the Next-to-Leading Order (NLO). The phenomenological importance of this calculation lies in the fact that the full knowledge of the order $\alpha_s^3$ radiative corrections allows a more precise determination of the cross sections, possibly reducing the systematic theoretical uncertainties to a level of 20%.

- Shower Montecarlos

Shower Montecarlos describe in a complete fashion the final state providing observable particles, and the generated events can be interfaced to a detector simulation.

We have previously seen that at the current Collider energies fragmentation can be described in two steps. The first step is the perturbative evolution of the hard partons coming from the hard scattering process. The $Q^2$ scale and the virtualities of these partons are so large that perturbative QCD is applicable and can describe in the LLA the branching process. It is during this stage that multiplicities and $z$-distributions develop. If the branching is performed according to the idea of pre-confinement (i.e. colour singlet configurations tend to develop close in phase space), at some low $Q^2$ scale $(\bar{Q}^2 > \Lambda_{QCD}^2)$ we will have a bunch of low mass colour-singlet quark clusters. The multiplicity and mass distribution of these clusters will depend on the particular hard process we started from, but the evolution of these clusters below the scale $\bar{Q}^2$ (i.e. the hadronization) is universal (even though non-perturbative) since by now all the memory of the initial process is lost. This second step of the fragmentation process can be modeled phenomenologically by fitting data at one given energy and for one given process (say $e^+e^- \rightarrow 2jets$ at PETRA), but once that is done the same model can be used at higher $s$ and for different processes (say $p\bar{p} \rightarrow 2jets$, $p\bar{p} \rightarrow \gamma + jet$ etc.). The differences between different energies and different processes will be accounted for by the different initial conditions for the development of the shower, and these differences will be handled by *first-principles* perturbation theory.

# Chapter 2

# The Collider Detector at Fermilab

The Collider Detector at Fermilab (CDF) is a general purpose detector operating on the Tevatron $\bar{p}p$ collider at Fermi National Accelerator Laboratory (FNAL) at center of mass energy $\sqrt{s} = 1.8$ TeV which is actually the highest in the world. In the 1988/89 run a luminosity of $10^{30} cm^{-2} s^{-1}$ was reached and surpassed

The detector covers a large angular region, down to $1.7^o$ from the beam, and over the entire $2\pi$ range of the azimuthal angle[1].

The basic goals of the Collider Detector at Fermilab are:

- detect charged particles and measure their momentum;
- measure the position and energy of electromagnetic as well as hadronic showers;
- identify leptons;
- observe indirectly non-interacting particles like neutrinos, by measuring the missing transverse momentum;
- trigger on expected and unexpected physics performing flexible selections on functions of all the measured quantities listed above.

---

[1] CDF uses a conventional frame of reference with origin in the center of the detector, the $z$ axis along the beam and $z > 0$ in the proton direction. The polar angle $\theta$ is measured with respect to the beam axis ($\theta = 0$ in the proton direction) while $\phi$ is the azimuthal angle ($\phi = 90^o$ in the vertical upward direction). Often the pseudorapidity $\eta = -ln(tan(\theta/2))$ is used in place of the angle $\theta$.

In order to achieve this, the interaction region is surrounded by layers of different detector components. Particles encounter in a sequence tracking detectors, sampling calorimeters and muon detectors. Events are analysed in a very short time (few microseconds) by a powerful and flexible trigger system.

Fig. 2.1a) shows a perspective view of the CDF detector, evidentiating the central, mobile part covering the region $10^o < \theta < 170^o$, the forward part, covering the region $1.7^o < \theta < 10^o$, and the backward, which is a mirror image of the forward part.

We will focus our attention on those parts of the detector that are relevant to the jet analysis. A description of the complete detector can be found in reference [31].

Calorimeters are the most important devices for jet measurements. A Vertex Time Projection Chamber (VTPC) was used to measure the event vertex, necessary for precise calculation of jet trajectories. The Central Tracking Chamber (CTC) was used to measure the response of the central calorimeters to low energy particles. The Beam-Beam Counters (BBC) were used in the hardware trigger and provided an accurate measure of the interaction time as well as an estimate of the luminosity. The hardware trigger made the decision during the data acquisition (online) to retain an event for later (offline) analysis.

## 2.1 Calorimetry

CDF employs sampling calorimeters. Sampling calorimeters, as opposed to total absorption calorimeters, only sample a fraction of the energy deposited by an incoming particle. Layers of sampling material are interleaved with layers of absorber in a sandwich. Incoming primary particles produce showers of secondary particles in the absorber. The showers deposit a fraction of their energy in the sampling material, and that energy produces a signal which is registered and summed over all sampling layers. The ratio between this sampled energy signal and the true energy of the incident particle was determined in a *test beam* with particles of known

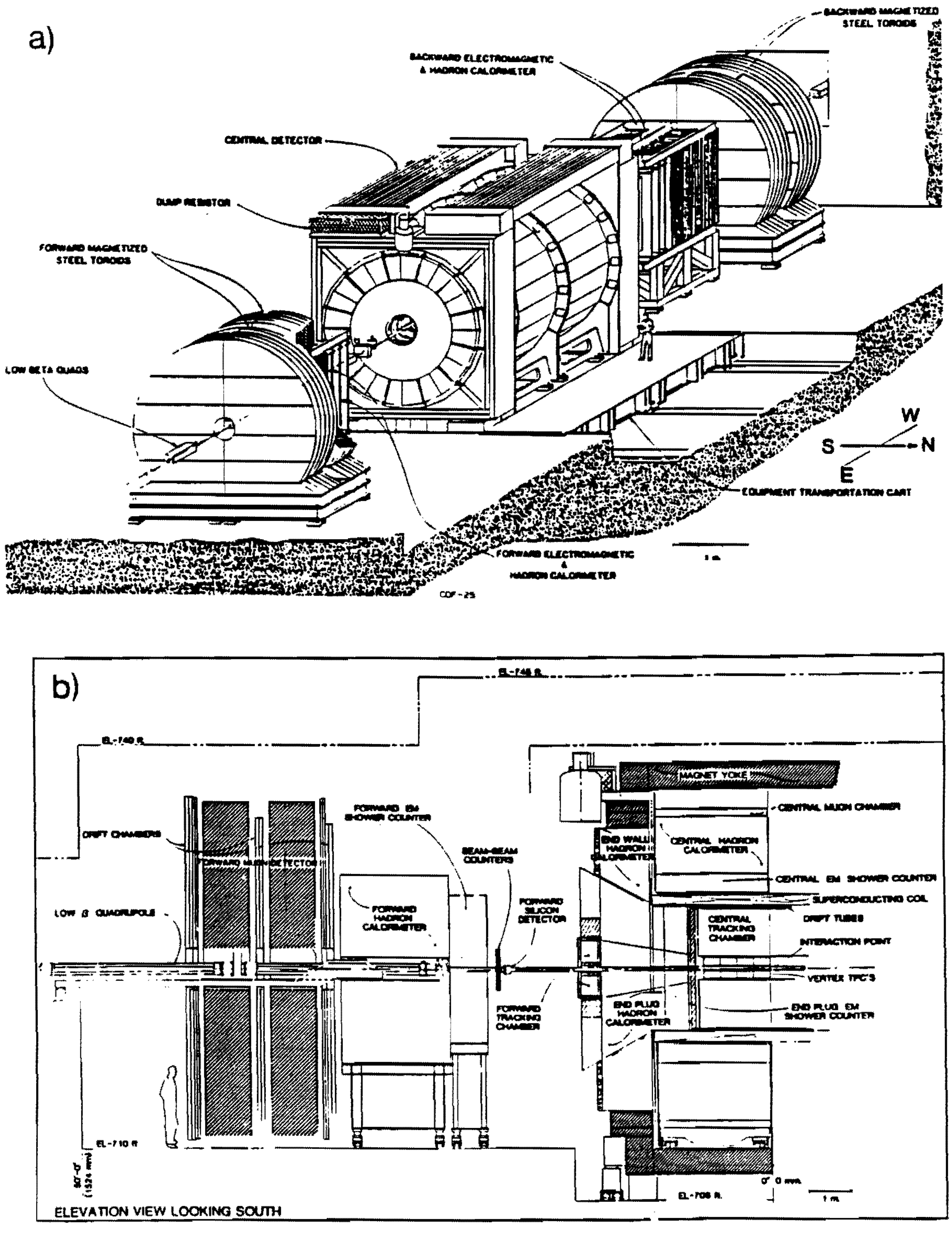

Figure 2.1: a) A perspective view of the CDF detector, showing the central detector and the forward and backward detectors; b) A side view of the forward half of the central detector and the whole forward detector

energy, and was later used in the *online calibration* to convert a measured signal to a measured energy. Radioactive source runs were performed concurrently with initial test beam calibration and periodically throughout the experiment in order to maintain this *initial calibration*.

All the calorimeters at CDF have been designed with projective *towers* which point towards the nominal interaction region, as shown in fig. 2.2a). By measuring the energy deposited in a projective tower by a particle, we also simultaneously measure the angle at which the particle emerged from the interaction. Each tower is approximately 0.1 units of $\eta$. For $|\eta| < 1.3$ the calorimeter towers are $15^o$ in $\phi$, and for $|\eta| > 1.3$ all the towers are $5^o$ in $\phi$, as shown in fig. 2.2b). This segmentation satisfies the demand for high granularity (the segmentation is fine enough that jets will normally spread over more than one tower) while minimizing cracks, that introduce dead regions between towers. Each tower is composed of an electromagnetic section to measure electrons and photons, and an hadronic section to measure hadrons.

The calorimeters at CDF are of two types. Scintillator calorimeters are in the *central* region ($|\eta| < 1.3$) and gas calorimeters are closer to the beam. Scintillator was chosen in the central region for its good resolution. Closer to the beam the towers are smaller in $\theta$ (fixed width in $\eta$), making the construction of a scintillator calorimeter impractical. In addition, the high multiplicities in the forward direction would age scintillator too quickly. Gas calorimeters are easily segmented into small towers using pads in the cathode plane, and robustly withstand high multiplicities, making them a natural choice for the forward region. In addition gas calorimeters are relatively cheap to construct. Unfortunately, they have typically worse resolution than scintillator calorimeters, and are subject to gain variations produced by changing ambient conditions.

### Central Calorimeters

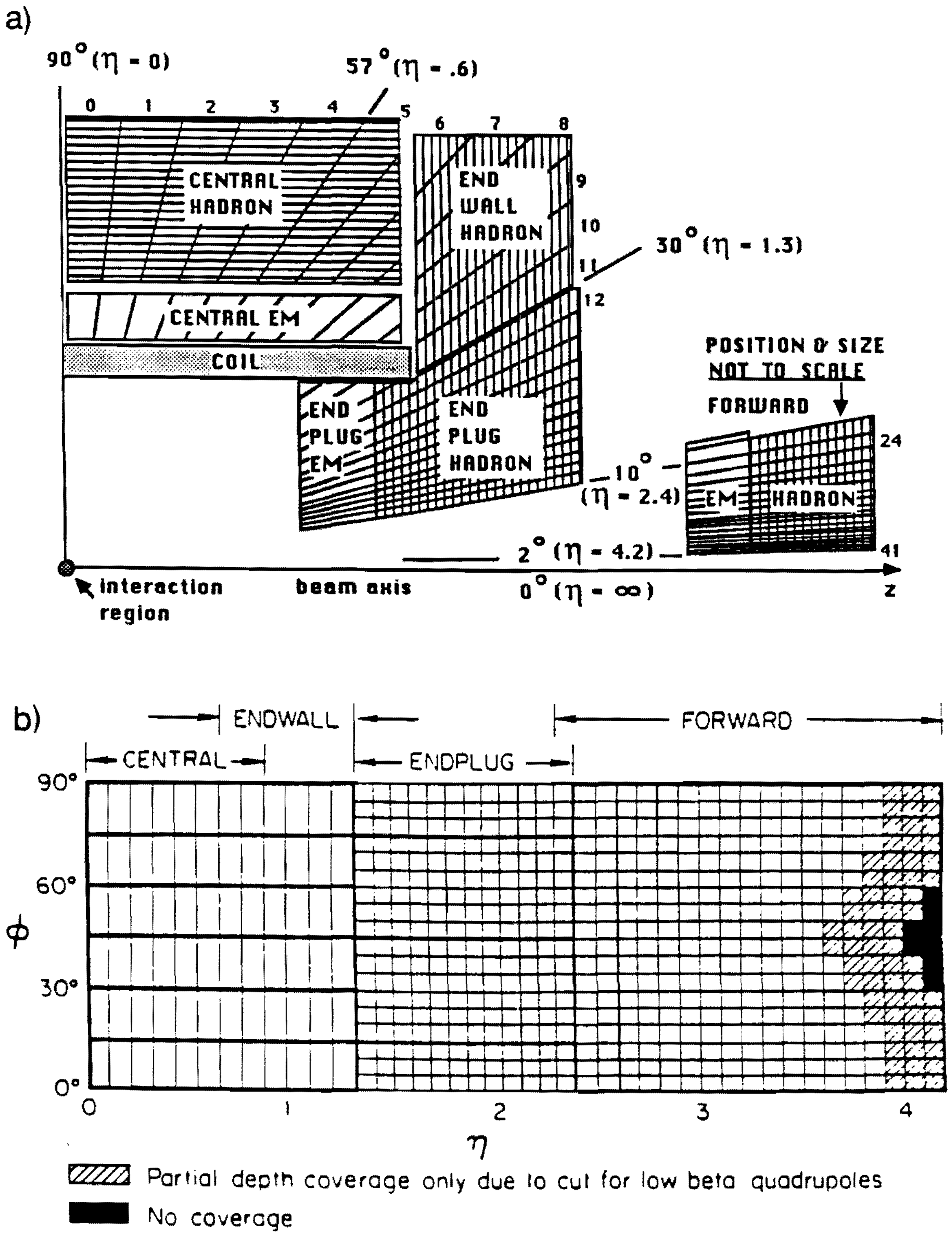

Figure 2.2: a) Cut-away view of the forward part of the central detector, evidentiating the central, endwall and endplug calorimeters (also shown, in size and position not to scale, the forward calorimeters); b) Schematic $\eta - \phi$ segmentation of one quadrant of CDF calorimeters.

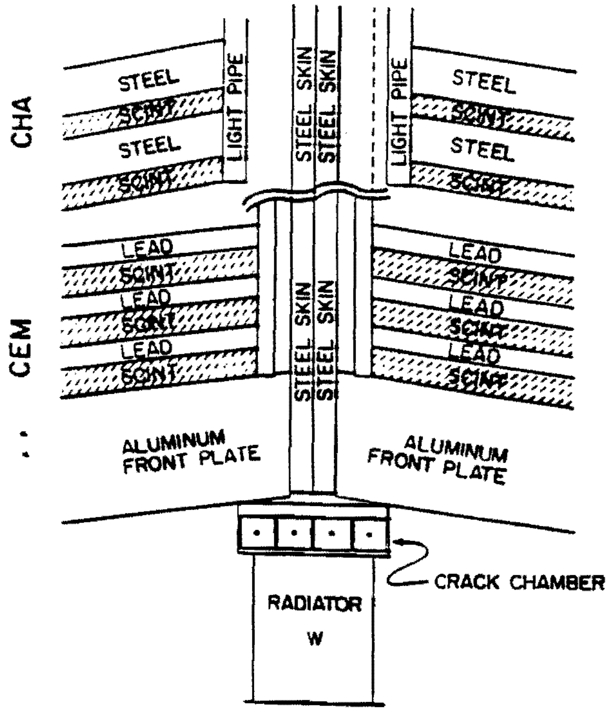

Figure 2.3: Sketch of a $\phi$ crack with the tungsten radiator in place.

The central calorimeter is azimuthally arranged in 48 physically separate 15° modules called *wedges*, 24 wedges at positive z and likewise at negative z.Each wedge is segmented into ten towers in $\eta$. Fig. 2.2a shows the towers at positive z that cover the angular range $90^o > \theta > 37^o$ ($0. < \eta < 1.1$). The towers are numbered 0 through 9 consecutively, where tower 0 is closest to $\theta = 90^o$.

Actually the central calorimeter is completed by the Endwall Hadron Calorimeter, as shown in fig. 2.2. Each wedge is completed by an Endwall module (same segmentation in $\eta - \phi$) that extends the central up to 30° ($\eta = 1.3$). Each Endwall module is divided into 6 towers numbered from 6 to 11 in fig. 2.2.

Each tower in the central is divided in an electromagnetic section (CEM) [32] and an hadronic section. The hadronic section is partially realized in the wedges (CHA) and partially in the Endwall Hadron Calorimeter (WHA) [33]. Towers 6, 7, 8 are partly in the CHA and partly in the WHA (fig. 2.2): the hadronic signal for these towers is the sum of the signals from the CHA and WHA.

The $\phi$ boundaries between the wedges constitute uninstrumented regions were the response is not flat ($\phi$ cracks). A tungsten radiator (10 radiation lenghts) "protects" each crack so that no charged particle can actually traverse a region with no absorber (see fig. 2.3). This also partially cures the problem of particles going through the light guides and emitting Čerenkov light (the so-called calorimeter "hot-spots"). The boundary between the two halves of the central calorimeter constitutes one of the main uninstrumented region (the 90° crack), while the steel and gap between the wedge and endwall modules generate a second region of complicated response. The $\eta$ boundaries between different calorimeter sections are known as $\eta$ cracks.

### Gas Calorimeters

All CDF gas calorimeters contain a mixture of 50% argon, 50% ethane with a small percentage of alcohol added to prevent glow discharge.

They are subdivided in several components: Endplug Electromagnetic Calorimeter (PEM) [34], Endplug Hadronic Calorimeter (PHA) [37], Forward Electromagnetic Calorimeter (FEM) [36], and Forward Hadronic Calorimeter (FHA).

A summary of the calorimeter properties in the different angular regions is given in table 2.1

## 2.2 Tracking system

The tracking detectors used in this analysis are the Vertex Time Projection Chamber (VTPC) and the Central Tracking Chamber (CTC). The VTPC is placed within the CTC and both are immersed in the 1.5 T magnetic field generated by the superconducting coil which surrounds them.

The VTPC [38] is made of eight octagonal time projection chamber modules stacked end-to-end in z. Four of the modules are shown surrounding the beam pipe in fig. 2.1b). Each chamber is divided azimuthally into eight octants. Each octant measures the radial and z coordinate of charged particles. The VTPC provides two

| | CEM | CHA | WHA | PEM | PHA | FEM | FHA |
|---|---|---|---|---|---|---|---|
| **$\lvert\eta\rvert$ Coverage** | $0.0 - 1.1$ | $0.0 - 0.9$ | $0.7 - 1.3$ | $1.1 - 2.4$ | $1.3 - 2.4$ | $2.2 - 4.2$ | $2.3 - 4.2$ |
| **Tower Size $\Delta\eta \times \Delta\phi$** | $\sim 0.1 \times 15^o$ | $\sim 0.1 \times 15^o$ | $\sim 0.1 \times 15^o$ | $0.09 \times 5^o$ | $0.09 \times 5^o$ | $0.1 \times 5^o$ | $0.1 \times 5^o$ |
| **Active Medium** | Plastic Scintillator | Plastic Scintillator | Plastic Scintillator | Gas | Gas | Gas | Gas |
| **Absorber** | Lead | Iron | Iron | Lead | Iron | Lead | Iron |
| **Thickness** | 18 r.l., 1 i.l. | 4.7 i.l. | 4.5 i.l. | 18.2 r.l. | 6.3 i.l. | 25.5 r.l. | 8.3 i.l. |
| **Resolution ($\sigma/E$ at 50 GeV) [%]** | 2 | 11 | 14 | 4 | 20 | 4 | 20 |

Table 2.1: Characteristics of the CDF Calorimeter Sections

kinds of information: the existence of one (or more) interaction vertex , and the z coordinate of the vertex (or vertices) within a resolution of 3 mm. The tracking information is provided down to an angle of about 3.5° from the beam direction

The CTC [39] is a 3.2 m long cylindrical drift chamber, providing precise momentum measurements (the momentum resolution is better than $\delta p_T/p_T^2 \leq 0.0011$, $p_T$ in GeV) in the rapidity region $|\eta| \leq 1$.

The chamber consists of 84 layers of sense wires arranged into 9 "superlayers": each superlayer consists of cells tilted by 45° with respect to the radial direction. There are five axial superlayers with 12 sense wires for each cell, providing $r - \phi$ information. The axial wire superlayers are interleaved with 4 stereo wire superlayers providing an $r - z$ view and consisting of cells with 6 sense wires forming alternate angles of $+3^o$ and $-3^o$ with respect to the beam axis. The spatial resolution for each cell is approximately $200 \mu m$; for stereo sense wires the resolution in $z$ is about 4 mm, while the system is able to resolve double tracks within less than 5 mm.

## 2.3 Beam-Beam Counters

The Beam-Beam Counters (BBC [40,42]) are scintillator hodoscopes close to the beam pipe used to provide the tracking chambers with an accurate measure of the interaction time (±200 ps), measure the vertex position (±4 cm), reject unwanted triggers and estimate the luminosity. Unwanted triggers were mainly collisions between the beam and residual gas in the beam pipe (beam-gas), energy deposition from halo particles in time with the beam (beam halo), or particles originating outside the CDF detector (cosmic rays). The BBC provided a count of true beam-beam collisions by comparing the time energy was deposited close to the beam with the expected beam crossing time. The BBC consist of two sets of sixteen scintillator counters, one set on each side of the interaction point at $|z| = 582 cm$. It covers an angular range $4.5^o > \theta > 0.32^o$ ($3.2 < \eta < 5.9$). A coincidence between the counters on one side (East) of the interaction point and the counters on the other side (West), within a 15 ns gate centered 20 ns after the beam crossing, was a single BBC $E \cdot W$ *coincidence*.

The integrated luminosity is measured by the number of BBC $E \cdot W$ coincidences divided by the fraction of the $\bar{p}p$ total cross section accepted by the BBC.

The BBC also provided the *minimum bias* trigger for CDF. This consisted of the BBC $E \cdot W$ coincidence alone.

## 2.4 Trigger and data acquisition structure

In the last physics run CDF had to deal with a delivered luminosity at the interaction point of over $10^{30}\, s^{-1} cm^{-2}$ corresponding to a collision rate around 70 kHz. The rate of data logging on tape had to be reduced to $\simeq 1Hz$. This forces to make a drastic selection in a very short time, tipically that available between beam crossing, of about 3.7 $\mu s$; any additional delay in the trigger selection results in fact in deadtime of the data acquisition system.

### 2.4.1 General architecture of the data acquisition

The CDF data acquisition system (DAQ) consists of three main parts: the analog front end electronics, the FASTBUS-based digital control and readout system and the VAX-resident configuration and control system software [41]. The front-end electronics is designed to readout the $10^5$ channels of the CDF detector, digitize and transfer this information to the FASTBUS system and Event Builder. The main body of the FASTBUS system coordinates timing and data transfer from front-end electronics and trigger systems to the VAX which logs the data on tape.

The CDF trigger [42] is structured in several levels which progressively reduce the rate, allowing the successive levels to take decisions of growing sophistication. This decisions range from fast coincidence of Beam-Beam Counters in level 0 to a full FORTRAN language elaboration on dedicated processors in level 3.

### 2.4.2 Level 0

Altough the level 1 trigger electronics could in principle make a decision within the time between two succesive bunch crossings more time is required for the trigger analog inputs to settle at the final level. This would give rise to a 50% deadtime already at level 1. This was the main reason for the introduction of the level 0. The final action of this stage is to inhibit the successive stages of the trigger in several situations:

a) No-interaction bunch crossings

b) Beam-gas interactions

c) Main Ring "splashes".

Two simple systems are available to the level 0 inhibit when one of these situations occurs. The first consists of the beam-beam counters, BBC, already discussed above. The second consists of the Main Ring Counters. The candidate contributed to the construction, test, and installation of this system.

The Tevatron booster ring (Main Ring) pipe crosses the CDF collision hall right over the detector. A steel shielding surrounds the Main Ring pipe to avoid radiation leakages to strike the detector, but when the Main Ring is operating occasional losses and beam-pipe interactions result in "splashes" of radiation down onto the CDF calorimeters. Since there is no timing relation between beam crossing in the Tevatron and "splash" this is seen by CDF as a large amount of energy out-of-time from the beam crossing. Anyway when the burst of radiation comes roughly in time with a minimum bias trigger the result is a lot of energy clusters in the hadron calorimeter, and eventually this clusters are big enough to trigger the inclusive jet selection. In fig. 2.4 a calorimetry 'Lego' plot[2] for a Main Ring event is shown.

---

[2] In the plot of figure each cell represents a calorimetric tower in the pseudorapidity-azimuth metric, the vertical axis reports transverse energy and for each tower hadronic and electromagnetic energy are reported separately (different shading).

Main Ring events are characterized by a long trail of hadron towers on the top of the detector ($\phi \simeq \pi/2$).

Though in principle it is possible to filter for Main Ring background in the offline analysis, to do so increases the number of fake events to be logged on tape, while resulting in effective deadtime for good data acquisition.

The Main Ring Counters are four small scintillator counters arranged in two pairs and placed right under the Main Ring pipe at the two sides of the collision hall. The two signals from counters of each pair are put in logical $OR$; each of these two signals opens a gate 4 $\mu s$ long and the $OR$ of the gates is used as a veto signal for the level 0 trigger. This simple scheme has shown an efficiency better than 99% in tagging Main Ring "splashes", while giving a very small contribution to the total deadtime of the data acquisition (less than 2%).

### 2.4.3 Level 1

The level 1 trigger processes analog signals. It shares a large part of its electronics with the level 2. The information available at level 1 contains BBC coincidence, presence of tracks with $p_t$ above a given threshold in the CTC, muon candidates with $p_t$ above a given threshold in the muon chambers, information from small angle systems, and separate information on total transverse energy in EM and Hadron calorimetry. The rate downstream to level 2 drops to a few kHz.

### 2.4.4 Level 2

The level 2 electronics takes about 10 $\mu s$ for its decision, which is based on topological features of energy in the calorimeters (jet identification), association of CTC stiff tracks to energy clusters (electron - $\pi^o$ discrimination), association of CTC stiff tracks to muon chamber segments (muon identification). The rate out of level 2 is reduced to a few Hz.

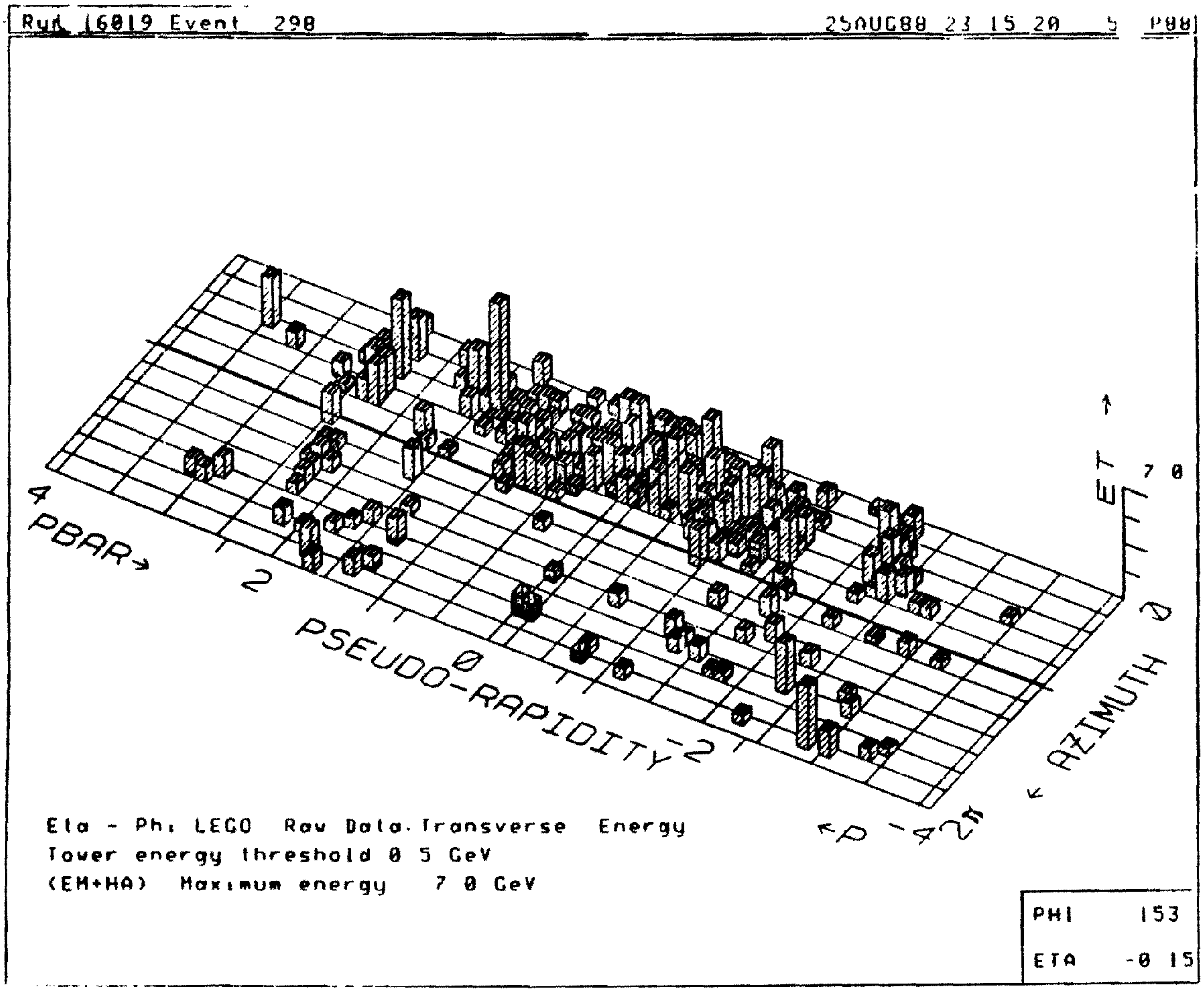

Figure 2.4: Calorimeter LEGO plot of a Main Ring "splash" event.

### 2.4.5 Level 3

The level 3 hardware is a "farm" of processors which run FORTRAN compiled programs, performing an high level offline-type analysis, such as rejection of cosmic rays, bursts of noise etc. The consequent reduction of rate decreases the number of useless events written on tape. The rate downstream to the data logger is reduced to $\simeq 1$ Hz.

# Chapter 3

# Jets at CDF

This chapter is divided into two main sections. In the first generalities on jet measurements are discussed. The huge amount of work done at CDF understanding jet measurements is the background on which our studies are founded, and is only summarized here. The second part is devoted to the description of samples and selection cuts used in the analysis described in the next chapters of this thesis.

## 3.1 Jet reconstruction

### 3.1.1 Clustering algorithms

The first step to measure quantities related to jets is their identification in calorimeter data. The jets are the hadronic remnant of scattered partons. Since hadronic remnants have typically limited transverse momentum with respect to the parton line they are highly collinear and can be "clustered" together to obtain what is experimentally defined as a jet. Typical values of particles momenta transverse to the jet axis are of order some hundred MeV. Fig. 3.1 shows an example of a high energy two-jet event as seen in the CDF detector. The figure shows a Lego plot of the calorimeter. Each cell represents a calorimetric tower in the $\eta - \phi$ space. On the vertical axis the transverse energy of the tower is reported.

The most widely accepted definition of jets is based on clustering of calorimeter cells in a metric of pseudorapidity $\eta$ and azimuthal angle $\phi$[44,45]. Several important

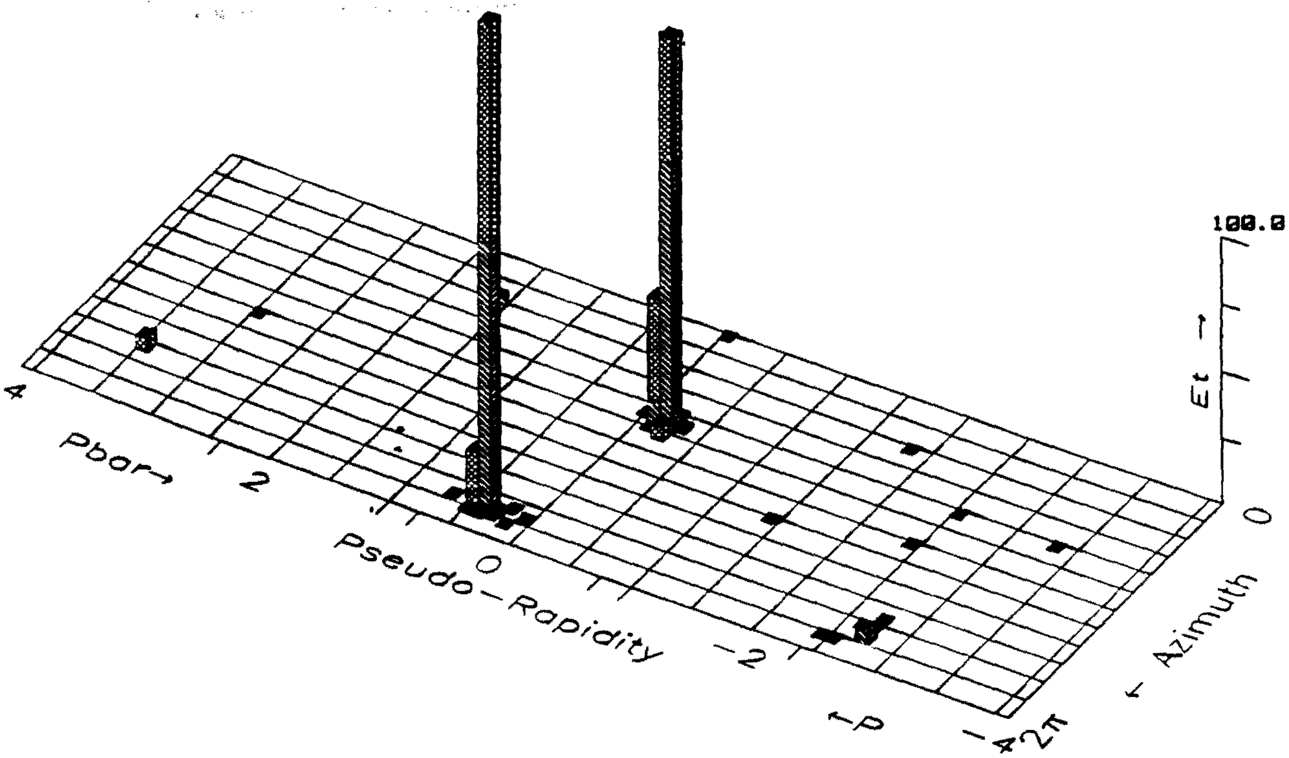

Figure 3.1: A high $P_t$ two-jet event as seen in the CDF detector

properties that should be met by a jet definition are [46]:

1. Simple to implement in an experimental analysis;
2. Simple to implement in a theoretical calculation;
3. Defined at any order of perturbation theory;
4. Yields finite cross sections at any order of perturbation theory;
5. Yields a cross section that is relatively insensitive to hadronization.

Many different jet finding algorithms are currently in use in $\bar{p}p$ collider experiments (CDF, UA1, UA2) and $e^+e^-$ experiments [47]. Each of these algorithms, even if only slightly different from the others, corresponds to a specific definition of jet, often not equivalent to the others.

The experimental possibility of QCD tests more precise than in the past has generated a constructive interplay between theory and experiments. The theory on its side has provided more sophisticated tools, such as complex shower Montecarlos and full Next-to-Leading-Order calculations [46,48,49]. Experiments have produced inclusive measurements characterized by very high statistics and reduced systematic uncertainties over very wide energy ranges.

To make it easy to compare analogous measurements performed by different experiments and to ease the test of theoretical calculations on these measurements a unification of the different viewpoints and the setting of a standard jet definition has become necessary. Some attempt has been made recently to collect and review the various definitions either from experimental and theoretical approaches [47], and to give a minimal standard definition of jet [52].

The *fixed cone algorithm*, already adopted by CDF, has been chosen, since it is the one which better responds to the requests of points 1.- 5. above. From a theoretical standpoint it has the advantage to be the most closely related to the techniques used to regulate collinear singularities in the calculation of gluon *bremsstrahlung* [50]. On the experimental side tests have been developed to compare the stability of jets obtained by different algorithms [52]; the fixed cone algorithm yields the most stable results. Apart from details given in the next section its main feature is to cluster calorimeter cells included in a cone of fixed size.

### JETCLU, THE CDF FIXED CONE ALGORITHM

The fixed cone algorithm JETCLU [53] starts with a seed tower with transverse energy above a given threshold (CDF uses 1 GeV). The contiguous towers are then used to compute an $E_t$ weighted centroid of the cluster. This is used as the center of a circle in the $\eta - \phi$ space, with a fixed radius $R = \sqrt{\Delta\eta^2 + \Delta\phi^2}$. All the towers inside the circle and above a certain $E_t$ *shoulder* threshold (CDF uses 100 MeV) are then included in the cluster; the $\eta - \phi$ centroid is recomputed from all the towers included, a new circle is drawn and a new list of towers is generated. The process is iterated until the list of towers is stable upon iteration. The cone identified by the $\eta - \phi$ circle and the $p\bar{p}$ interaction vertex is usually referred to as the *jet cone*. In the steps listed above it is possible to have some towers assigned to more than one cluster. At the final stage either the overlapping clusters are separated or merged together. First the amount of overlapping energy is computed. If it is larger than a certain fraction of the smaller cluster energy then the clusters are merged. If it is less the common towers are assigned to the cluster with the nearest centroid. After separation and/or merging of clusters the centroid is recalculated. Jet energy and momentum components are then computed using the list of towers associated to the corresponding cluster. Each calorimeter cell is treated as a massless particle. The i-th cell 4-momentum $(E_i, \vec{P}_i)$ is obtained using the energy release in the cell and the angular position $(\theta_i, \phi_i)$ of the center of the cell:

$$E = \sum_{i=1}^{N} E_i$$

$$P_x = \sum_{i=1}^{N} E_i sin\theta_i cos\phi_i$$
$$P_y = \sum_{i=1}^{N} E_i sin\theta_i sin\phi_i$$
$$P_z = \sum_{i=1}^{N} E_i cos\theta_i$$

where i is the tower index and N is the number of towers associated to the cluster. From the above definition it is possible to derive the transverse momentum of the jet as

$$P_t = \sqrt{P_x^2 + P_y^2}$$

And for transverse energy we get:

$$E_t = E\frac{P_t}{P} = Esin\theta$$

where $P = \sqrt{P_x^2 + P_y^2 + P_z^2}$. In this way the jet axis is identified by the direction of the 3-vector $\vec{P}$.

There is no precise guidance for the choice of the cone radius in the fixed cone algorithm. Studies on simulation of jet fragmentation for jets with $E_t$ above 20 GeV indicate that a cone radius between 0.4 and 1.0 yields measurements with a minimum dependence on hadronization and underlying event [51]. A cone radius $R = 0.7$ has been adopted as a standard in this thesis. It should anyway be noted that some interesting measurements sensitive to this parameter, like the inclusive dijet mass cross section shown in Chapter 4, suggest the importance of the use and the comparison of different cone sizes. Data from the 1988/89 run of CDF has been produced in this view using R=0.4, 0.7 and 1.0 in the clustering algorithm.

### 3.1.2 Jet energy resolution

The jet energy resolution was measured at CDF using the dijet $\vec{K}_t$ balancing technique first introduced by the UA2 collaboration [54].

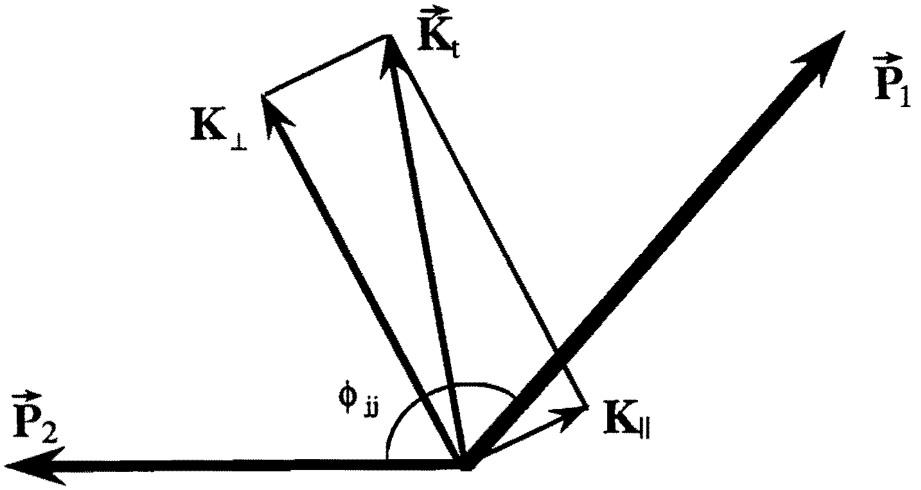

Figure 3.2: The dijet momentum imbalance $\vec{K_t}$ resolved into two components, $K_\perp$ and $K_{||}$. The component $K_\perp$ is dominated by QCD effects, the component $K_{||}$ contains both the QCD boost and the detector resolution effects

Fig. 3.2 shows a schematic representation of a dijet event in the transverse plane. $\vec{p_1}$ and $\vec{p_2}$ are the measured transverse momenta of the two jets; $\vec{K_t}$ is defined as the vector sum $\vec{p_1} + \vec{p_2}$, while $\phi_{jj}$ is the azimuthal separation of the two jets. A pair of orthogonal coordinates is defined so that the $\kappa_\perp$ axis bisects the angle $\phi_{jj}$, the $\kappa_{||}$ axis being orthogal to the former.

The two components of $\vec{K_t}$ along the two axes are connected to different effects contributing to the overall transverse momentum of the dijet system. $K_\perp$ does not involve the jet energy resolution directly: it is dominated by QCD effects which give the jets a finite boost in the transverse plane. $K_{||}$ is a superposition of the QCD boost and of the detector resolution. That $K_{||}$ is actually connected to the detector resolution can be understood by the following example: suppose we have only two jets exactly back to back: then $K_\perp = 0$ and $K_{||}$ gives the error in the $P_t$ measurement; if we had an ensamble of such events, we could estimate the resolution of the energy/momentum measurement from the width $\sigma_{||}$ of the distribution of $K_{||}$. Generally speaking $K_{||}$ is a combination of the QCD boost and of the detector resolution; therefore, being $\sigma_\perp$ the width of the distribution of $K_\perp$ we can subtract

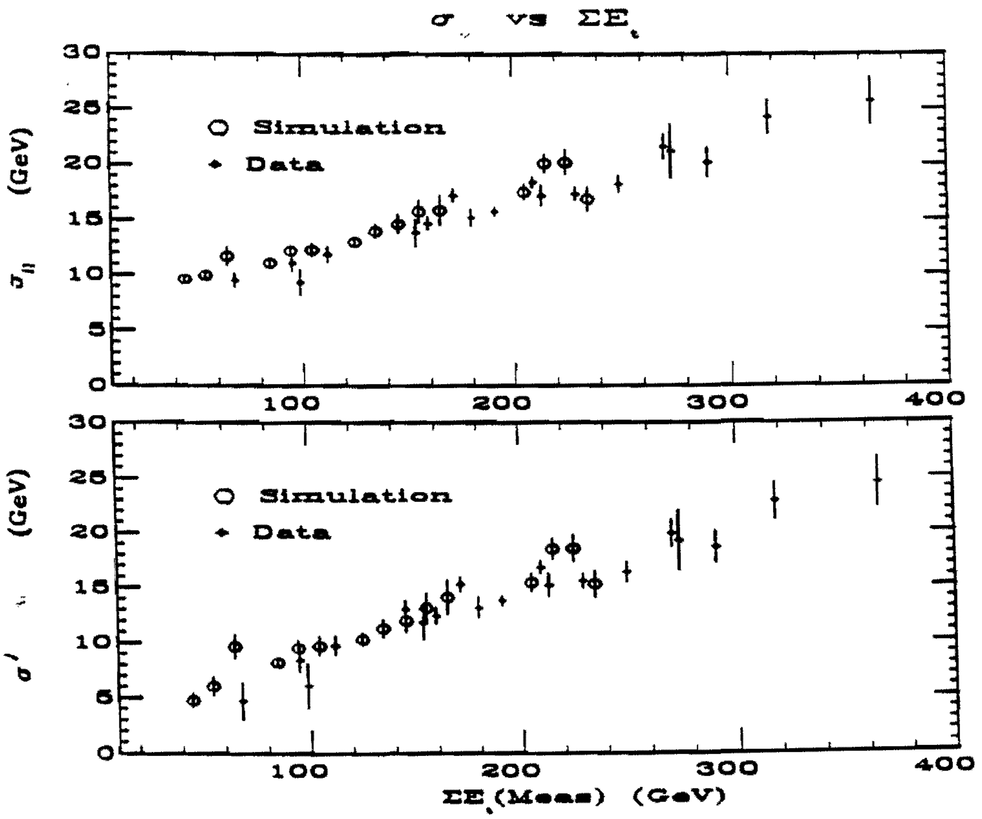

Figure 3.3: Energy resolution as a function of dijet $E_t$ for data and Montecarlo. The cone size is $R = 0.7$.

in quadrature the widths associated to the two components of $\vec{K}_t$:

$$\sigma' = \sqrt{\sigma_{\|}^2 - \sigma_{\perp}^2}$$

before estimating the energy/momentum resolution.

Fig. 3.3 shows the measured $\sigma_{\|}$ and $\sigma'$ as a function of the dijet $\sum E_t$ for data from the 1988/89 run compared to a simulation (used in the next section to obtain corrections to the energy scale). The agreement is clearly good on a large energy range, showing that the simulation reproduces well the jet resolution.

### 3.1.3 Energy scale

The CDF calorimeter is non-compensating. This means that the calorimeter will report different energies for pions than for electrons or photons; also this difference is a function of the energy of the incident particle. Since the jet energy is computed by adding up contributions from the EM and hadronic compartments and since jets are a mixture of neutral and charged particles with a variable fragmentation spectrum, the calorimeter response to jets is actually a convolution of the calorimeter response to single particles with the fragmentation functions for jets. In order to correct for this, therefore, response functions for both pions and electrons of *any* energy *and* fragmentation functions for jets are needed. In fact response functions can be determined from test beam and minimum bias data, while the fragmentation functions have to be somehow inferred from the jet data themselves.

Since the analysis presented in this thesis involves mostly energies measured by the central calorimeter, while the gas calorimeters are mainly used for angular measurements, we will shortly discuss in this section the major effects taken into account in the determination of the jet energy scale for the central calorimeter.

- Calorimeter non-linearity

  The central calorimeter response was determined with a combination of test beam and minimum bias data. Since the test beam cannot run below energies of about 10 GeV, therefore isolated tracks in the CTC from minimum bias events are used for low energy tests. Tracks in minimum bias triggers were used pointing to the central calorimeter and satisfying the isolation requirement that no other track pointed to a grid of 5X5 calorimeter cells around the cell of interest. This procedure, unfortunately yields big uncertainties due to correlated neutral particles which form a background around the high Pt charged one. This forces to operate a background subtraction on minimum bias data, being the prevailing source of systematic uncertainty (see fig. 3.8) in the determination of the response function [55].

  Fig. 3.4 shows the calorimeter response to pions as a function of the pion energy from test beam and isolated track data. The vertical axis shows the energy (E) reported in EM plus hadronic calorimeter divided by the momentum (P) of the incident particle. The horizontal axis shows the particle

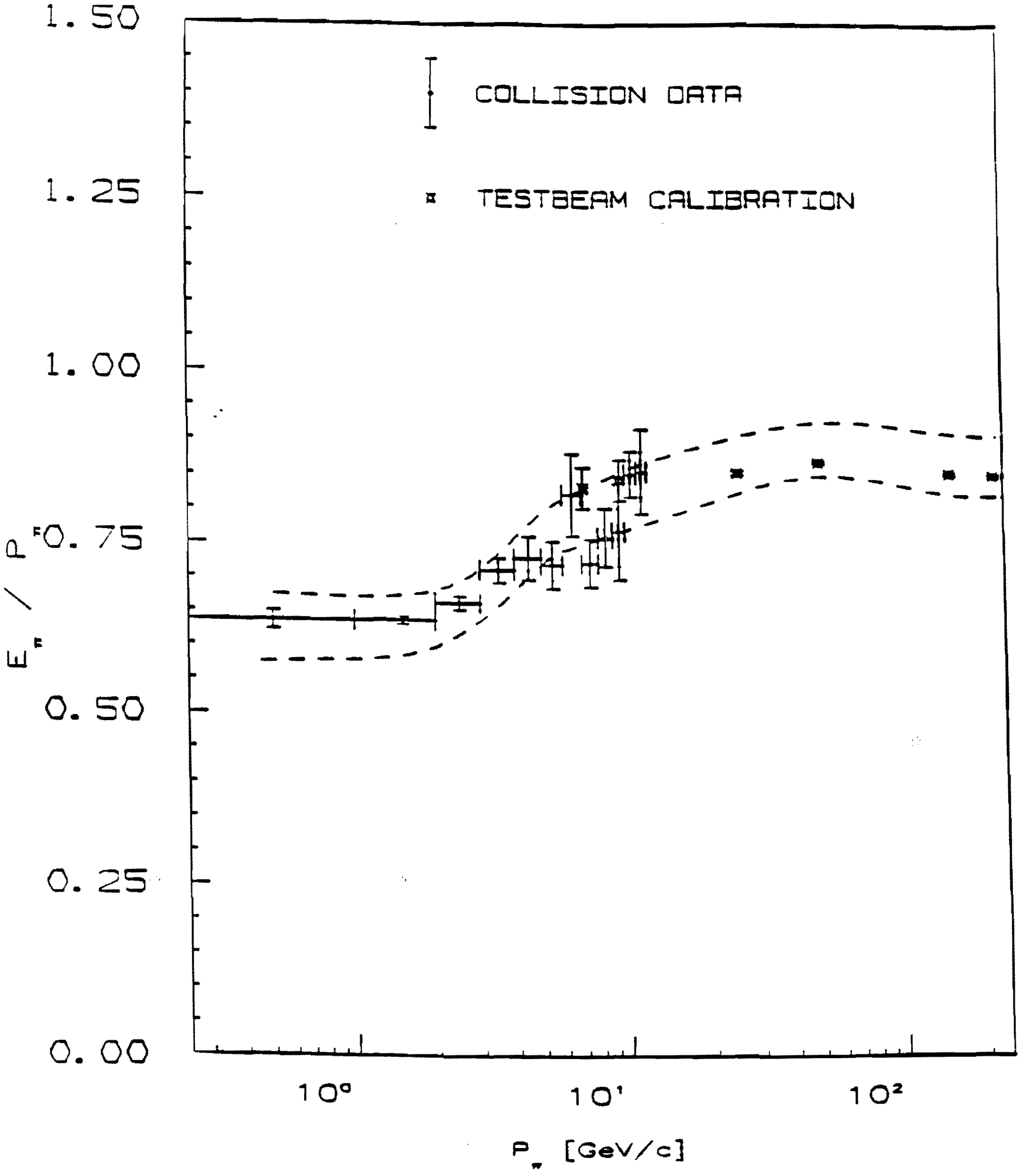

Figure 3.4: CDF central calorimeter response ($\frac{E}{p}$) to pions as a function of incident momentum. The high energy data come from test beam measurements; the low energy data ($\leq 12GeV$) come from isolated tracks in minimum bias events.

momentum. We see that low energy charged pions can be reported in the calorimeter with a fraction as low as 65% of the true energy.

- Fragmentation

  The effects of the calorimeter non-linear response on jet energy measurements can be quantified only after determination of the fragmentation properties of jets. CDF has made an attempt to determine an experimental fragmentation function.

  More than one simulation has been used to reproduce the CDF fragmentation and to estimate corrections to jet energies and momenta. Three different simulations gave corrections compatible within the estimated uncertainties.

  First of all Isajet fragmentation + detector simulation was tuned so as to reproduce experimental results [56].

  A second interesting result was the "natural" agreement (without any tuning) of Herwig version 3.2 with the CDF fragmentation [57].

  Finally a third simple simulation was implemented at CDF, able to reproduce single jet fragmetation (SETPRT, see ref. [58])

  Results of these studies have given upper and lower limits on the possible fragmentation functions. From these upper and lower bounds, systematic uncertainty was determined on the measured energy scale due to fragmentation. The most significant uncertainties come at low $E_t$ where the influence of nonlinearity is larger (see fig. 3.8).

- Cracks

  As explained in Ch. 2, crack is a generic name for uninstrumented regions of the detector.

  $\phi$ CRACKS

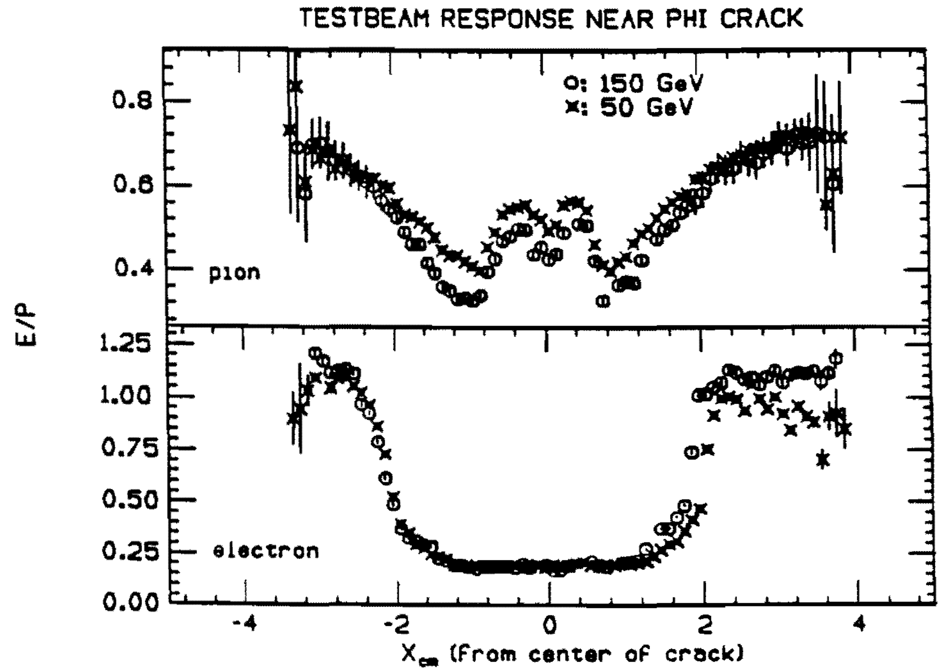

Figure 3.5: $\frac{E}{p}$ response scan of $\phi$ crack vs. distance from the center of the crack for 50 and 150 Gev pions (top) and electrons(bottom)

Test beam scan of the $\phi$ crack regions have been used to map the crack response (see fig. 3.5) using 50 and 150 GeV pions and electrons [59]. The maps are then used in the detector simulator to estimate the effective energy loss for jets. A systematic uncertainty is assigned to the energy scale due to uncertainty on the crack response.

### $\eta$ CRACKS

The $\eta$ cracks occur at boundaries between different parts of the calorimetry (e.g. central and plug) and at the gap between the two central calorimeter arches. This last $\eta$ crack (the $90^o$ crack) affects the measurements in the central calorimeter, contributing to the non-uniformity of the central calorimeter response.

We define the variable $\eta$-detector ($\eta_d$) as the pseudorapidity calculated with respect to the center of the detector instead of the event vertex. This variable

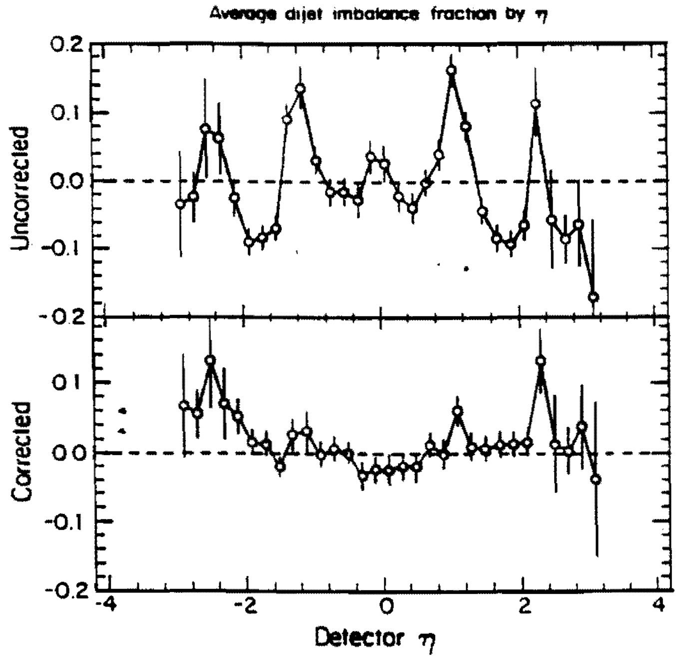

Figure 3.6: The $p_t$ imbalance of dijet events where the *trigger* jet was taken in the central region ($0.15 \leq |\eta_d| \leq 0.9$), and the *probe* jet was allowed to fall in any region of detector pseudorapidity. On the top the imbalance distribution for all jets is shown. The bottom distribution is obtained after correcting for known crack losses.

depends only on the geometry and the $\eta$ cracks fall at fixed $\eta_d$.

To scan the response of $\eta$ cracks and obtain the proper correction, the technique of dijet balancing has been used [60]. This technique relies on the fact that in events with a clear dijet topology the two jets should approximately balance in the transverse plane. A sample of clean two jet events is then selected by cutting on secondary clusters. A *trigger* jet is selected in a uniform region of the central calorimeter, while the second or *probe* jet is allowed to fall anywhere in the detector. The $p_t$ imbalance between the trigger and probe jet is then a measure of the average energy loss in various regions of the detector (see fig. 3.6). The technique is of course applicable to probe the whole calorimeter, not only the central region.

In conclusion the absolute jet energy scale is obtained in two stages. First the absolute calibration of the central calorimeter is determined. Then the gas calorimeters are equalized to the central.

The correct jet energy scale in the central calorimeter is derived using the tuned fragmentation and the detector simulation, with nonlinearity and crack responses put in properly. In the Montecarlo the "true" jet energy is obtained from those "observable" particles (leptons and hadrons) produced by the $p\bar{p}$ scattering and contained in the same cone of the clustering algorithm. In fig. 3.7 the percentage difference between the energy reported in the calorimeter ($E_{cal}$) and the "true" energy obtained from particles ($E_{part}$) is shown as a function of the "true" energy for tuned Isajet and SETPRT simulations. Both simulations agree in showing that the energy correction is substantial at low energies, a large fraction of it coming from nonlinearities.

The systematic uncertainty in the measured jet energy comes from a number of sources as stated above. Fig. 3.8 summarizes the main contributions [61].

The absolute calibration of the central detector is finally extended to the gas calorimeters by means of the dijet imbalance mapping. To this purpose a correction to the "raw" jet energies is calculated as a function of the jet $\eta$-detector ($\eta_d$ dependent correction).

## 3.2 Data selection and simulated samples

### 3.2.1 Data Sample

The data sample comes from the Tevatron collider run started on June 1988 and terminated on May 1989. During this period a total of 9 $pb^{-1}$ integrated luminosity was delivered to the B0 interaction point where the CDF detector is located, of which 4.71 $pb^{-1}$ were logged on tape. During the run the performance of the accelerator became better and better while it was tuned, resulting in a peak delivered luminosity which often exceeded the design luminosity of $10^{30}s^{-1}cm^{-2}$.

Several physics triggers have been running at the same time to provide data for different analysis. Our sample comes from the inclusive jet trigger, which requires

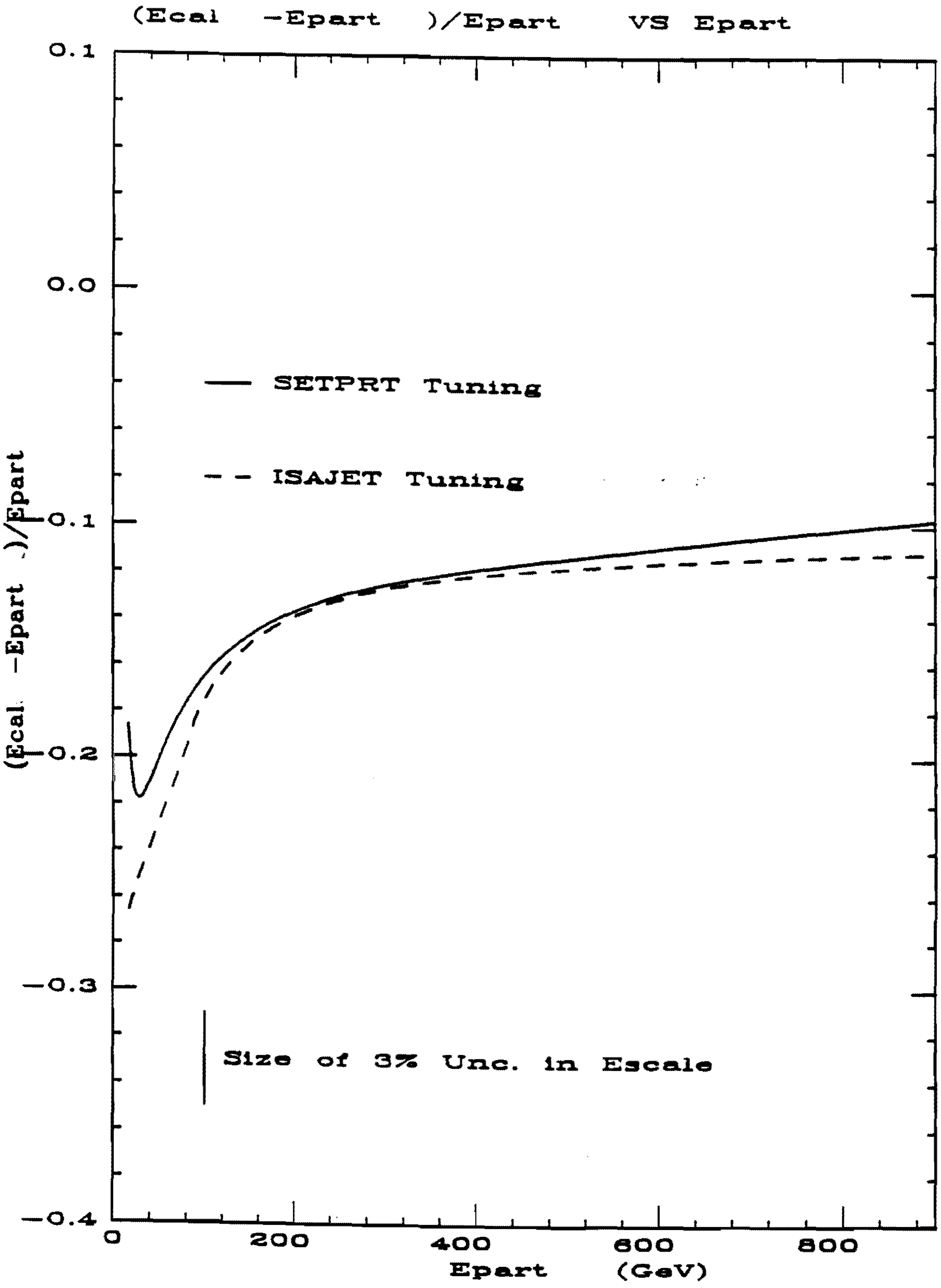

Figure 3.7: Energy corrections expressed as fractional difference of measured to "true" energy vs. the "true" energy for two of the simulations used at CDF

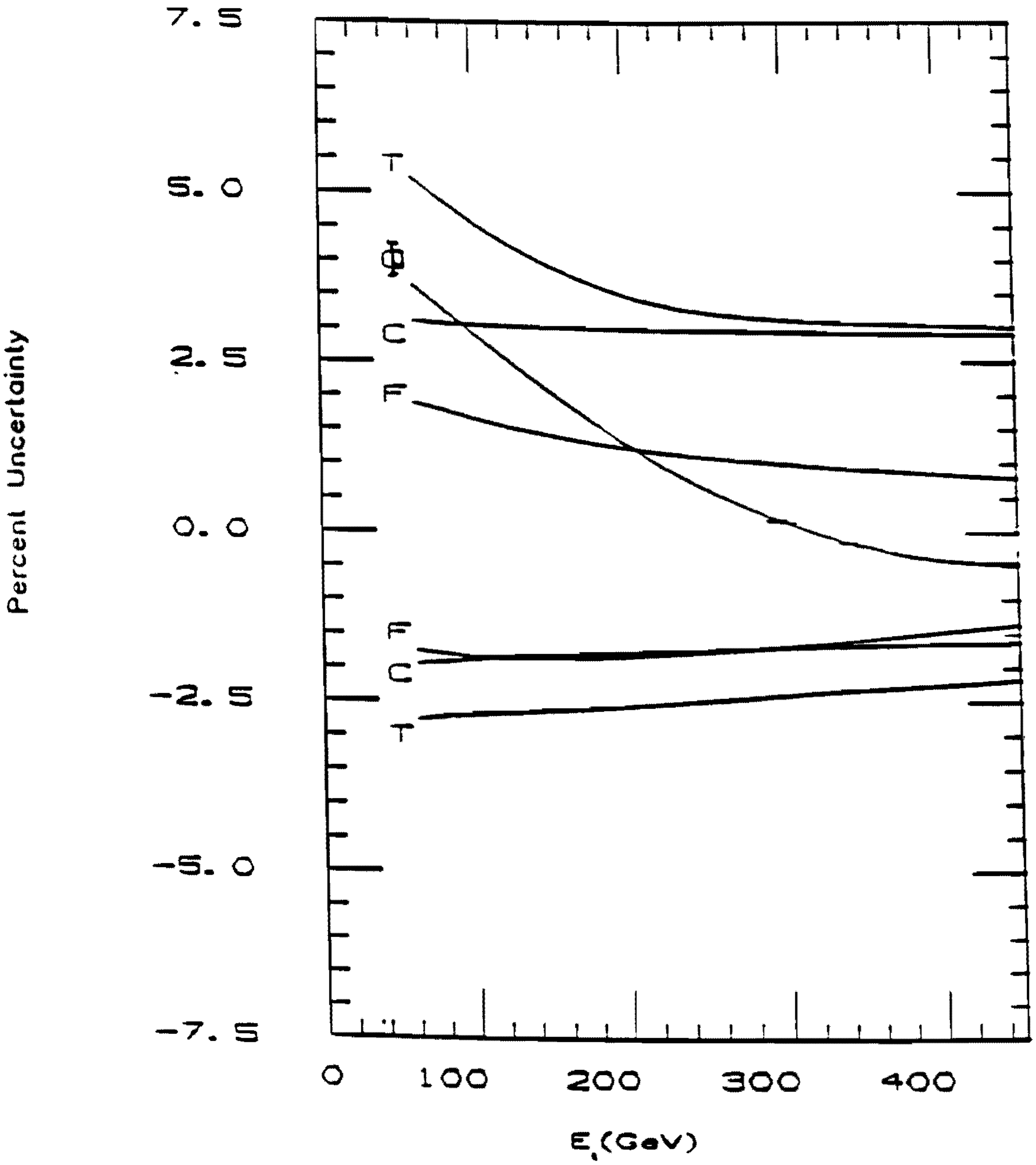

Figure 3.8: Breakdown of the various contributions to the uncertainty as functions of the corrected jet energy: total (T), $\phi$ cracks ($\Phi$), calorimeter non-linearity (C), fragmentation (F)

at least one energy cluster above a given $E_t$ threshold to be found in the calorimeter. Three different thresholds where simultaneously present, requiring 20, 40 and 60 GeV tranverse energy respectively, and named from this JET_20, JET_40 and JET_60. Since the rate has an exponential rise with decreasing threshold, JET_20 and JET_40 were pre-scaled (i.e. the rate was hardware-reduced by a given prescale factor which for most of the time was 30 for JET_40 and 300 for JET_20) while the whole JET_60 sample was recorded. Integrated luminosity recorded for the JET_60 sample (which is the most populated) was of about 4.2 $pb^{-1}$.

### 3.2.2 Background study

Events passing the inclusive jet triggers contain a large amount of fake events. By fake events we mean events in which the trigger was "misled" by jet-like structures from one or more sources of background and/or a real event was "dirtied" by too large an amount of background. Potential source of background to the jet sample are cosmic rays, main ring "splashes" and calorimeter hardware problems.

After calorimeter cleanup during the production [62,65], which eliminates most of the hardware problems and main ring splashes, cosmic rays are the largest source of fake events.

Three quantities were examined in order to study the cosmic ray background. These quantities: $EMF_{event}$, $CHF_{event}$ and $MET$ are defined in the following. Cuts were made on these quantities and events classified according to which cuts they passed and which cuts they failed [63].

The electromagnetic fraction of a jet ($EMF_J$) is defined as the ratio of the electromagnetic energy of the corresponding cluster to the total energy. Cosmic ray bremsstrahlung can release energy either in the EM or in the hadronic calorimeter, thus yelding clusters with $EMF_J$ near one or zero. The global quantity $EMF_{event}$ was redefined to be the $E_t$ weighted sum of $EMF_J$ over all the $N_{jet}$ clusters with $E_t$ above 5 GeV:

$$EMF_{event} = \frac{\sum_{J=1}^{N_{jet}} E_{tJ} \times EMF_J}{\sum_{J=1}^{N_{jet}} E_{tJ}}$$

where $E_{tJ}$ is the total transverse energy of the $J$-th jet. The $EMF$ cut is defined by $0.1 \leq EMF_{event} \leq 0.95$.

A jet is usually composed of charged and neutral particles in some proportion. Since jets are originated from the $\bar{p}p$ interactions in the center of the detector, charged particle tracks associated with the jets are then reconstructed in the CTC. In a cosmic ray event few if any CTC track will be found pointing from the event vertex to the cluster of energy generated from the cosmic ray. The charged hadron fraction of a jet ($CHF_J$) is defined as:

$$CHF_J = \frac{\sum_{i=1}^{N_t} P_{ti}}{E_{tJ}}$$

where index $i$ runs over all the $N_t$ tracks associated with the jet (i.e. pointing inside the jet cone), $P_{ti}$ are their transverse momenta measured by the CTC, and $E_{tJ}$ is defined as above. The global quantity $CHF_{event}$ was defined as:

$$CHF_{event} = \frac{\sum_{J=1}^{N_{jet}} CHF_J}{N_{jet}}$$

where the sum extends to all the $N_{jet}$ jets with $E_t > 10GeV$. The $CHF$ cut is defined by $CHF_{event} \geq 0.175$.

The third quantity is based on the following considerations: since the colliding partons inside the proton and antiproton have little momentum transverse to the beam direction ($P_t$), a real jet event will have jets which balance approximately in $P_t$. Cosmic rays usually deposit their energy in a single cluster, or if they can manage to form two separate clusters, the azimuthal separation generally is not such as to give a balance in $E_t$. The missing transverse energy $\not{E}_t$ is defined as:

$$\not{E}_t = \sqrt{(\sum_{J=1}^{N_{jet}} E_{tJ} sen\phi_J)^2 + (\sum_{j=1}^{N_{jet}} E_{tJ} cos\phi_J)^2}$$

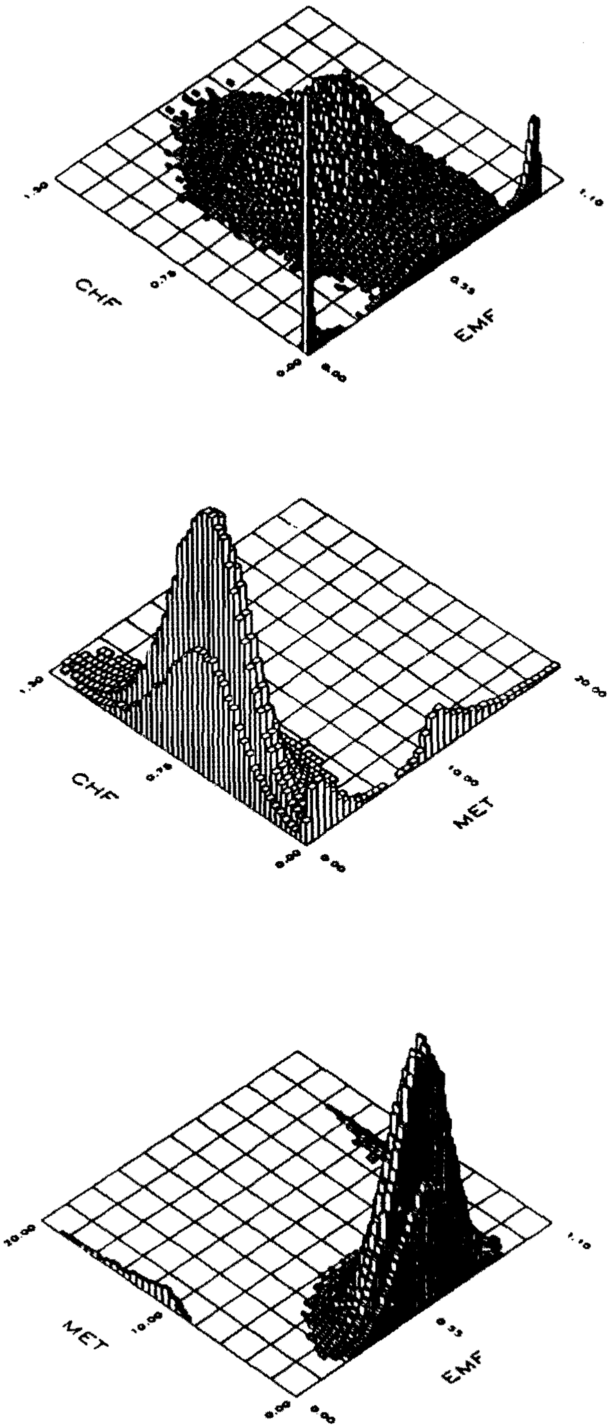

Figure 3.9: Correlation between the quantities used to tag cosmic background

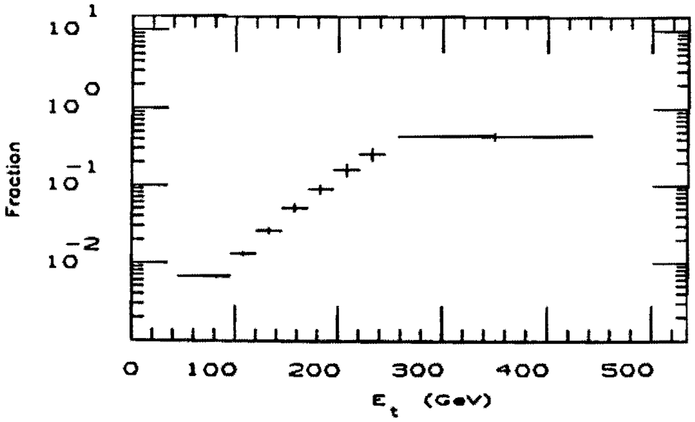

Figure 3.10: Ratio of background $E_t$ differential cross section to the total $\frac{d\sigma}{dE_t}$ cross section.

where $N_{jet}$ is the number of jets in the event with $E_{tJ} > 5GeV$, and $\phi_J$ is the azimuth of the axis of jet $J$. The *missing* $E_t$ *significance* ($MET$) is defined as follows:

$$MET = \frac{\not{E}_t}{0.8 \times \sqrt{\sum_{J=1}^{N_{jet}} E_{tJ}}}$$

with $N_{jet}$ as above. $MET$ is a measure of the jet missing $E_t$ in number of standard deviations. The $MET$ cut is defined by $MET \leq 6.5$.

Fig. 3.9 shows the correlations between $EMF_{event}$, $CHF_{event}$ and $MET$. Observing these plots it becomes clear that the majority of the events tends to satisfy at least two of the $EMF$, $CHF$, and $MET$ cuts, while the rest of the events form isolated islands in the plots where cosmic ray backgrounds are expected to fall.

On a data subset of 845 $nb^{-1}$ and with jets reconstructed using a cone radius of 0.7 a study was made classifying the events on the basis of the above cuts. Since real physical events are expected to fail at most one of them, while cosmic ray events are expected to fail the majority of them, events were classified as jet events if passing at least two of these cuts.

Fig. 3.10 shows the ratio of the cross section $\frac{d\sigma}{dE_t}$ for background events determined using the cuts above to the total jet cross section. From fig. 3.10 it is clear that the cross section for the background is much less steep than the inclusive jet

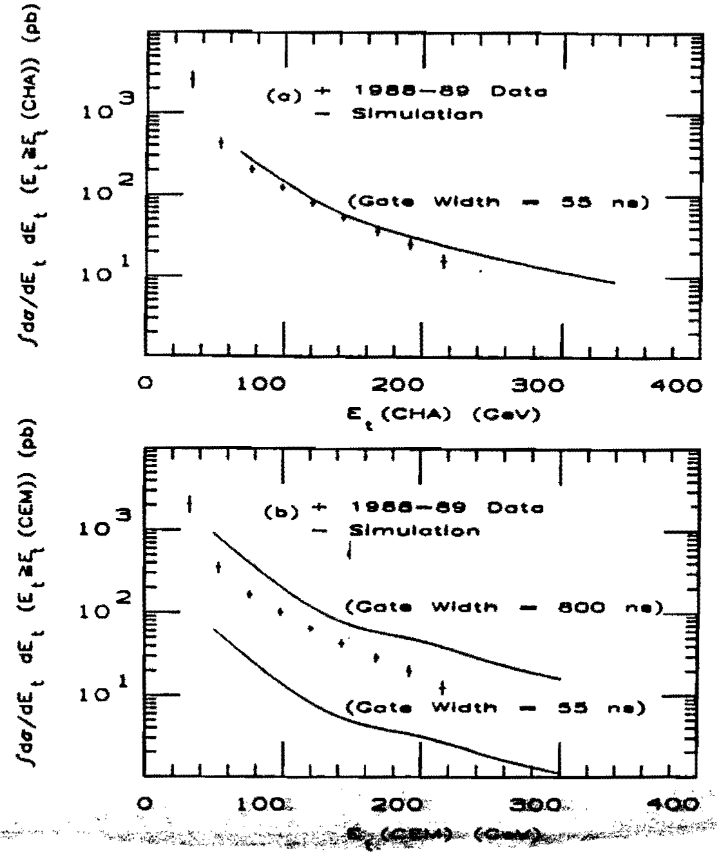

Figure 3.11: Cosmic ray event rates and comparison to MC predictions in a) CHA and b) CEM.

$\frac{d\sigma}{dE_t}$. Therefore the relative background is larger at large values of $E_t$.

The expected cosmic ray background at CDF has been investigated using a Montecarlo simulation [64]. The expected rates in the central hadronic and electromagnetic calorimeter were calculated and the cross sections thus obtained compared to the results from the study described above. Fig. 3.11 shows the comparison of the background cross section to the prediction of the MC. The agreement between predicted rates and data shows the efficiency of the cuts in tagging cosmic background.

The result shown in fig. 3.10 is important for the analysis described in Chapter

5. There we select events with leading jets with transverse energy typically of order 100 GeV. Looking at fig. 3.10 we see that the cosmic ray background is few percents for $E_t$ in the region of 100 GeV. Therefore we expect a negligible contribution to come from this background. This allows to use a looser filtering procedure that, not exploiting the tracking information, has the advantage of being applicable also to events where jets are not central. Our filtering procedure rejects events satisfying the following condition:

$$((EMF_1 < 0.05).OR.(EMF_1 > 0.95).OR.$$
$$(EMF_2 < 0.05).OR.(EMF_2 > 0.95)).AND.(MET > 6)$$

where MET is defined as above, $EMF_i$ is the electromagnetic fraction of jet $i$ and jets are numbered in order of decreasing transverse energy.

### 3.2.3 Kinematic cuts

LEADING JET PSEUDORAPIDITIES.

As previously discussed in Chapter 2 the CDF calorimeter has different structural characteristics (and therefore different response) depending on the pseudorapidity region under consideration. The three main regions (central, endplug and forward/backward) give considerably different response. To optimize the jet energy measurement and to ensure homogeneity in the data used for our analysis the cut $|\eta_1|, |\eta_2| < 0.7$ was applied to the data sample, thus selecting the two leading jets in the central calorimeter (jets are numbered with decreasing transverse energy). This choice is consistent with those made in most of the inclusive cross-section analyses of jet events at CDF. Fig. 3.12 shows the scatter plot $\eta_1$ vs.$\eta_2$ of the full sample; also indicated are the positions of the pseudorapidity cuts.

COLLINEARITY

Since our study of QCD radiation is mainly based on comparisons of data distributions and Shower Montecarlo predictions, and being Shower Montecarlos a

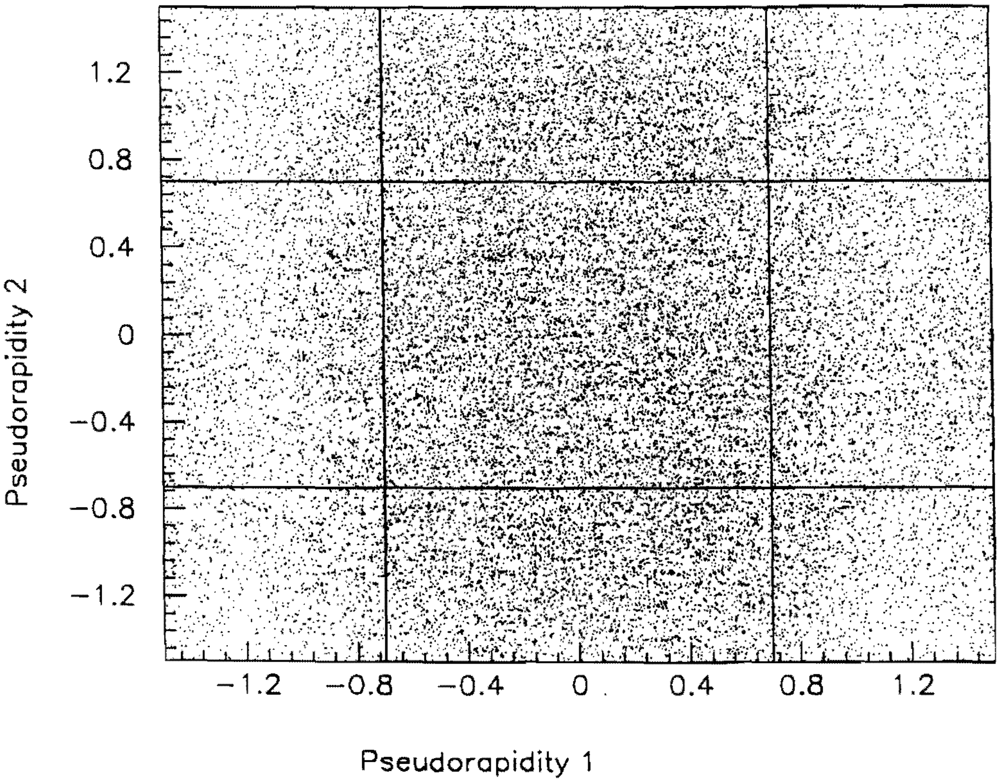

Figure 3.12: Scatter plot of pseudorapidity of first vs. second jet from the full data sample. Also indicated are the positions of the pseudorapidity cuts.

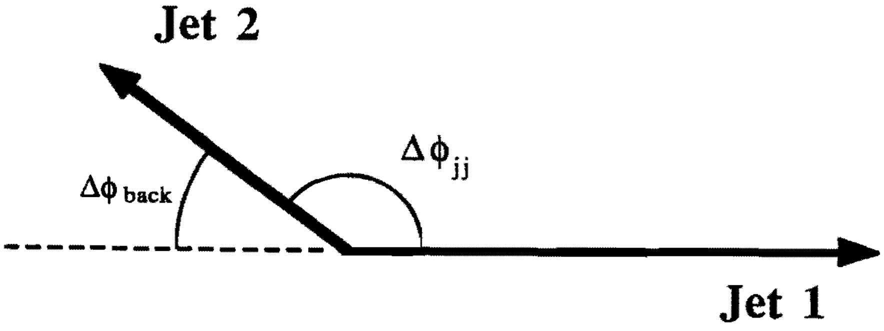

Figure 3.13: Definition of $\Delta\phi_{back}$.

realization of the Leading Logarithmic Approximation (LLA) which is not able to correctly describe large $p_t$ branchings, we would like to get rid of events having too striking a topology of high order processes. We would like at least to discard the so-called "Mercedes-like" three jet events, that is events with three jets approximately $120^o$ apart from each other and having similar energies. A variable useful to discriminate such events is $\Delta\phi_{back}$, the angular deviation of the two leading jets from being back-to-back in the transverse plane (see fig. 3.13). Clean two-jet events come from the final state of $2 \rightarrow 2$ processes and since there is no boost in the transverse plane they should be exactly back to back in this plane ($\Delta\phi_{back} = 0$). Actually, even clean two-jet events with no radiation, because of detector resolution would result only approximately back to back. Clear 3 jet events coming from the $2 \rightarrow 3$ processes will be characterized instead by large values of $\Delta\phi_{back}$. There is no substantial theoretical support for a specific value of the $\Delta\phi_{back}$ cut. We requested in our sample that the two leading jets be back to back within $20^o$ in $\phi$ (see fig. 3.14). From the distribution shown in fig. 3.14 it is apparent that this is a loose cut.

### 3.2.4 Simulated samples

We used the programs Herwig version 3.2 [73], and Isajet version 6.25 [78], to generate jet events successively processed through QFL Version 3.10 [66], the CDF detector simulator. Two types of samples were generated using Herwig: one with a flat distribution of the final state parton $p_t$'s for use in energy scale and resolution studies discussed in Chapter 4 (sect. 4.3) and one with parton $P_t$ spectrum as predicted by perturbative QCD. The Isajet sample was generated with the parton $P_t$ spectrum of QCD. To increase the statistics at large $P_t$ several samples with increasing parton $P_t$ thresholds were generated. The samples were joined together after an appropriate selection to avoid the biasing due to the generation cuts. Dijet invariant mass spectra (or, depending on the specific analysis, transverse energy spectra of the leading jets), normalized for the simulated integrated luminosity data,

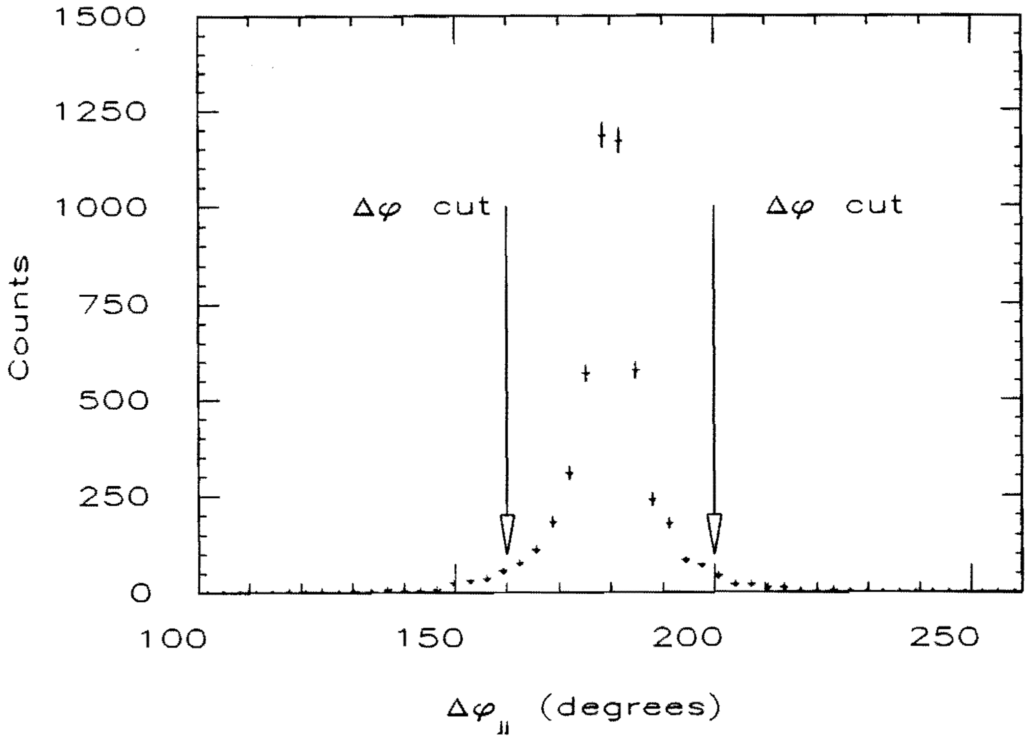

Figure 3.14: $\Delta\phi_{jj}$ distribution. The position of the $\Delta\phi$ cut is indicated.

were then obtained and compared to determine the proper cuts. As an example fig. 3.15 shows the dijet invariant mass spectra for various samples. Each cut is made at the value were two subsequent spectra start to overlap and the non-biased regions joined together to obtain a continuous spectrum.

Since our analysis only involves central leading jets, to achieve high statistics with the least possible CPU-time, we constrained final state partons in the rapidity interval [-1.5,1.5]. This should be a safe generation cut since we will require leading jet pseudorapidities within [-0.7,0.7], following the same analysis path used for real data. To check for bias due to this generation cut fig. 3.16 shows the parton pseudorapidity distribution for events selected with leading jet pseudorapidities within [-0.7,0.7]. The distribution is not affected by the generation cut in pseudorapidity.

Finally higher statistics samples for both Herwig and Isajet were generated with transverse momenta of the final state partons greater than 75 GeV. We generated 5.9 $pb^{-1}$ integrated luminosity with Isajet and 5.5 $pb^{-1}$ with Herwig. This gives us

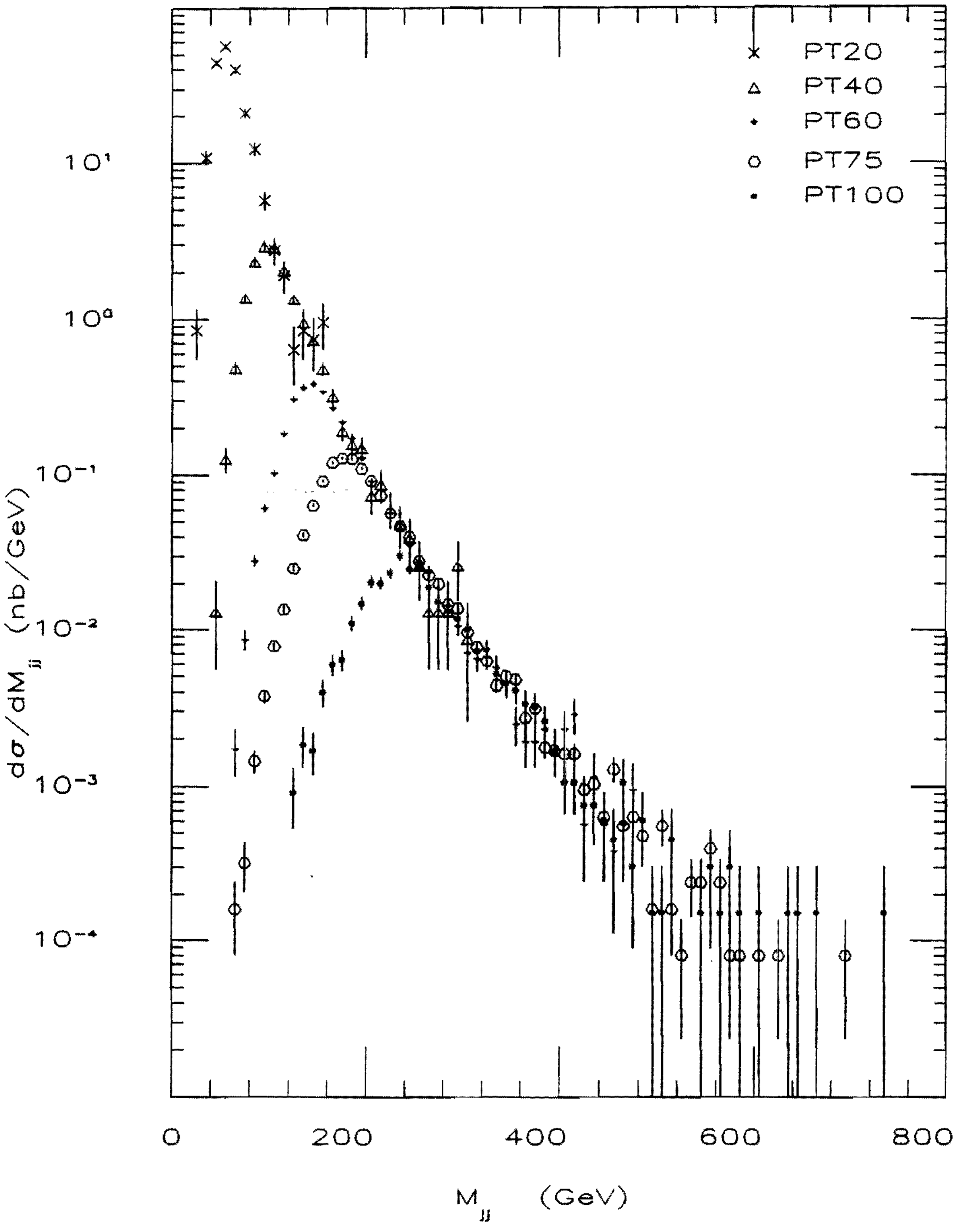

Figure 3.15: Invariant dijet mass spectrum for the various subsamples generated. Each sample was cut at the $M_{jj}$ value where the adjacent spectrum started to overlap.

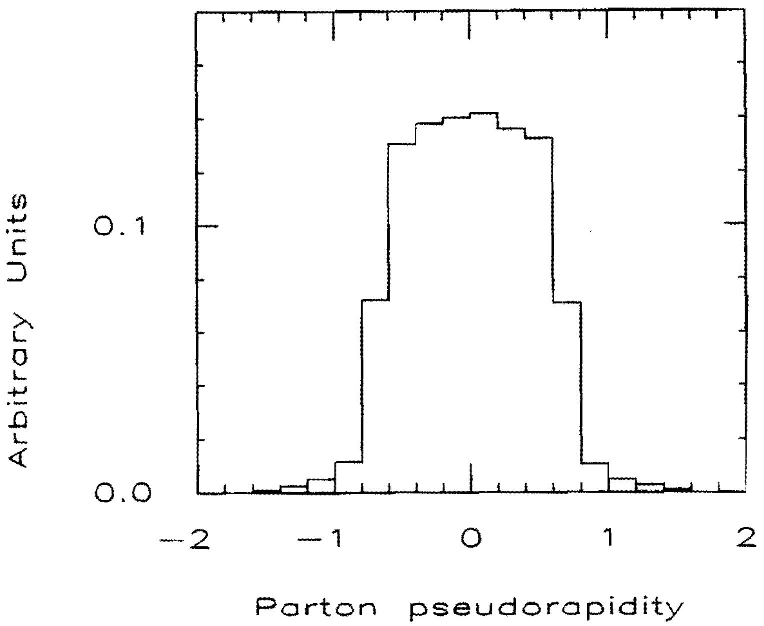

Figure 3.16: Parton pseudorapidity distribution for the events generated in the parton $\eta$ interval [-1.5,1.5], but leading jets in the $\eta$ interval [-0.7,0.7]

high statistics similar to the JET_60 data sample which profits of the total 4.2 $pb^{-1}$ integrated luminosity. The 75 GeV $P_t$ cut was chosen so that the cuts to be applied on simulated samples to get rid of generation bias were equal to those applied on the JET_60 sample to avoid the trigger bias.

### 3.2.5 Simulated events vs. real data

To check our simulated samples, several distributions of leading jet quantities were studied. Pseudorapidity distributions of the two leading jets for both simulations and data (JET_60) are shown in fig. 3.17. Comparison of the leading jet $E_t$ spectra for Herwig, Isajet and data is shown in fig. 3.18. These checks give quite satisfactory results, showing that both the generators and the detector simulator are properly tuned.

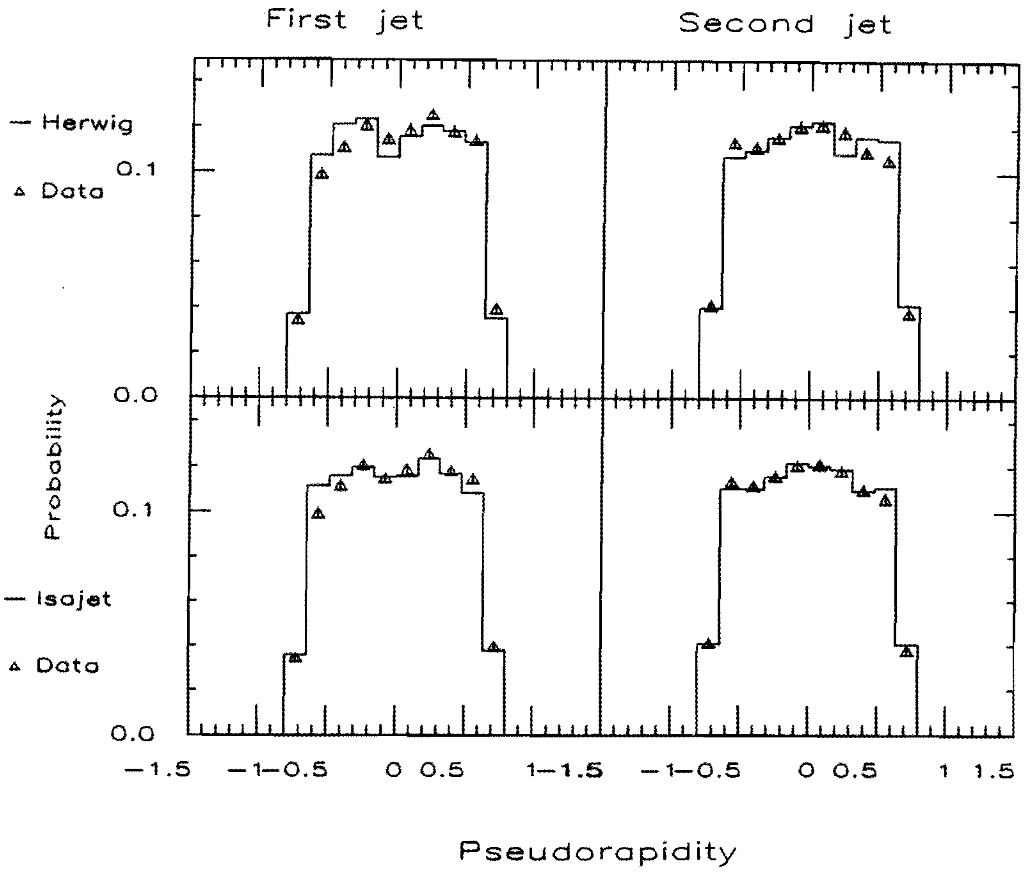

Figure 3.17: Comparison between simulated (solid line) and measured (triangles) pseudorapidity distributions of the two leading jets.

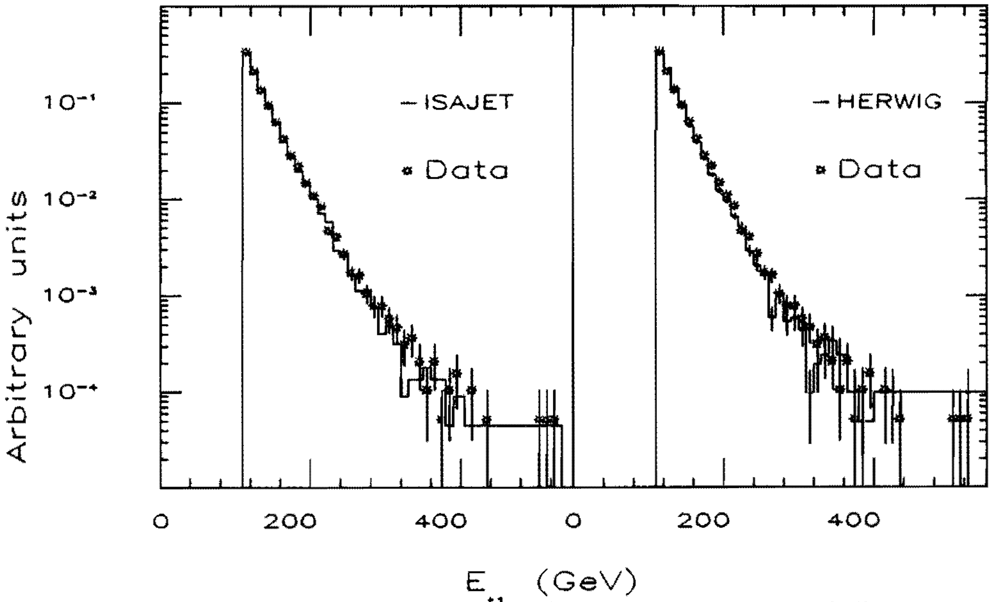

Figure 3.18: Comparison between simulated (dots) and measured (histogram) $E_t$ spectra of the leading jet.

# Chapter 4

# Effects of QCD radiation on jet measurements

## 4.1 Importance of radiation

Many inclusive features of jet events are reasonably approximated by the simple model of the 2 → 2 process (Leading Order calculations), and it is important to understand what can be described by this approximation [67].

However this simple scheme needs often to be integrated to come to a more precise understanding of jet events. Variables like the jet event multiplicity or the jet shape cannot be explained by a simple 2 → 2 process. Perturbative QCD allows to make more precise predictions taking into account higher order contributions (see Chapter 1).

The ability to describe higher order effects, like gluon radiation, is important to test perturbative QCD and has contributed to change the relation between theoretical predictions and experimental measurements (see Chapter 3 sect. 1).

In the past the experimental jet definition was oriented to reproduce as much as possible the Born Level approximation of the hard process. The jet energy measurement (affected by gluon radiation, fragmentation and underlying event) was corrected to try to reproduce the simple theoretical LO approximation. A clear example is given by the *underlying event correction* and the *out of cone correction.*

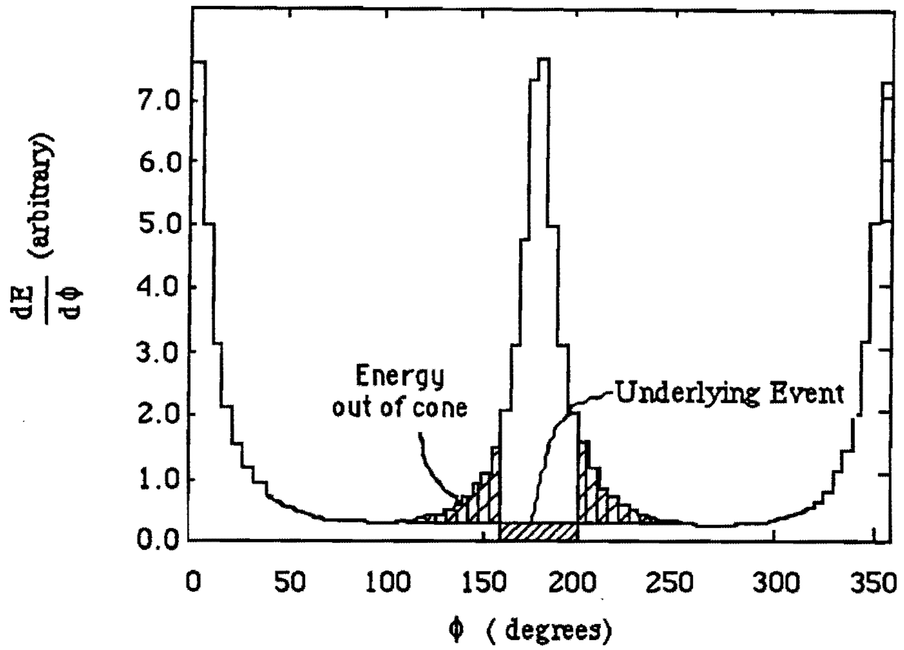

Figure 4.1: Transverse energy deposited in the central calorimeter as a function of the azimuthal angle from the event thrust axis. The minimum at 90° was taken to be the energy contribution from the underlying event. The cross hatched region at $\simeq 40^o$ would be roughly the amount of energy lost outside the clustering cone of radius 1.0

In fig. 4.1 the average transverse energy flow around the leading jet axis is plotted as a function of the $\phi$ distance from this axis. The back to back structure is characteristic of dijet final states. This plot has been obtained by selecting a set of clean two-jet events, i.e. cutting on third jets. The energy density at the local minimum at $90^o$ from the thrust axis was taken in the past as the average underlying event energy density and the corresponding amount of energy falling in the jet cone (dashed in fig. 4.1) was subtracted to the jet energy as not belonging to the original parton(underlying event correction). The *energy out of cone* is the average energy falling outside the clustering cone and in excess of the underlying event energy (cross hatched area in fig. 4.1). This energy was once considered as belonging to the original parton, and therefore summed to the jet energy (out of cone correction). This procedure is reasonable for the specific leading order the theory is calculated to.

The improvement of theoretical calculations, which makes available higher order

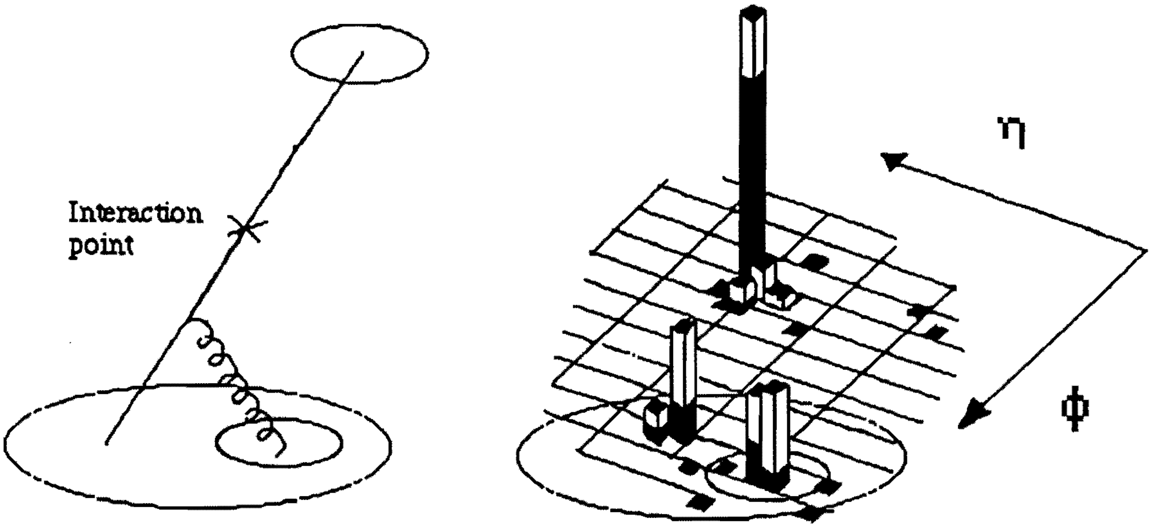

Figure 4.2: Jets as seen in NLO theory and in experiment.

predictions, suggests the use of a more general procedure, independent of the present level of the theoretical technique: the jet is operatively defined by the flux of energy in a limited and well defined phase space region (Chapter 3, section 1) and the aim of theoretical calculations is to predict what is observed at the jet level (not at the parton level). A step in this direction has been recently done with the NLO calculations (see section 3 of Chapter 1) which indeed allow a third parton in the final state, in the attempt to describe the observation of more than two clusters in the event as well as the finite size of the jets. Fig. 4.2 illustrates this attitude. In such a case for a given choice of cone size two of the three clusters may be merged together if close in the $\eta - \phi$ space, but the theory can account for this because the corresponding partons will also be merged and eventually the predicted cross sections shall depend on the cone size.

Let's come now to another simple example that put in evidence the importance of the radiation effects. In fig. 4.3 the production of an intermediate particle (e.g a W boson) decaying in two quarks is shown. The partons will generate jets and the intermediate particle is searched as a resonance giving at least two jets in the event.

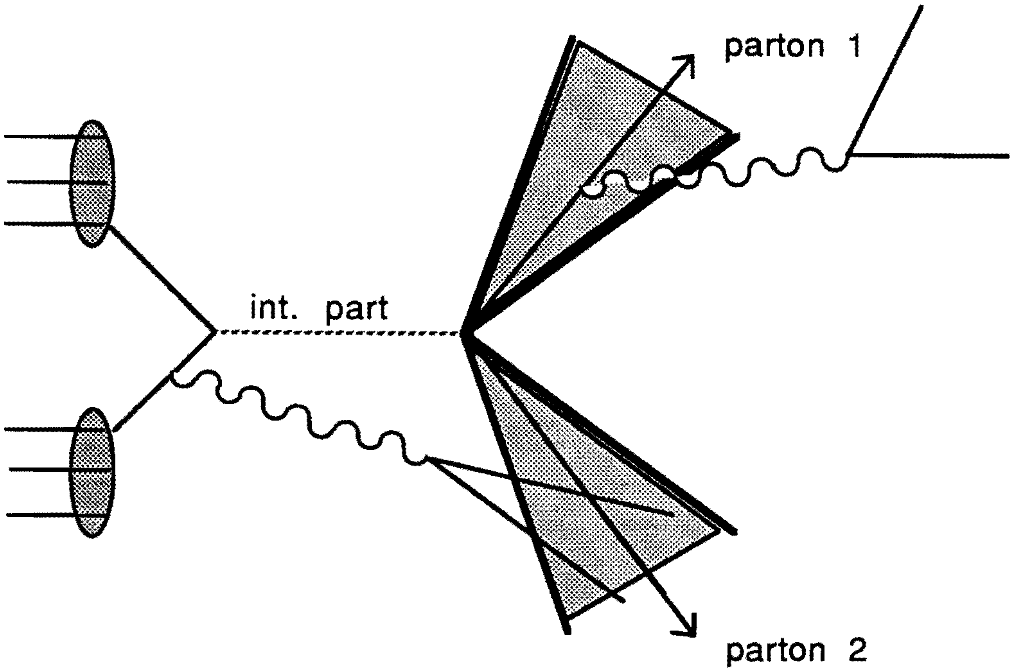

Figure 4.3: Production of an intermediate particle decaying into two jets

The measured jets are obtained from the fixed cone algorithm. Fig. 4.3 sketches such cones around the final state parton directions. Part of the final state parton energy can be lost out of the cones, possibly giving rise to secondary jets. It can also happen that energy radiated from the initial state enter the cones, causing an excess in the measured energy. In reconstructing the mass of the intermediate particle it is important to include radiation lost from the final state partons and to exclude initial state radiation, to achieve the best resolution and minimize the mass offset. The two leading jets are the obvious candidates to represent the final state partons, but what about the secondary jets in the event? Should they be included in the event mass definition or should they be excluded? The impossibility of deciding for each secondary jet whether it derives from initial or final state radiation is what makes the measurement more difficult.

We study in this chapter the QCD radiation with the help of shower Montecarlos. We look in particular at the difference between the invariant mass of the scattered partons of the $2 \rightarrow 2$ process ($M_{partons}$), and the measured invariant mass $M_{jj}$ of the system composed of the two leading jets. In the attempt to recover the final state radiation belonging to the hard scattering and to exclude the initial state radiation, only a statistical separation can be obtained and the jet cone size is to be optimized. We will show that the radiation affects the inclusive cross section measurements, introducing a strong dependence on the clustering cone size.

## 4.2 Spatial correlation between radiated energy and final state partons

We used a subset of the ISAJET sample (see section 2 of Ch. 3) to study the radiated energy in relation with leading jets. The scatter plot of fig. 4.4 refers to the secondary partons produced at the last stage of the shower development of the final state, and each entry is weighted by the parton energy. We will use the word 'son' to indicate any such secondary parton, and the word 'parent' to indicate the final state parton of the $2 \rightarrow 2$ process initiating the shower. The horizontal axis in the scatter plot represents the $\phi$ distance ($\Delta\phi = \phi_{son} - \phi_{parent}$) between the son and the parent parton; the vertical axis represents the $\eta$ distance ($\Delta\eta = \eta_{son} - \eta_{parent}$) between the same partons. The parent parton position in this plot is at the origin. Projections of the scatter plot on the two axes are also shown in fig. 4.4. Fig. 4.4 shows that most of the final state radiation is confined inside a narrow cone around the parent parton. Nonetheless a certain amount of energy from the final state will fall outside the clustering cone even with the choice $R_{cone} = 1$. For comparison fig. 4.5 shows the distribution of sons generated from initial state partons with respect to one of the final state partons (chosen at random), weighted by the son energy.

It is clear that no correlation is found between initial state radiation and final state parton directions. It is also clear that any nonzero choice of the clustering cone radius will result in including a fraction of the energy radiated by the initial state; anyway comparison with fig. 4.4 indicates the choice of $R_{cone}$ affects the fractions of initial state and final state radiation that will be included in the leading jets.

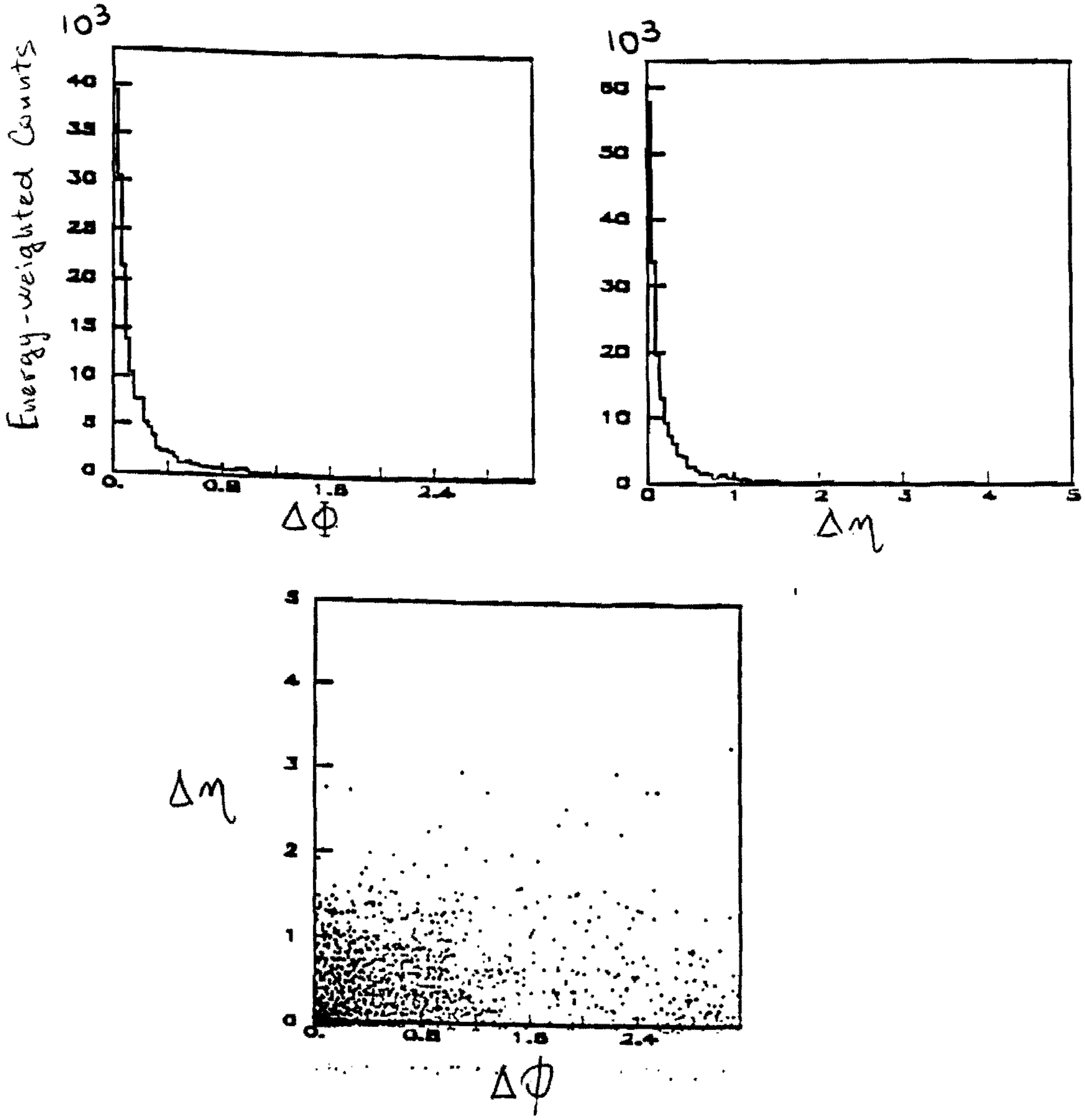

Figure 4.4: $\Delta\eta - \Delta\phi$ distribution of secondary partons radiated from the final state. Most part of the radiation from the final state is confined inside a cone around the parent parton

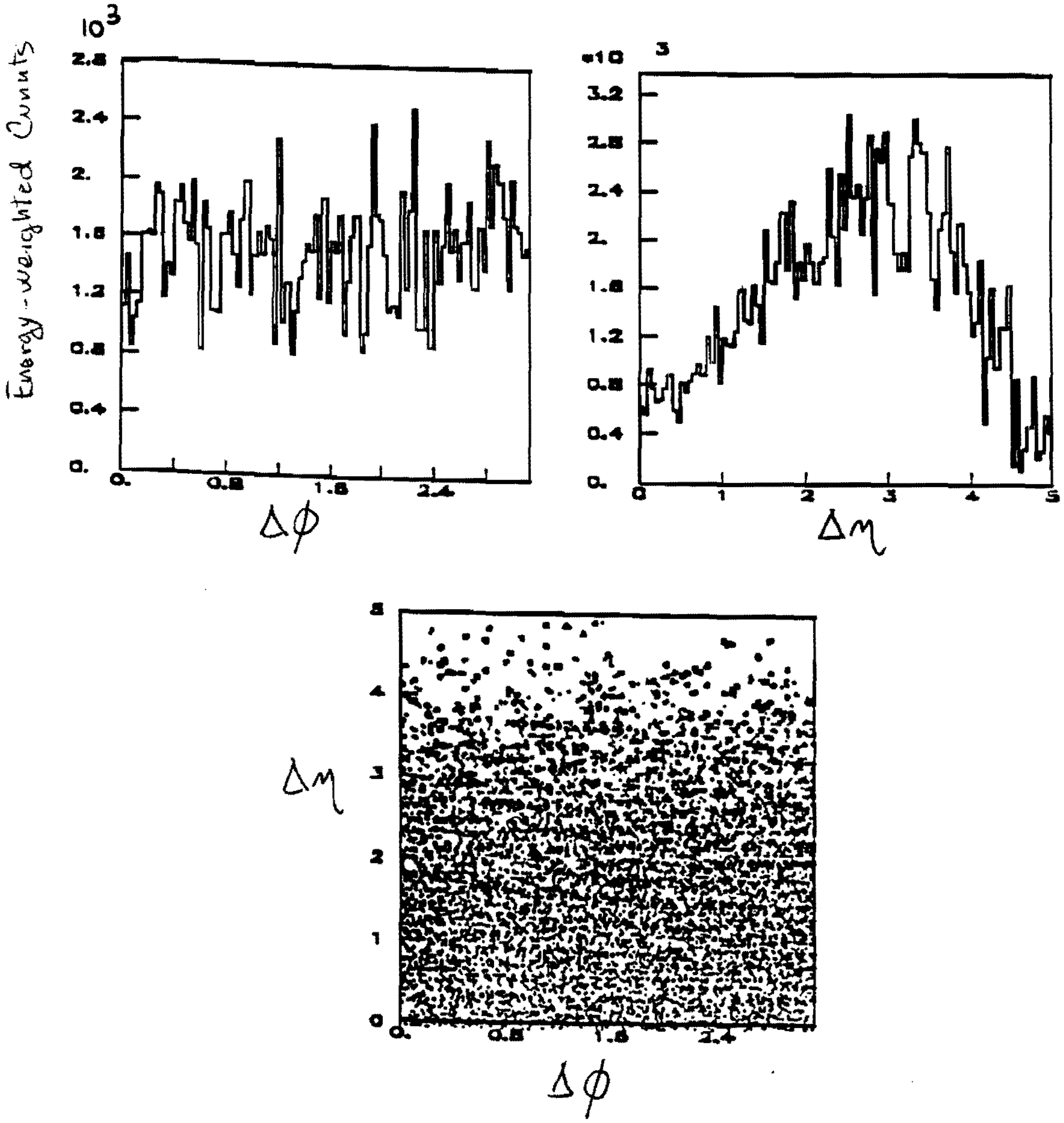

Figure 4.5: Distribution of secondary partons radiated from the initial state with respect to a final state parton

## 4.3 The influence of radiation on the dijet invariant mass

We used the Herwig simulated sample with flat parton $P_t$ distribution (see Chapter 3), to study the effects of radiation on the scale and resolution of dijet invariant mass ($M_{jj}$) measurements. The detector simulation and the clustering algorithm were run on the generated events. We computed the *measured dijet mass* $M_{jj}$ using the 4-momenta of the two leading jets as given by the clustering algorithm, without applying the jet corrections for detector response (i. e. cracks, non linearity etc.). Then, using the information provided by the generator Herwig, we reconstructed the *true dijet mass* according to two different definitions:

a) The mass that would be observed with a perfect detector: this is obtained by summing the 4-momenta (provided by Herwig) of all the particles exiting the primary vertex inside the clustering cones of the two leading jets and calculating the invariant mass of the total 4-momentum ($M_{particles}$). This definition follows the modern course of considering the jets as the result of the clustering algorithm. The measured mass $M_{jj}$ differs from $M_{particles}$ only because of detector effects.

b) The invariant mass of the hard $2 \rightarrow 2$ process ($M_{partons}$), before the shower evolution. This definition is particularly important for production of an intermediate particle decaying into two partons. In this case $M_{partons}$ is actually the mass of the produced particle. The measured mass $M_{jj}$ differs from $M_{partons}$ not only for detector effects, but also for radiation effects (see fig. 4.3). When data are directly compared to the LO predictions, it is important to fully understand the difference between $M_{jj}$ and $M_{partons}$ , because the measurement refers to $M_{jj}$ and the calculations to $M_{partons}$.

In the following, the comparison between the curves obtained with definition a) to those obtained with definition b) will help to disentangle the effect of radiation from that of the detector only.

Fig. 4.6 shows the average relative difference $< M_{jj} - M_{true} > /M_{true}$ versus $M_{true}$ for both definitions a), b). $M_{jj}$ is obtained with a clustering cone radius $R_{cone} = 1$. The relative difference $< M_{jj} - M_{partons} > /M_{partons}$ is negative and few percents less than $< M_{jj} - M_{particles} > /M_{particles}$. This means that, in the Herwig approximation, even with a cone radius $R_{cone} = 1$ the effect of the losses out of the cone is in average larger than the effect of the energy collected from the initial state radiation into the jets.

Fig 4.7 shows the mass resolution $\sigma(M_{jj} - M_{true})$ as a function of $M_{true}$. The fluctuations on the initial/final state radiation respectively included/excluded from the jets, make the distribution of the difference $M_{jj} - M_{partons}$ substantially wider than the distribution of $M_{jj} - M_{particles}$, where only detector effects contribute.

Let us see now how the above effects depend on the cone size. In fig.4.8a) the average relative differences $< M_{jj} - M_{partons} > /M_{partons}$ are plotted vs. $M_{partons}$ for three different values of $R_{cone}$ (1.0, 0.7 and 0.4). Fig. 4.8b) shows the corresponding $< M_{jj} - M_{particles} > /M_{particles}$ plotted vs. $M_{particles}$.

We note that the dependence on the cone size is much greater in fig. 4.8a) than in fig. 4.8b), indicating (and measuring) the sensitivity of the out of cone radiation to the cone size. The mass difference between the measurements with $R_{cone} = 1$ and $R_{cone} = 0.4$ is about 10% and it is not significantly dependent on the mass value. The small dependence on the cone size shown in fig. 4.8b) is reversed with respect to fig. 4.8a). This is probably due to the jet core particles, which dominate the $R_{cone} = 0.4$ measurement and are better measured because of their greater momentum.

The plots in fig. 4.9a) and 4.9b) respectively show the values of $\sigma(M_{jj} - M_{partons})$ vs. $M_{partons}$ and $\sigma(M_{jj} - M_{particles})$ vs. $M_{particles}$ for the three different values of $R_{cone}$. These plots evidence only at large masses a small dependence of the mass resolution on the cone size.

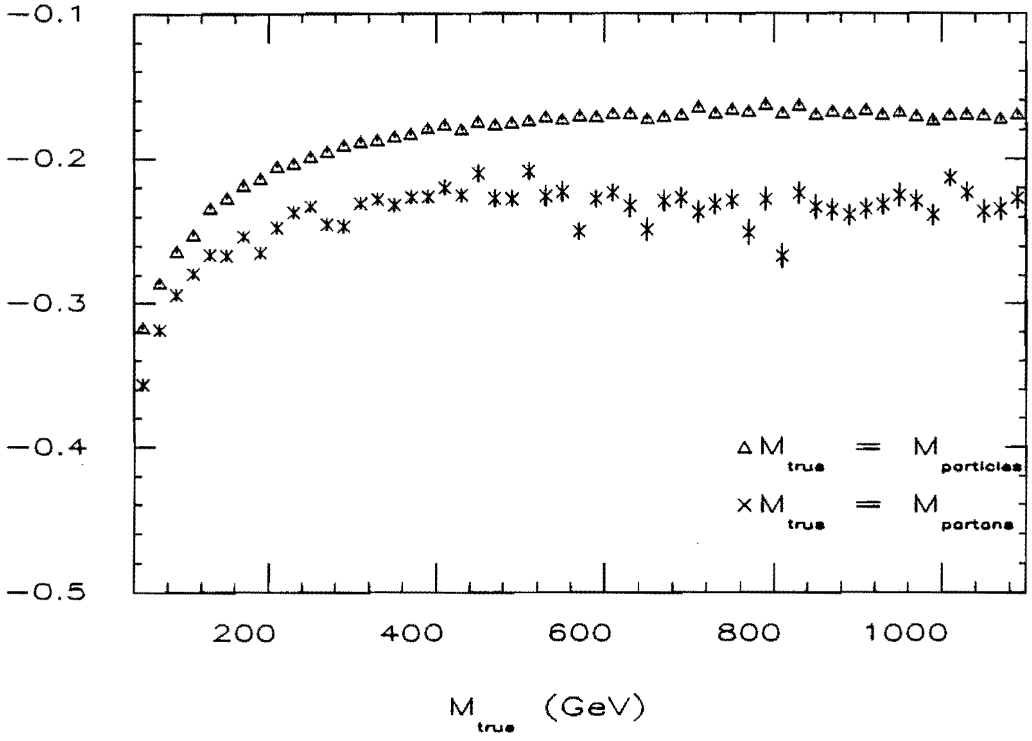

Figure 4.6: $< M_{jj} - M_{true} > / M_{true}$ versus $M_{true}$

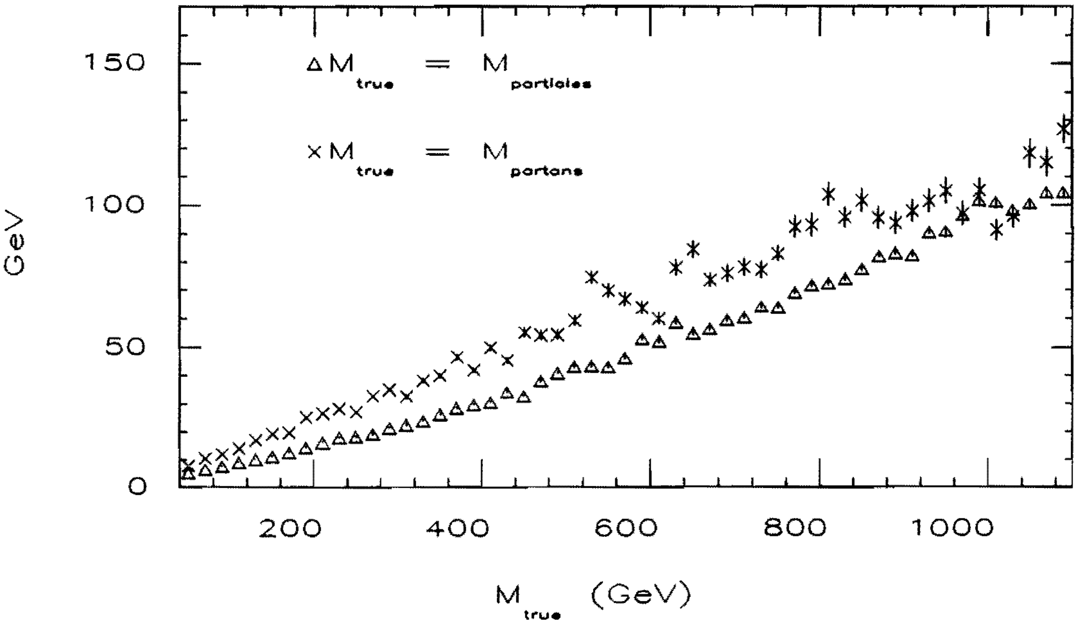

Figure 4.7: $\sigma(M_{jj} - M_{true})$ as a function of $M_{true}$

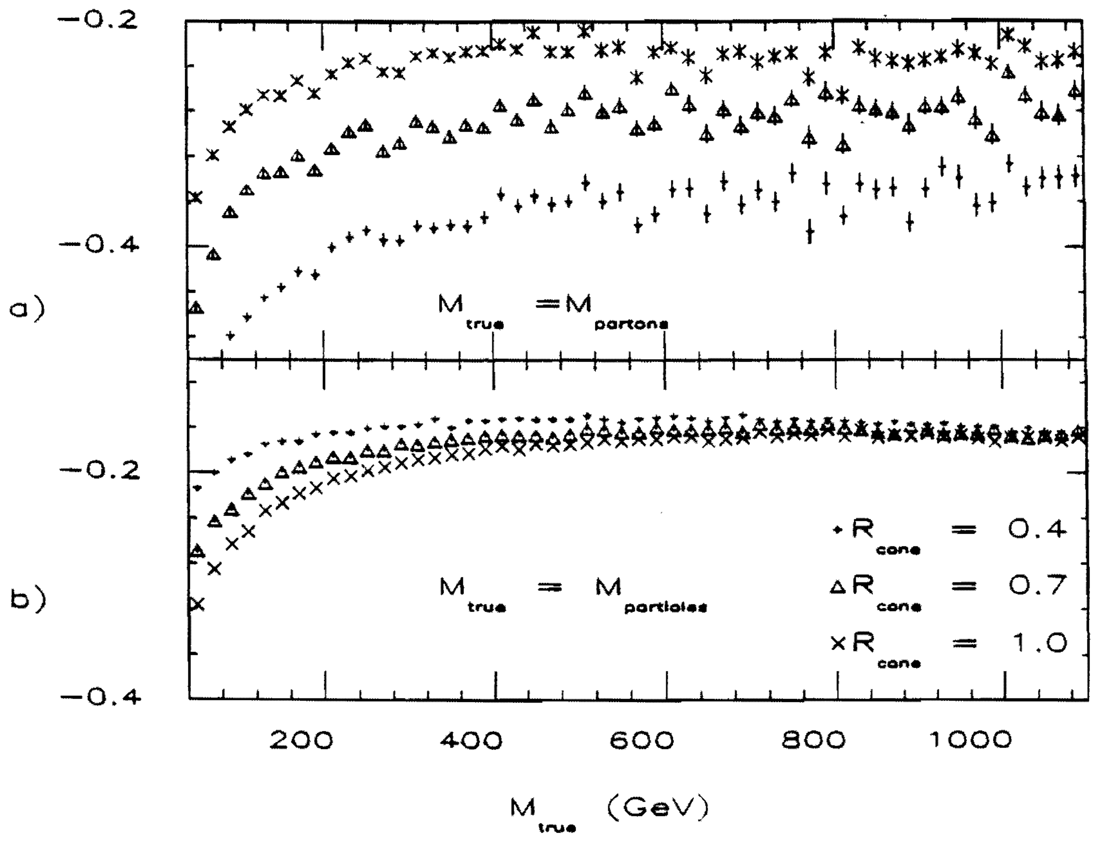

Figure 4.8: $< M_{jj} - M_{true} > / M_{true}$ versus $M_{true}$ for a) the "partons" true mass and b) the "particles" true mass.

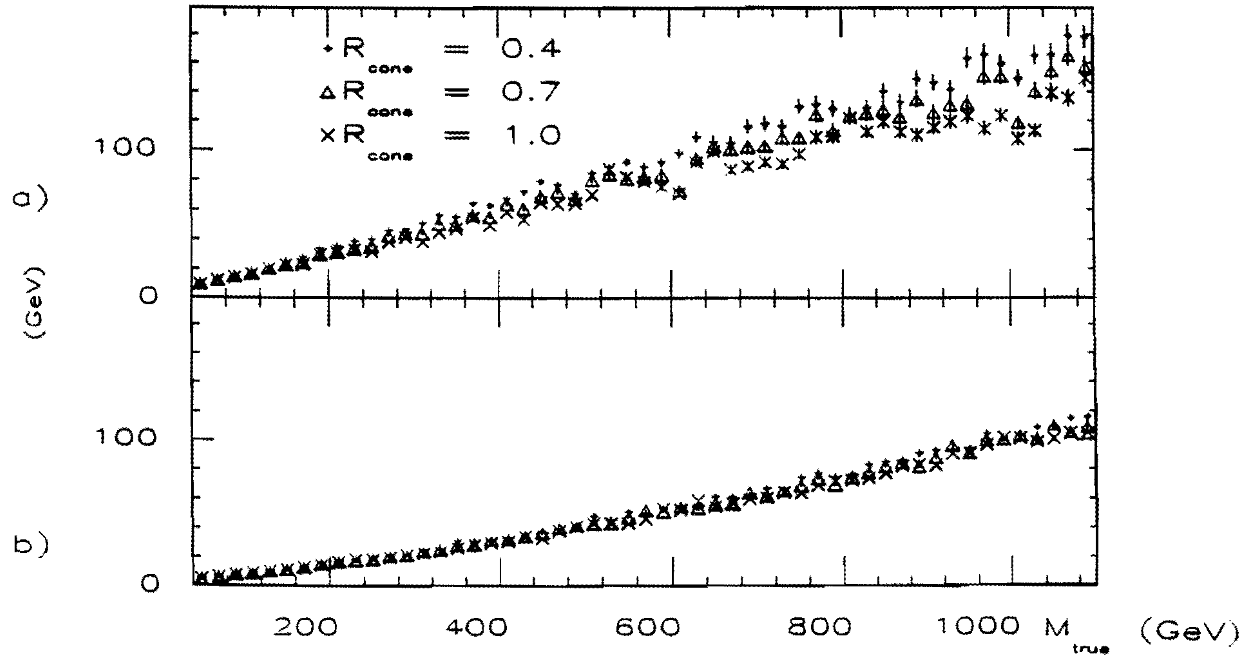

Figure 4.9: $\sigma(M_{jj} - M_{true})$ vs. $M_{true}$ for a) the "partons" true mass and b) the "particles" true mass.

## 4.4 Gluon radiation in the measurement of $\frac{d\sigma}{dM_{jj}}$

### 4.4.1 Dependence on the cone size

We investigated the dependence of the measured dijet mass spectrum on the choice of the cone size and how well the shower Montecarlos Isajet and Herwig reproduce the effect. To this purpose we analyzed the data and the simulation samples with the same programs. Single jet energies were corrected with the $\eta$-dependent corrections described in Ch. 3. The event selection described there was applied and, after normalization for the integrated luminosities, the spectra were obtained both for data and simulations by joining together the different samples. Fig. 4.10 shows the observed differential cross section $d\sigma/dM_{jj}$ for the three data samples JET_20, JET_40, JET_60[1]. The figure also shows the cuts applied on each sample to get rid of the trigger bias regions joining the curves together.

In fig. 4.11a) the bin-by-bin ratio of the cross sections obtained with different cone sizes, namely $R_{cone} = 1$ and $R_{cone} = 0.7$,

$$\frac{d\sigma(Rcone = 1.0)}{dM_{jj}} / \frac{d\sigma(Rcone = 0.7)}{dM_{jj}}$$

is plotted as a function of the dijet invariant mass $M_{jj}$ for data and ISAJET samples. Still comparing Isajet and data fig. 4.11b) shows values of the ratio:

$$\frac{d\sigma(Rcone = 0.7)}{dM_{jj}} / \frac{d\sigma(Rcone = 0.4)}{dM_{jj}}$$

We see that the choice of the cone does not affect strongly the shape of the spectrum, since the ratios are almost flat, and the values give an overall factor of $\sim 1.5$ in both cases. In fig. 4.12a) and b) the ratios of cross sections predicted by Herwig are compared to the data.

---

[1] The data set names refer to the trigger $P_t$ thresholds of 20, 40, 60 GeV (see section 2.1 of Chapter 3)

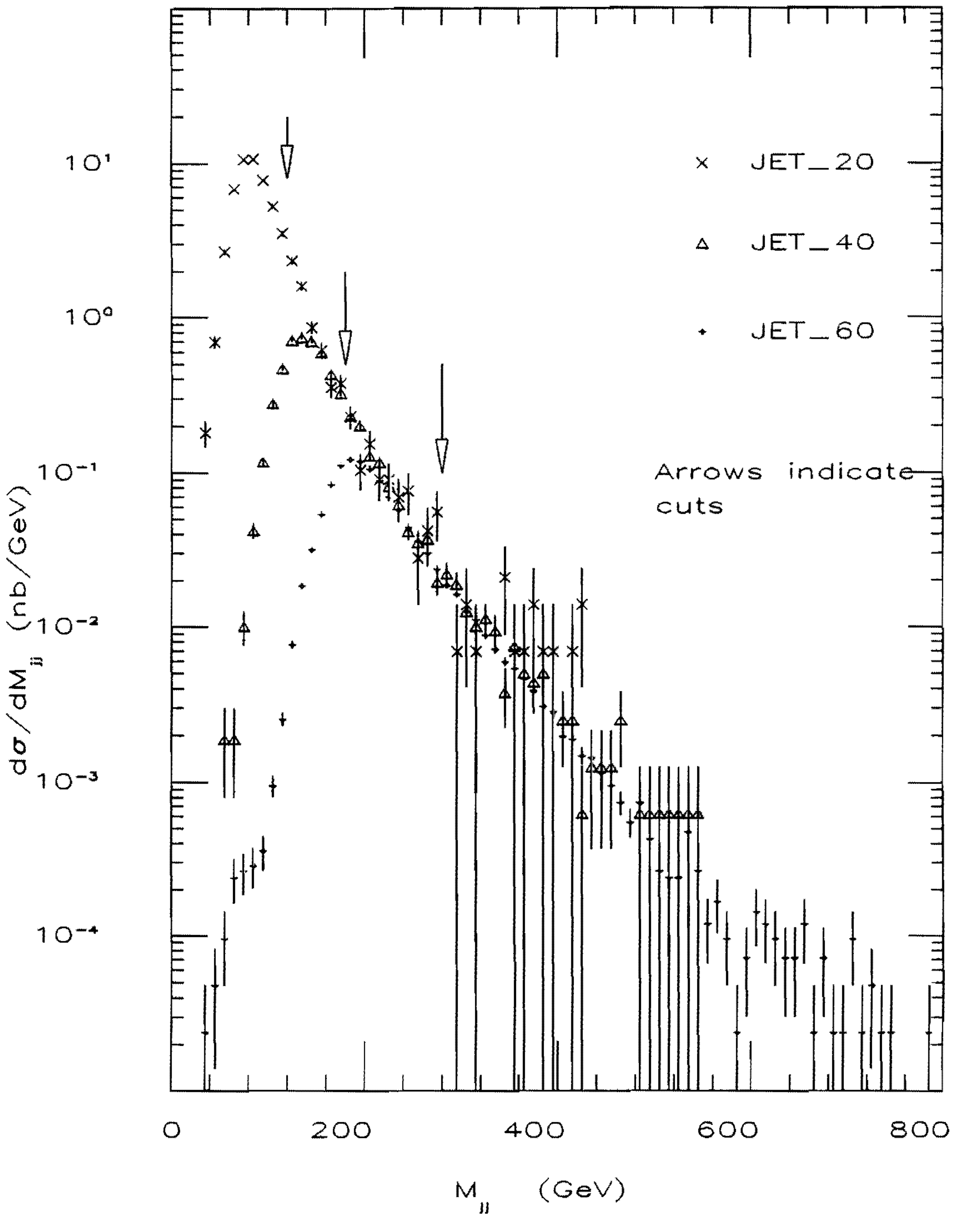

Figure 4.10: Dijet invariant mass spectra of the various subsamples.

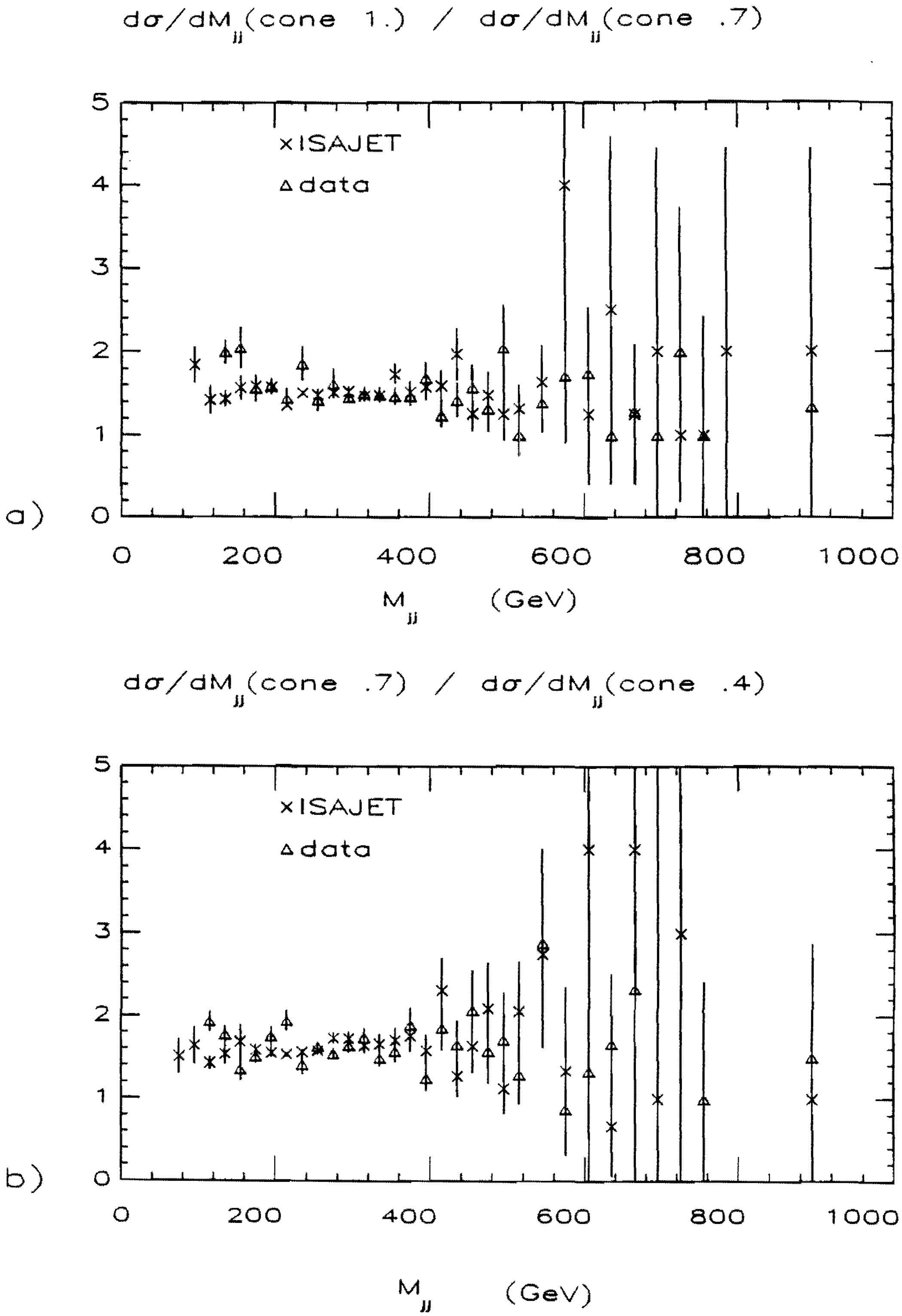

Figure 4.11: Comparison of the ratio of the measured dijet invariant mass spectra $\frac{d\sigma}{dM_{jj}}$ for a) Cone size 1.0 over 0.7 and b) Cone size 0.7 over 0.4 to Isajet predictions

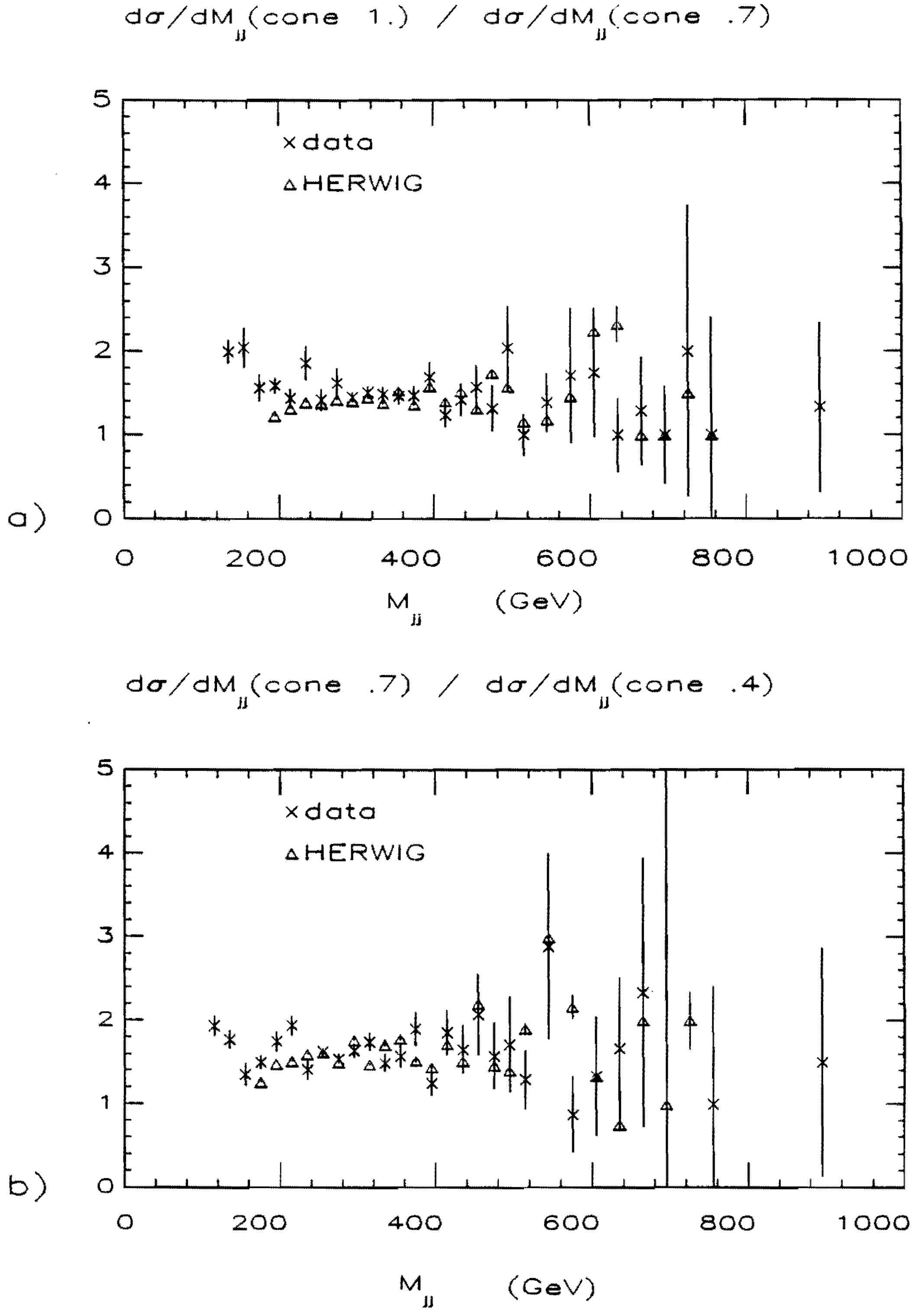

Figure 4.12: Comparison of the ratio of the measured dijet invariant mass spectra $\frac{d\sigma}{dM_{jj}}$ for a) Cone size 1.0 over 0.7 and b) Cone size 0.7 over 0.4 to Herwig predictions

In summary the most evident cone size effect on the dijet mass spectrum is an overall increase of the cross section for greater cones without a strong change of the spectrum shape. This is mainly due to an offset of the mass scale as shown in the previous section. Isajet and Herwig predictions agree within the errors with the experimental values, except perhaps at very low masses. The good agreement shows the good performance of both shower Montecarlos in predicting inclusive effects of the radiation.

### 4.4.2 Predictions compared to data on absolute scale

The study discussed in this section checks the ability of different theoretical predictions to reproduce on absolute scale the measured cross section as a function of the cone size used in the clustering algorithm. Data are compared to the shower Montecarlo predictions (Isajet and Herwig) and to the available parton level calculations, that is the Leading Order (LO) and Next-to-Leading Order (NLO) predictions.

While the shower Montecarlo cross sections are obtained through detector simulation and naturally include all the detector effects, the Parton Level predictions have been folded[2] to the $M_{jj}$ response function to obtain an observed cross section to be compared to the data [70]

For this study the event selection described in Ch.3 was used. The average cross section

$$< \frac{d\sigma}{dM_{jj}} >= \frac{1}{M_1 - M_2} \int_{M_1}^{M_2} \frac{d\sigma}{dM_{jj}} dM_{jj}$$

was calculated for $M_1 = 280GeV$ and $M_2 = 320GeV$ and it is plot in fig. 4.13 as a function of the clustering cone radius. Herwig and Isajet predictions are also

---

[2] If $f(x)$ is the Parton Level cross section as a function of the 'true' mass $x$, and the $M_{jj}$ response function $R(M_{jj}, x)$ gives the probability density function of measuring $M_{jj}$ from a 'true' mass $x$, we obtain the folded cross section $f'(M_{jj})$ as

$$f'(M_{jj}) = \int f(x) R(M_{jj}, x)\, dx$$

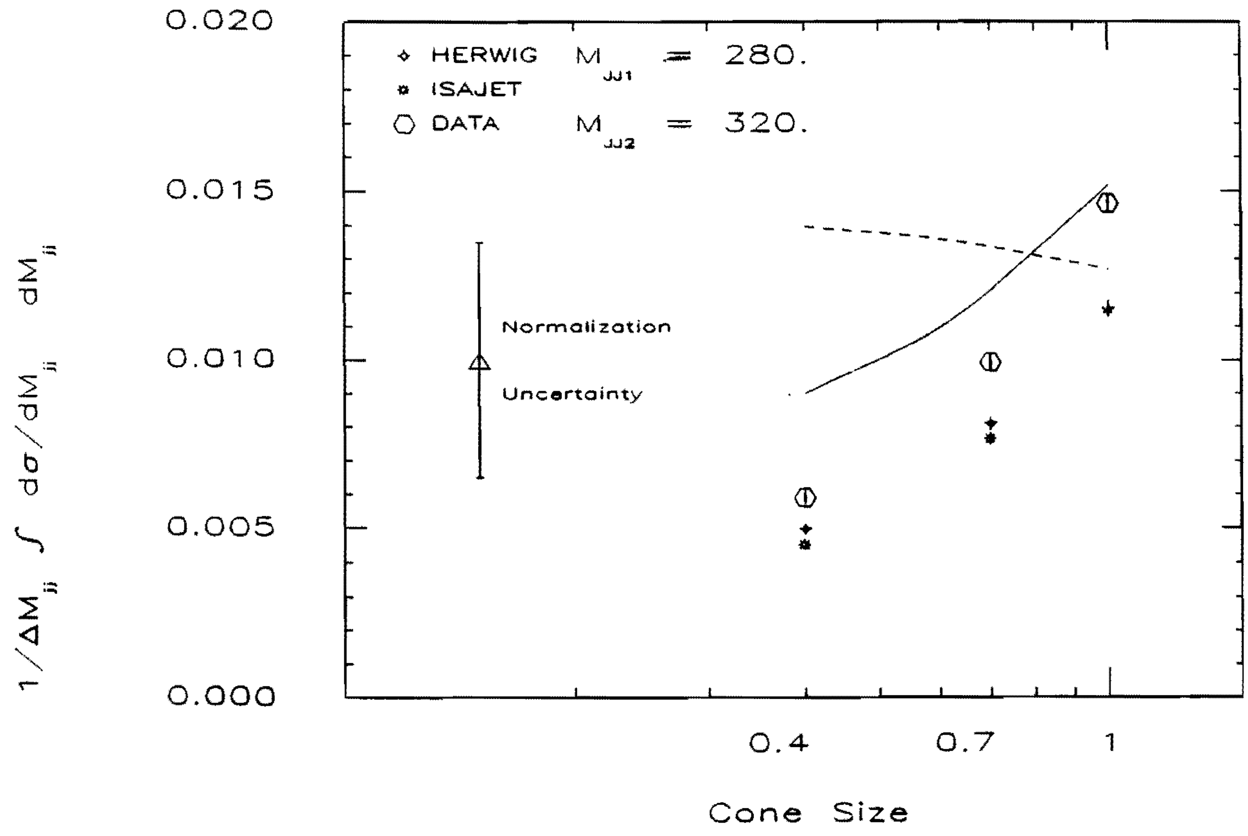

Figure 4.13: The dependence on cone size of the dijet invariant mass cross section at a given mass.

plotted. The dashed line is the QCD prediction (Born level), obtained with the structure function HMRSB [16] and $Q^2$ scale choice $Q^2 = P_t^2/4$ while the solid line corresponds to the NLO calculation [28] obtained with the same structure function and $Q^2$ scale. The error bars on the data points are statistical errors only, while on the left of the plot the error bar corresponding to the normalization uncertainty on the data is shown [69]. The normalization uncertainty on the LO predictions, estimated by varying the $Q^2$ by a factor of 4 and choosing different structure functions (namely DO, EHLQ, DFLM, MT [14,12,15,17]) is not shown but it is approximately of the same size of that of the data. The uncertainty is not yet available for NLO but it is expected to be smaller than that of the LO calculation.

Since the NLO predictions should in principle describe also the large $P_t$ branching, we released the $\Delta\phi_{back}$ selection cut (see Chapter 3 section 2.3) and compared again the data to the NLO and LO predictions in fig. 4.14.

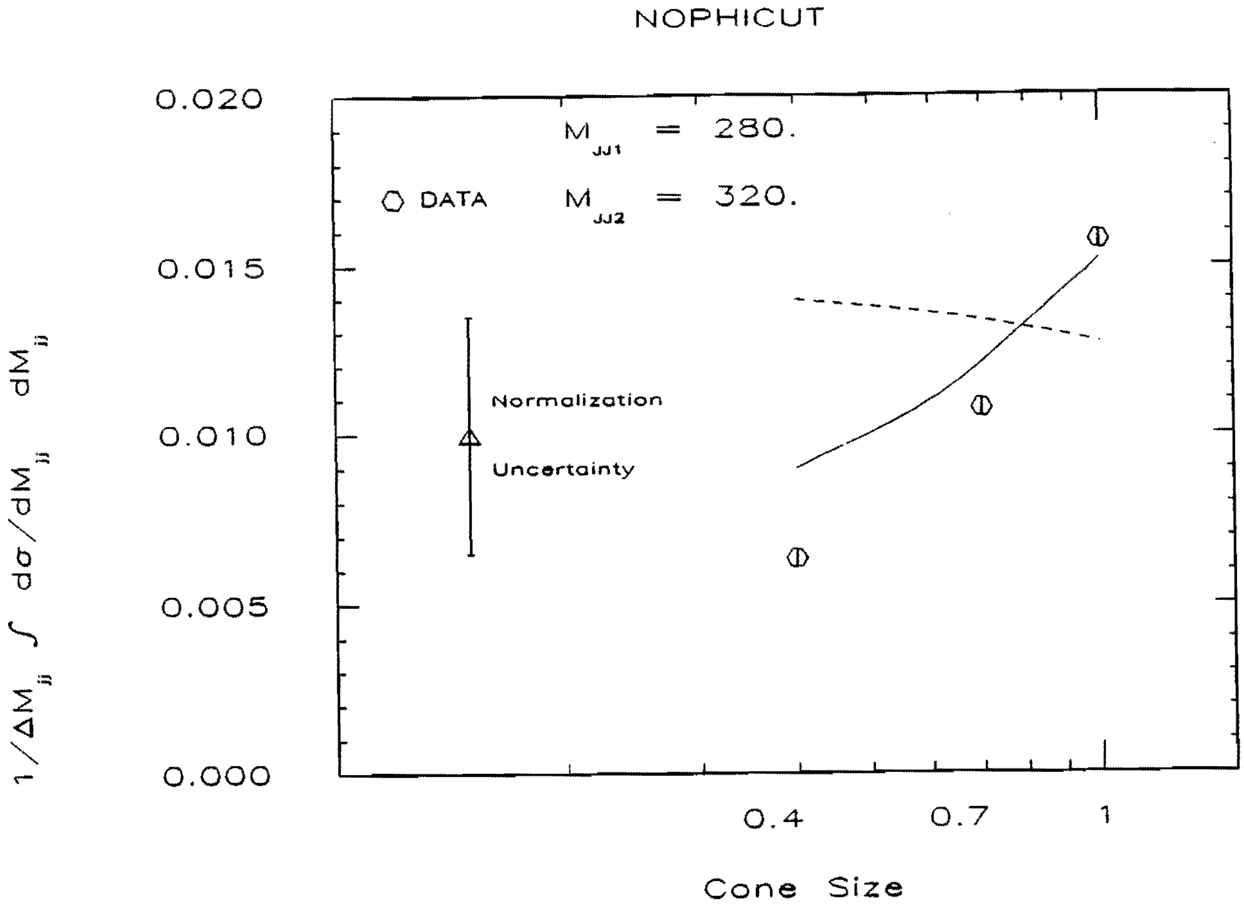

Figure 4.14: The dependence on cone size of the dijet invariant mass cross section: The $\Delta\phi_{back}$ cut on the data has been released.

The behaviour of the cross section as a function of the cone size is similar for data and both Montecarlo simulations. A steeper dependence is shown by data and simulation with respect to full QCD $\alpha_s^3$ prediction, but we should evaluate Structure Function and $Q^2$ dependence of the NLO calculation before coming to the conclusion that LLA gives a better description of the cone size dependence. From the figure the inadequacy of Born Level, which predicts no dependence on the cone size, is underlined (the weak dependence on the figure is due to the folding with the detector response).

## 4.5 Conclusions

Results of this chapter may be resumed in three points:

a) QCD *bremsstrahlung* radiation has important effects on the measurement of inclusive quantities (such as the dijet invariant mass); a completely efficient rejection of initial state radiation, and collection of final state radiation, cannot be obtained with a "smart" choice of $R_{cone}$.

b) Shower Montecarlos give substantially correct predictions on the inclusive effects of radiation. In predicting these effects ISAJET and HERWIG, although incorporating different features (see Ch. 5), give substantially equivalent results.

c) NLO calculations seem to be able to qualitatively reproduce the dependence of the data on the jet cone size.

# Chapter 5

# Interference effects in QCD radiation

We have seen in Chap. 4 that the Leading Log Approximation gives a satisfactory description of some radiation effects and that Isajet and Herwig are equally good in reproducing the measurements described there, although the two shower Monte-carlos are substantially different with respect to the interference between diagrams. We come to the conclusion that the above measurements are not sensitive to QCD interference. The goal of this chapter is to show that a more exclusive study of radiation can find variables sensitive to colour interference. Interference is detectable in the data, its effects being described by Herwig and not by Isajet.

## 5.1 Colour topology and interference in the QCD processes

When evaluating squared modules of matrix elements for a given subprocess one must keep in mind that two diagrams which do not differ in either the initial or the final state must be added coherently.

QCD is characterized by colour symmetry and colour currents must be strictly conserved. Colour must be taken into account in the description of the initial and final state of a QCD process when summing coherent diagrams.

An interference pattern should be observed when a process is described by two

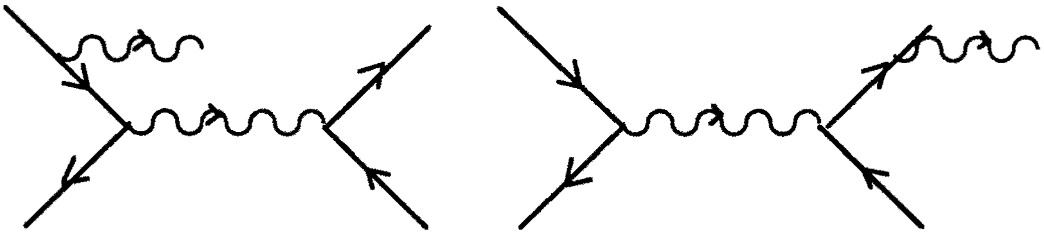

Figure 5.1: Emission of one gluon from initial and final state in a hard parton subprocess

(or more) diagrams to be added coherently. The case we are interested in is that of the bremsstrahlung emission of gluons from the incoming or outgoing parton lines in a 2 → 2 process. The elementary 2 → 2 process is experimentally observed as the emission of two hadronic jets (see Chap. 1). A large part of the gluons radiated from hard parton lines will contribute to the energy of the leading jets, but on occasion they may give rise to secondary (and generally softer) jets carrying away a fraction of the total energy in the CMF. The observation of three jet events is well established experimentally since jets may be defined and measured in a non-ambiguous way. We therefore expect to observe interference, for instance, when identical 2 → 2 processes are followed by gluon emission from initial or final state partons (Fig. 5.1).

For the sake of simplicity we shall for now restrict ourselves to one-gluon emission, but the following discussion can be generalized to multiple gluon emission and gives qualitatively similar results [74].

Furthermore we will consider only initial-final state radiation interference since this is easier to detect, its most striking effect being to give higher probability to find third jets in certain phase space regions with respect to others.

We can say where we expect to find a third jet but, because of interference, we cannot say if the third jet comes from initial or final state bremsstrahlung; this

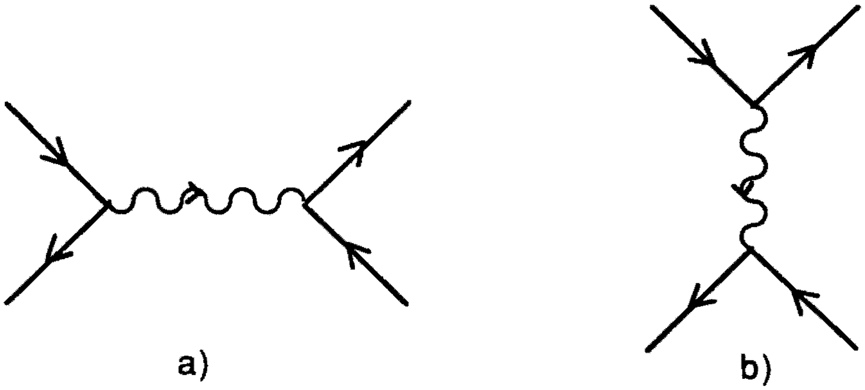

Figure 5.2: Feynman diagrams for $\bar{q}q \rightarrow \bar{q}q$: a) s-channel, b) t-channel

question has no meaning, in the same way as there is no meaning in asking which of two slits in an opaque screen lightened by a light source the photon observed beyond the screen has passed through.

### 5.1.1 Coloured Feynman diagrams and interference

To identify the interfering diagrams we must consider the possible colour configurations for each hard subprocess with one emitted gluon in either the initial or the final state. We can foresay that initial-final state interference will take place when a colour line can be traced back from the final to the initial state, i.e. when initial and final states are *colour connected* [74].

Let us first of all examine the $2 \rightarrow 2$ process $\bar{q}q \rightarrow \bar{q}q$ (identical flavours); in this case there are two channels (not keeping into account the colours): the s-channel and the t-channel. In fig. 5.2 the two Feynman diagrams for the $2 \rightarrow 2$ processes are shown. When considering gluon emission from the external legs, taking into account the colours we obtain the diagrams shown in fig. 5.3, where each numbered leg represents a colour state. The gluons are represented by couples of colour lines flowing in opposite directions.

It is easy to see that while the diagrams for the s-channel have the same colour

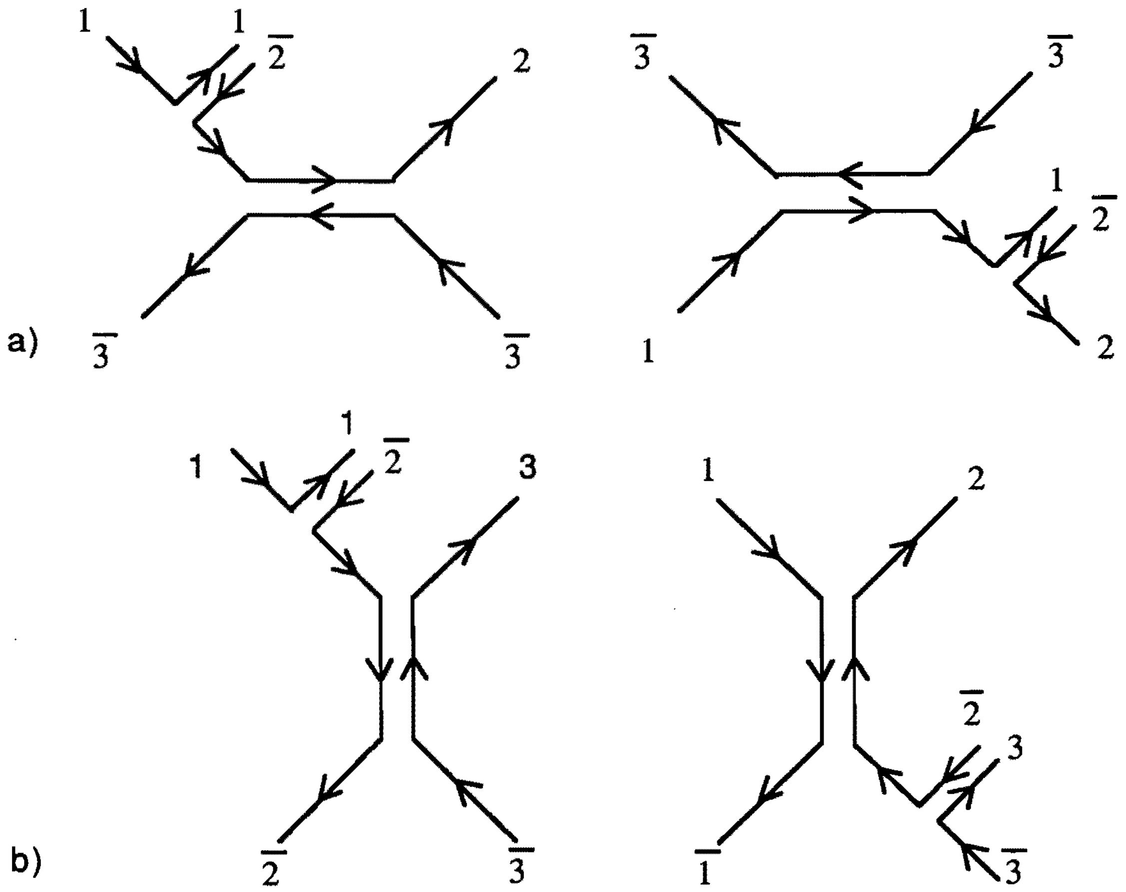

Figure 5.3: Colour configurations for $\bar{q}q \rightarrow \bar{q}q$: a) in the s-channel and b) in the t-channel

configurations in the final state (a $1-\bar{2}$ gluon, a 2 quark and a $\bar{3}$ antiquark), the diagrams for the t-channel have different configurations (a $1-\bar{2}$ gluon, a 3 quark and a $\bar{3}$ antiquark for the first; a $3-\bar{2}$ gluon, a 2 quark and a $\bar{3}$ antiquark in the second). With the assumption that each line carries its own colour, different from those of all other colour lines (this assumption corresponds to the approximation of an infinite number of colours, used by the shower Montecarlo Herwig [73]), there is no colour configuration which gives rise to interference between the two t-channel diagrams.

For the $2 \rightarrow 2$ process $\bar{q}'q \rightarrow \bar{q}'q$ (different flavours) flavour conservation at the strong vertices discards the s-channel, and therefore one finds exactly the same situation as in the case of $\bar{q}q \rightarrow \bar{q}q$ in the t-channel, where interference between the two colour diagrams cannot take place.

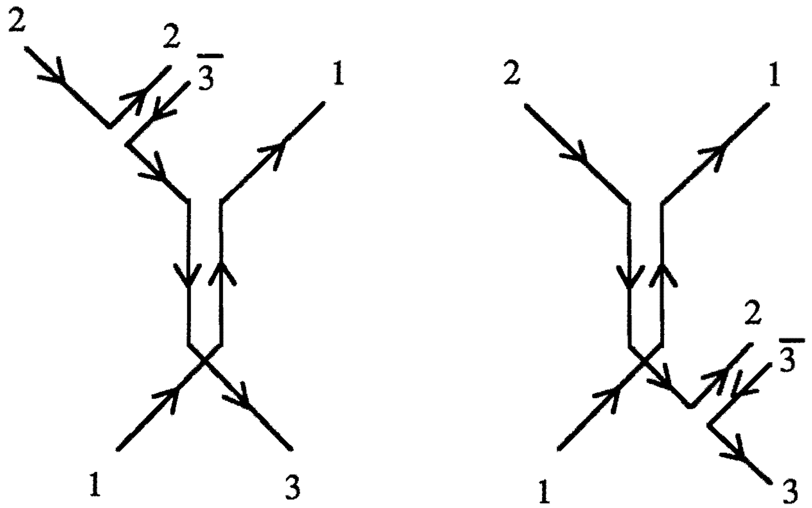

Figure 5.4: Colour configurations for $qq \to qqg$ in the u-channel

The process $qq \to qq$ has both the u and t-channel but they are fully equivalent, differing only for the labelling of the final state quarks. Fig. 5.4 shows the colour configurations when the gluon is emitted in a) initial and b) final state in the u-channel. As it is easy to see the colour configurations of the initial and final partons may indeed be identical, so that an interference is to take place.

It is quite natural, at this point, to conclude that if no colour line can be traced back from the final to the initial state in the $2 \to 2$ process colour diagrams, then the colour diagrams for emission of one bremsstrahlung gluon obtained from each will sum up incoherently, while if there is at least one such colour line tracing back a colour from the final to the initial state, then some diagrams must be summed coherently [74].

With this in mind we conclude that interference is present for all the remaining diagrams involving gluons in the $2 \to 2$ base process (see the examples in fig. 5.5).

### 5.1.2 The interference pattern: angular distribution of bremsstrahlung gluons. Herwig and Isajet

As a first step towards the detection of observable effects of QCD interference we should understand the predicted effects of such interference at the level of the the-

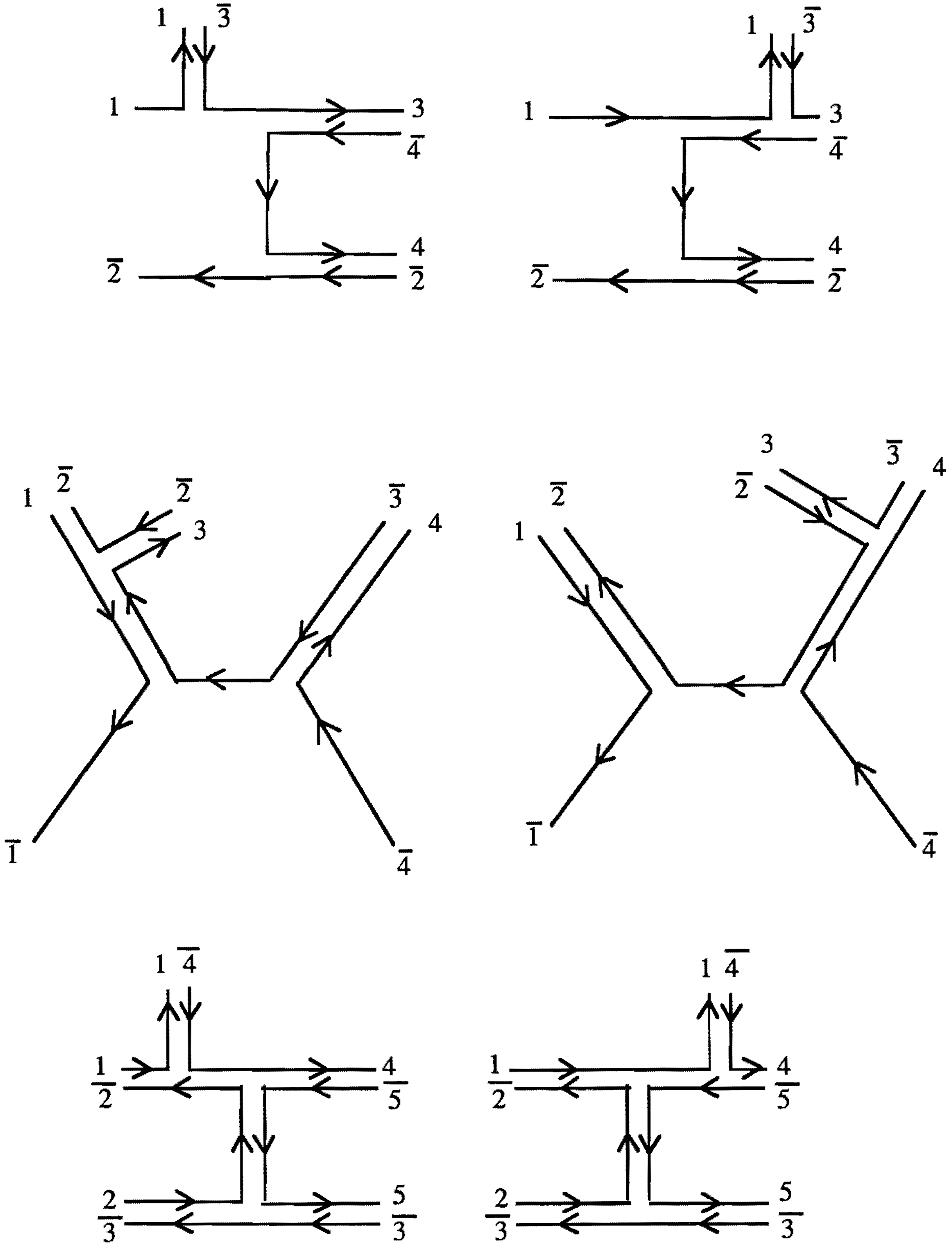

Figure 5.5: Some colour configurations for $\bar{q}q \to ggg$ , $qg \to qgg$ and $gg \to ggg$ respectively. The couples of diagrams are coloured so as to obtain identical initial and final colour state, i.e. interference

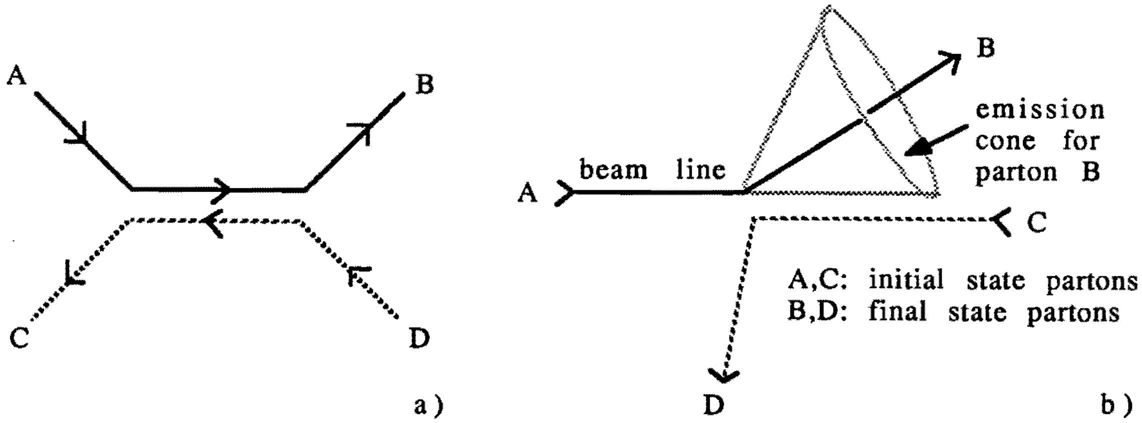

Figure 5.6: Definition of the emission cone for bremsstrahlung gluons from one hard parton: a) hard process, b) drawing of the emission cone

ory [81,82]. An exhaustive treatment of the theory is nonetheless out of the scope of this work. We shall therefore limit ourselves to a qualitative exposition of some results in the LLA. The shower evolution as a Markov process [75], is apparently inconsistent with the quantum properties of the theory (i.e. with the interference effects). This problem was solved in the LLA [76] showing that the effect of the interferences can be described at the leading log level by imposing proper phase space constraints to the evolution of the shower [76,77].

If we consider the emission of one soft gluon by one hard parton a cone may be defined, outside which a fully destructive interference results in a suppression of the emission [76,77]. Fig. 5.6 shows how the cone is defined. The left picture represents an example of a 2 → 2 Feynman diagram that can produce the event sketched on the right. Partons A and B are connected by the same colour line (colour connected) and so are partons C and D. The radiation emitted by parton B is constrained within the cone with axis on the direction of the emitting parton B and bounded by the direction of the colour connected parton A. Similar cones can be drawn for the emission of partons A, C, D.

The situation reminds the classical radiation of a relativistic electron. If the line

A-B is the trajectory of the accelerated particle, most radiation is confined in the region between the initial and the final electron directions.

In the shower Montecarlos incorporating this effect the emission cone is defined by the appropriate colour line in each branch of the shower.

As an example we shall examine the spatial distribution of radiation for the hard $2 \rightarrow 2$ scattering in fig. 5.7. The radiation is distributed in the whole space, but for sake of simplicity the figure shows only the cross section on the plane containing the four partons. The colour connected partons are A-B and C-D. The emission cones for the colour line C-D are not shown, assuming that we will be able to tag the final state parton which gives the major contribution to the final state radiation (namely by selecting the second jet, whose lower $E_t$ is correlated to the radiation losses, as shown in section 5.2.5). The emission cones overlap each other generating regions with depleted or enhanced radiation density (numbered from 0 to 2 in the figure).

One possibility to look for the enhancement/depletion in the data is to study the spatial distribution of the third jet, since the radiation, if energetic enough, will in general be clustered by the analysis algorithm into secondary jets. In this scheme the final state emitting parton (B in fig. 5.7) is associated with the second jet and it is natural to measure the spatial distribution of the third jet around the second one using the variables $\Delta\eta = \eta_3 - \eta_2$ (distance in pseudorapidity) and $\Delta\phi = \phi_3 - \phi_2$ (distance in azimuthal angle). From examples like that in fig. 5.7 one would expect that colour coherence between initial and final state hard-partons will enhance the emission of the third jet in the half-plane defined by the second jet and the beam axis ($\Delta\phi = 0$) and in the convex region between the second jet and the beam axis ($\Delta\eta > 0$).

The way Isajet deals with the emission of radiation from the parton legs of each hard subprocess is completely uncorrelated: it is obvious that no interference pattern can be simulated in this kind of approach [78].

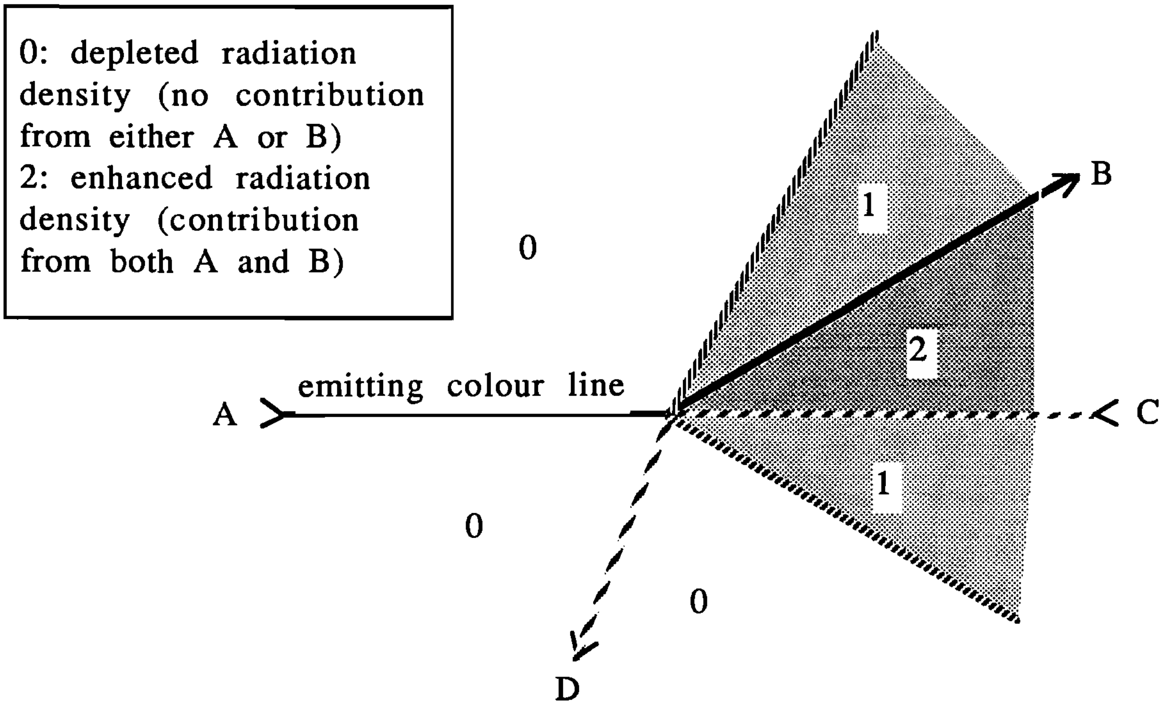

Figure 5.7: Cross section on the four partons plane of the spatial distribution of radiation for the hard scattering of fig. 5.6. Notation for the various zones is explained in the inset

Herwig instead takes into account interference between various colour diagrams by means of the phase-space constraints to the evolution of the shower [73].

A comparison between the spatial distributions of the third jet around the second jet predicted by Isajet and Herwig will exhibit the effect of the colour interference to be searched in the data. We will see in the next section that:

i) the data show an effect compatible with interference;

ii) a shower evolution that does not implement the phase space reduction, does not reproduce the effect

iii) LLA implementation of coherence predicts the effect properly.

## 5.2 A study of radiation by means of the third jet

### 5.2.1 Kinematic variables for the description

As formerly stated in sect. 2.3 of Chap. 3 the jets are numbered with decreasing transverse energy. A proper set of kinematic variables for our description of events with at least three-jets is formed by the pseudorapidities $\eta_1$, $\eta_2$ and $\eta_3$ of the first three jets, the azimuth angles $\phi_1$, $\phi_2$ and $\phi_3$, and the jet transverse energies $E_{t1}$, $E_{t2}$, $E_{t3}$.

### 5.2.2 Data sample and selection cuts

The data sample and the basic selection cuts are reported in sect. 2.1 and 2.3 respectively of Chap. 3, we will describe here only the additional features and requests specific to the present analysis.

The JET_60 subsample, which is not trigger-prescaled, is the most populated and we will from now on restrict our study to this subsample.

In sect. 1.1 of Chap. 3 we have discussed the clustering algorithm which gives us the experimental definition of jet. There we mentioned the fact that $R_{cone}$ is the main knob to make the algorithm more or less "inclusive" to the radiation. For this reason we commit ourselves to check further the dependence of our measurement from this parameter. For now we make the choice $R_{cone} = 0.7$.

By comparison of $E_{t1}$ distributions for JET_40 and JET_60, after application of the basic selection cuts, we obtained the value of $E_{t1} = 110 GeV$ at which the two spectra start to overlap. This was taken as the fiducial value for the $E_{t1}$ cut for the JET_60 sample, to avoid regions biased by the trigger threshold. In fig. 5.8 the distributions are shown, normalized for integral luminosity and prescale factors, and the position of the cut is indicated.

We then required the presence of a third jet. Due to the clustering algorithm

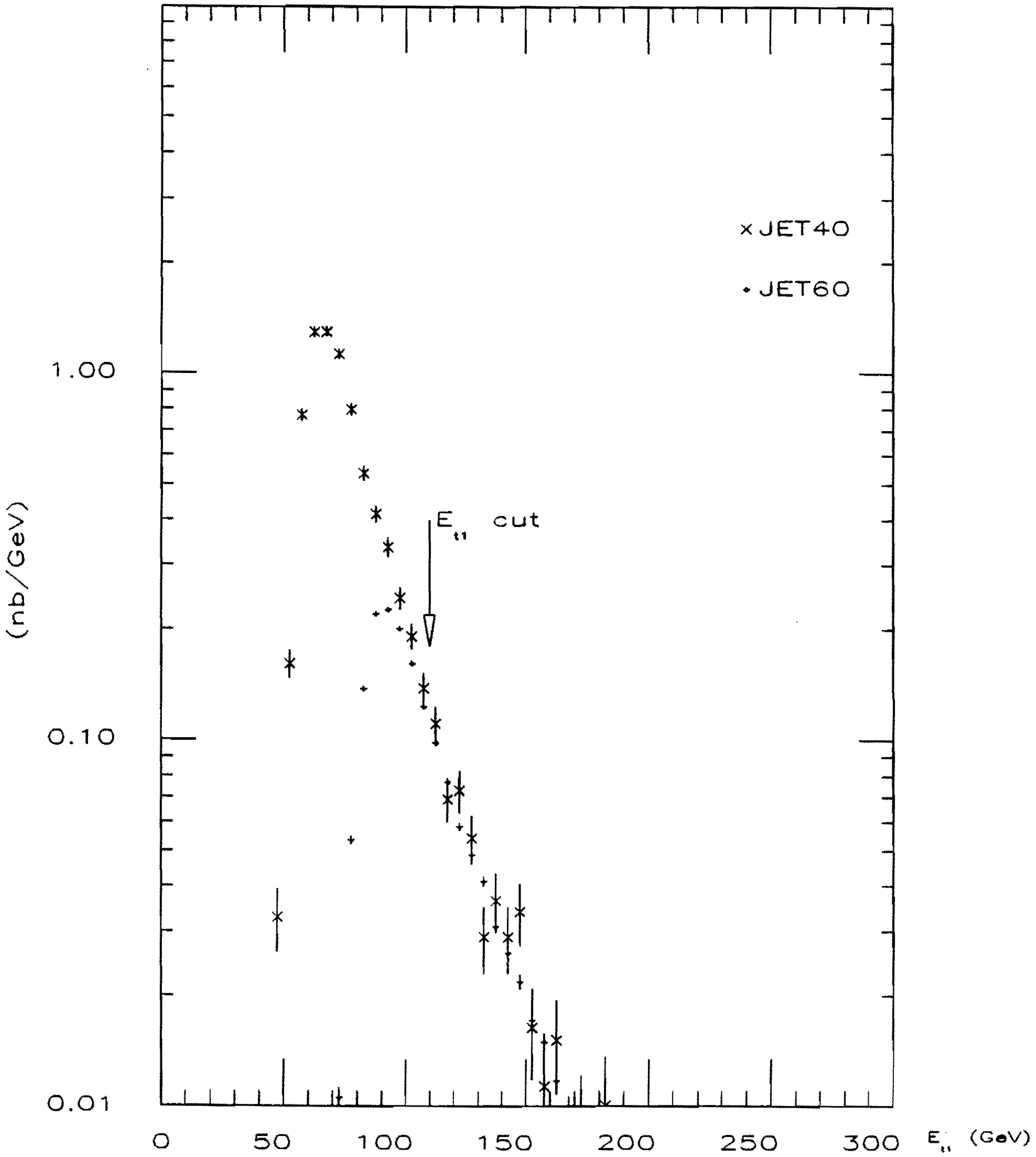

Fig. 5.8 — $E_{t1}$ distributions for JET_40 and JET_60

this is a further request for a calorimetric cluster falling outside the merging regions of the two leading clusters.

We now turn to energy distributions of third jets. In the scatter plot of fig. 5.9a) dots refer to events having a third jet with a given rapidity (horizontal axis) and a given energy (vertical axis). In the scatter plot of fig. 5.9b) the vertical axis reports instead the values of transverse energy of the third jet. In these scatter plots we see the effect of the clustering algorithm efficiency, which has a threshold at low $E_{t3}$. Going towards the forward region this becomes a higher and higher threshold in $E_3$ which cuts the $E_3$ distribution along a line corresponding to $E_{tcut}/\sin\theta$. We want to cut the region biased by the clustering efficiency. A safe method is to cut on $E_{t3}$. We choose the value of 10 GeV for this cut, which eliminates the switch-on region of the $E_{t3}$ distribution shown in fig. 5.10.

In fig. 5.9 is visible an inefficiency around the pseudorapidity 2.3. This is an effect of the $\eta$ cracks described in sect. 1.3 of Chap. 3. Fig. 5.12 in the next section shows that the simulation is not really good in reproducing this inefficiency. This disagreement between data and Montecarlo is under study to provide a corrected gas calorimeter simulation. The number of events left after all the cuts and the request of a third jet was of 10650 for JET_60.

### 5.2.3 Simulated samples

We used the samples described in sect. 2.4 of Chap. 3. Dealing with third jets, we are now exploring the borderline where the shower Montecarlos can show their limits. Since our study is based on the different approximations used by Isajet and Herwig to generate bremsstrahlung radiation, we need to gain as much insight as possible in the performances of the two programs in simulating the characteristics of the third jet. We do not expect the detection of interference effect to be particularly sensitive to the degree of agreement between the simulated and the real internal structure of the third jet, but we require an overall consistency for the global variables that

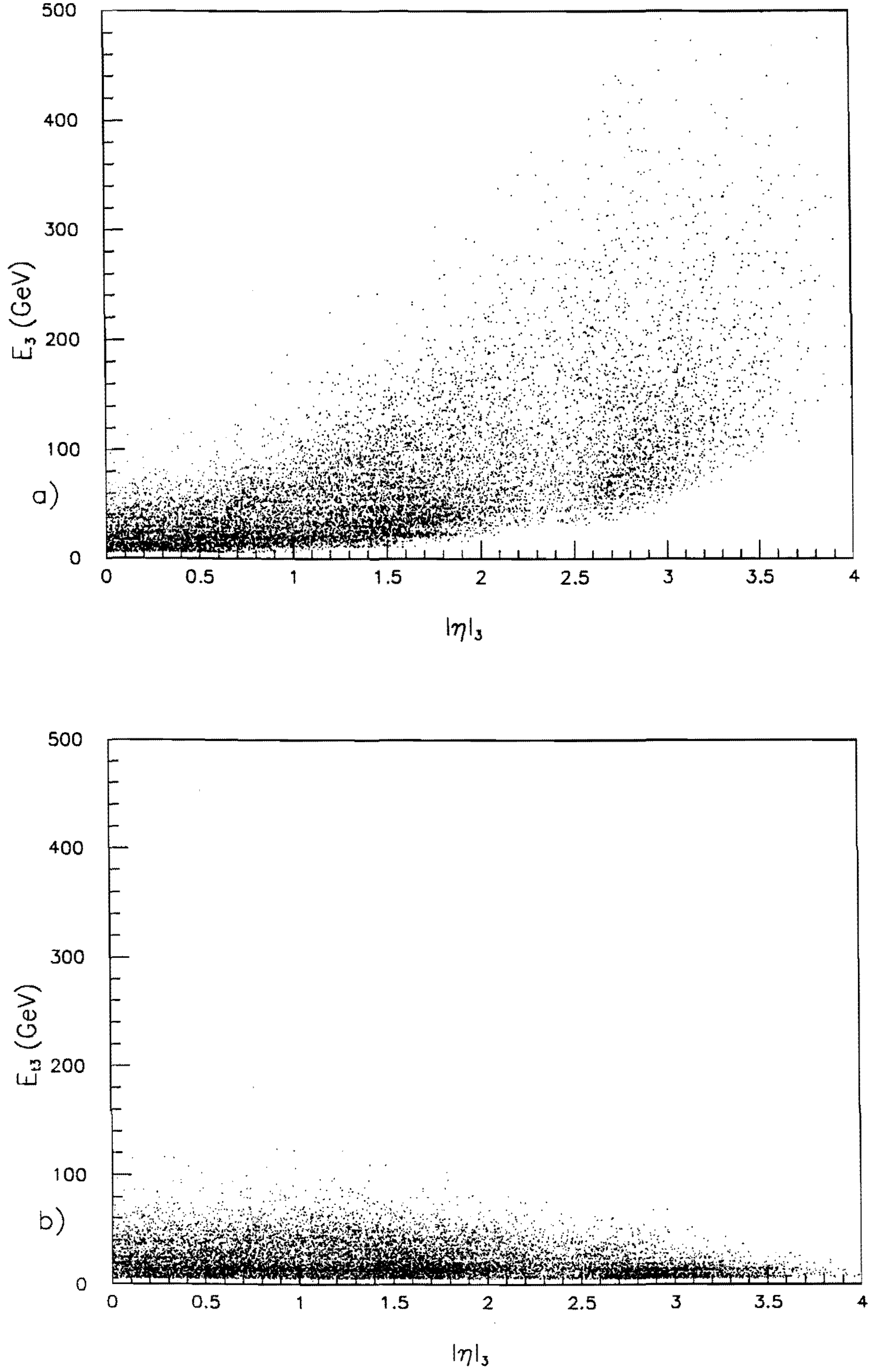

Fig. 5.9 – Scatter plots a)$E_3$ vs. $|\eta|_3$ and b)$E_{t3}$ vs. $|\eta|_3$

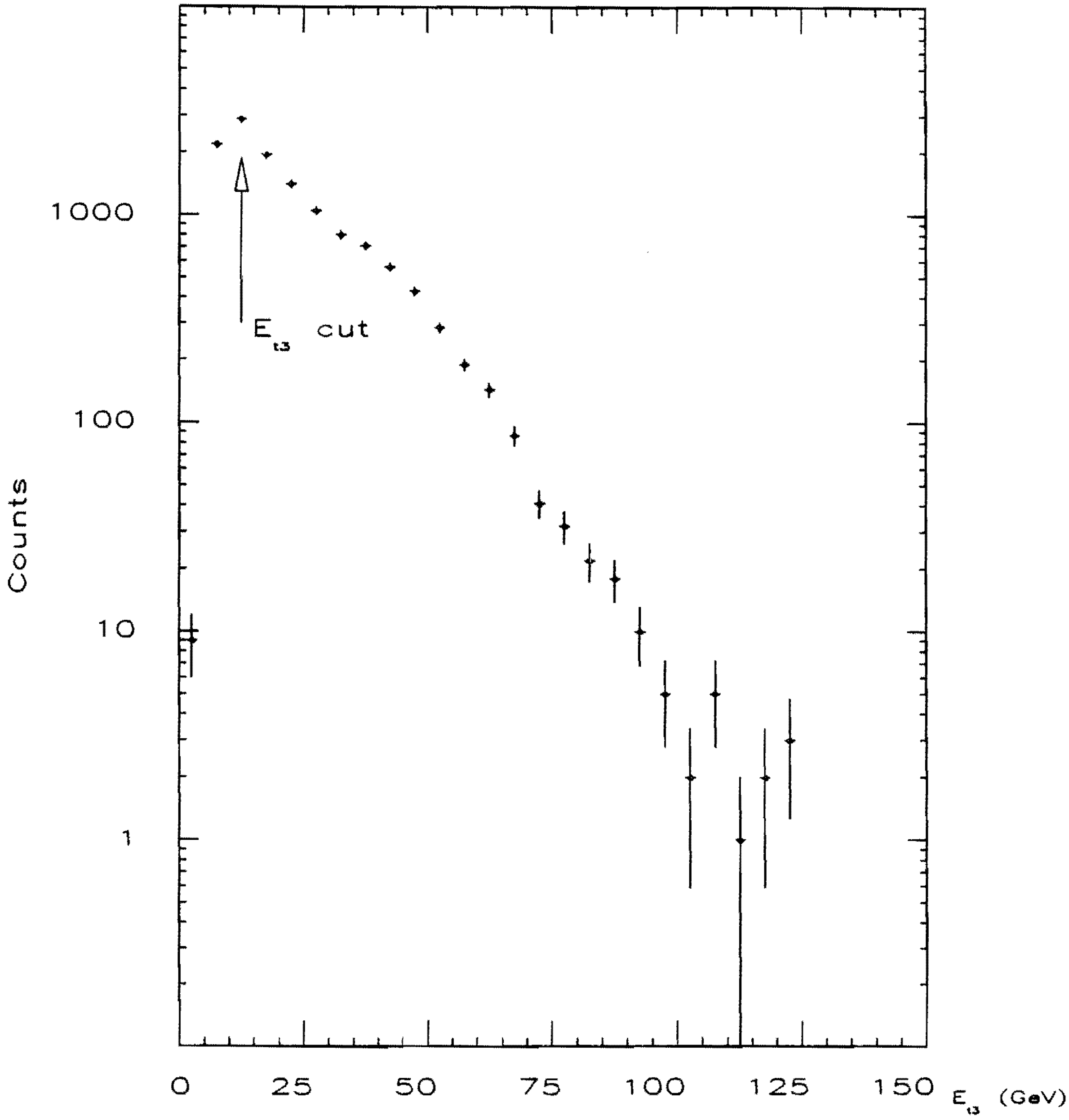

Fig. 5.10 — $E_{t3}$ distribution

| | **Herwig sample** | **Isajet sample** |
|---|---|---|
| *Total integranted luminosity* $(pb^{-1})$ | 5.5 | 5.9 |
| *Total number of events* | 280000 | 280000 |
| *Events passing main cuts* | 62742 | 59334 |
| *Of which with third jet* | 54629 | 54285 |
| *Passing* $E_{t1}$ *cut* | 13782 | 14735 |
| *Passing* $E_{t3}$ *cut* | 11004 | 12261 |

Table 5.1: Summary of simulated sample populations

describe the role of the third jet in the event.

We applied the same cuts used for the data to the simulated samples (these include the request of a third jet). The populations before and after application of each cut are summarized in tab. 5.1.

Distributions of the main physical quantities characterizing the third jet were then compared for each sample to those obtained from data. These included:

- Energy $E_3$
- Transverse energy $E_{t3}$
- Pseudorapidity $\eta_3$
- Detector pseudorapidity $\eta_{det3}$

Fig. 5.11 shows the distributions of $E_{t3}$ for different values of $\eta_{det3}$, compared to the corresponding simulation plots. Experimental distributions of third jet energies are more or less well reproduced by both the simulators.

In fig. 5.12 the pseudorapidity and the detector pseudorapidity distributions of the third jet are shown for Isajet, Herwig and data samples respectively. A good agreement is found for these quantities between Herwig and data, while Isajet has more problems in predicting the absolute spatial distribution of third jets and this is possibly influenced by failure in reproducing colour interference.

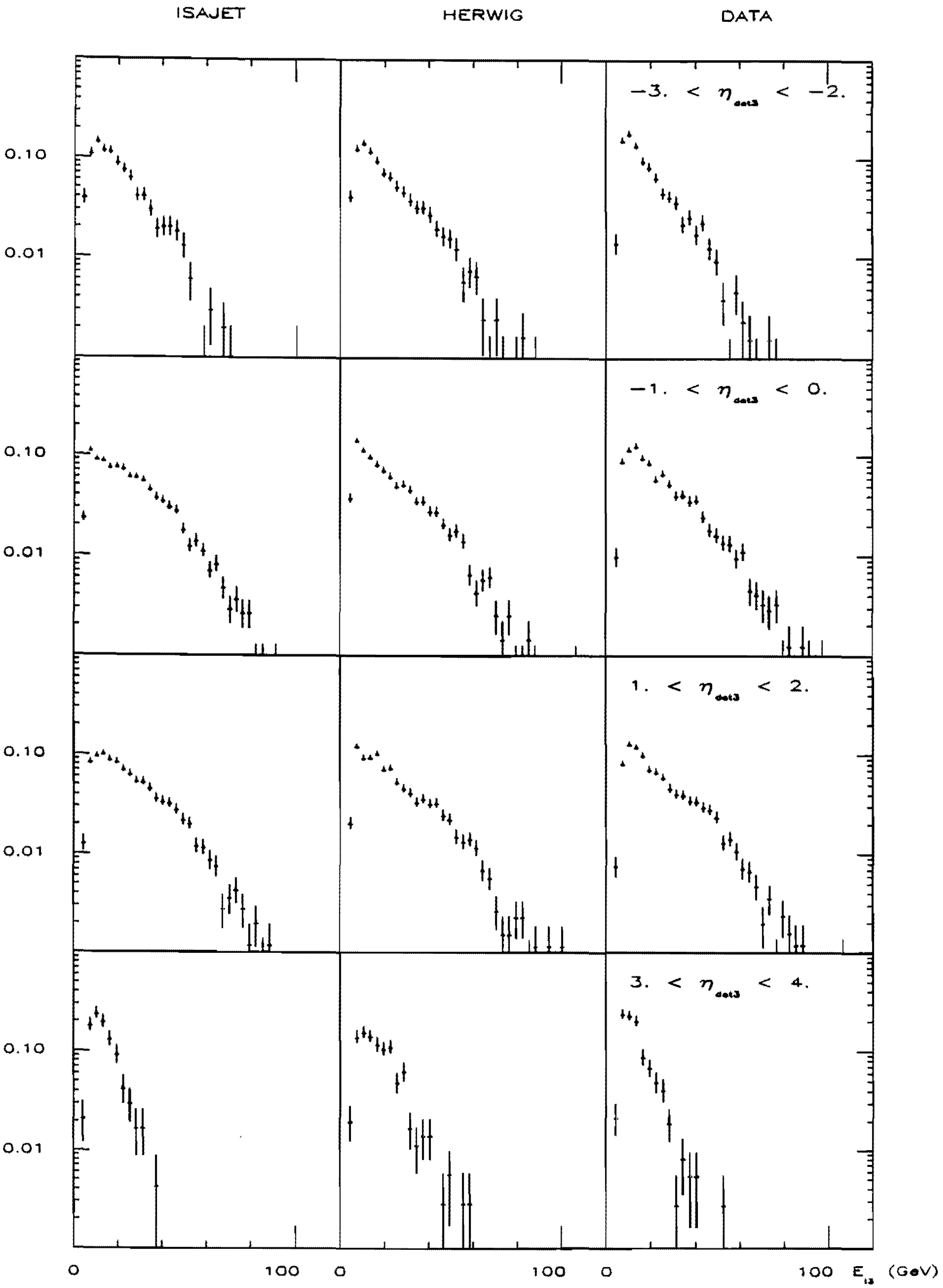

Fig. 5.11 — $E_{t3}$ distributions at various values of $\eta_{det3}$ for ISAJET, HERWIG and DATA respectively

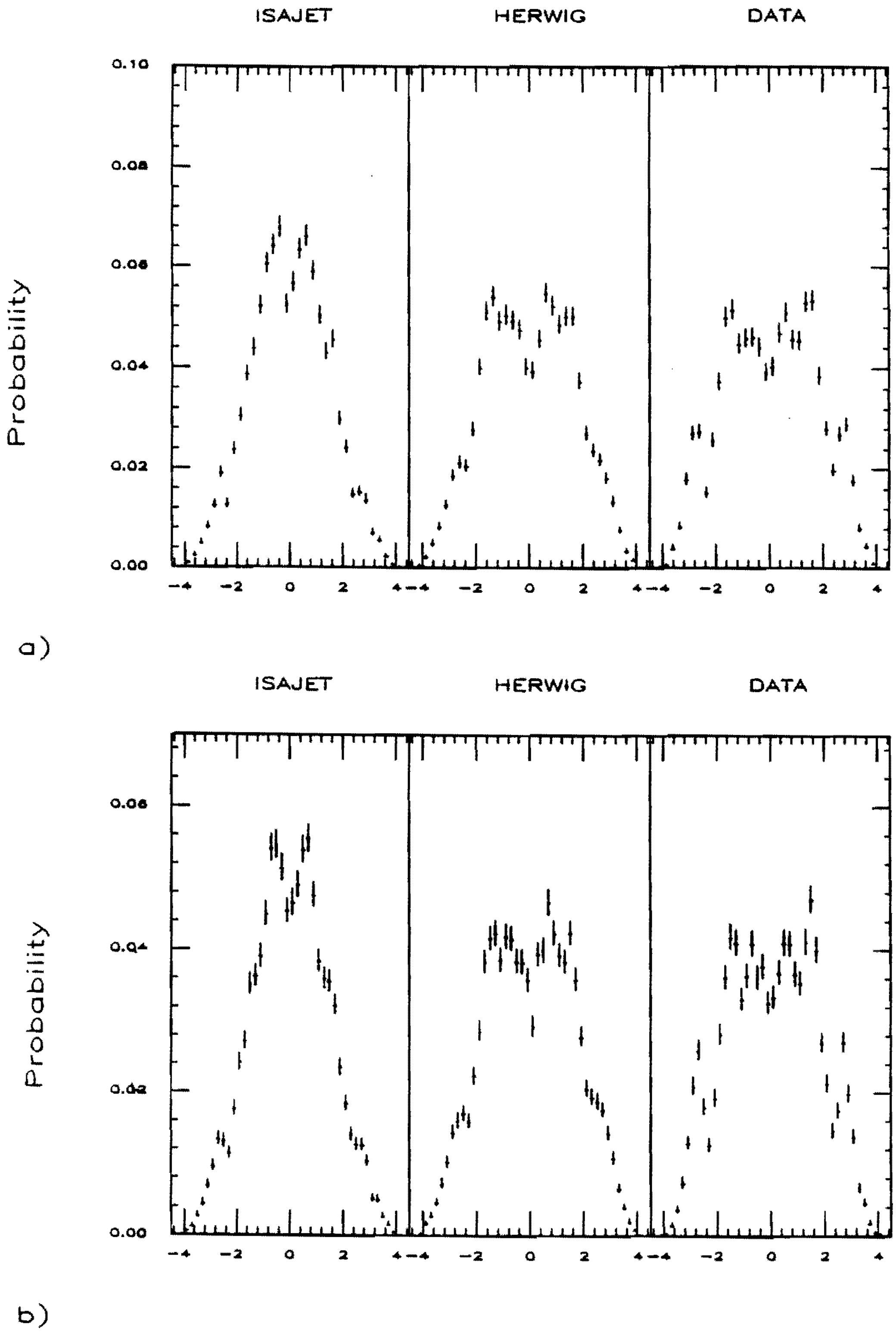

Fig. 5.12 — a) $\eta_3$ distributions. b) $\eta_{det3}$ distributions

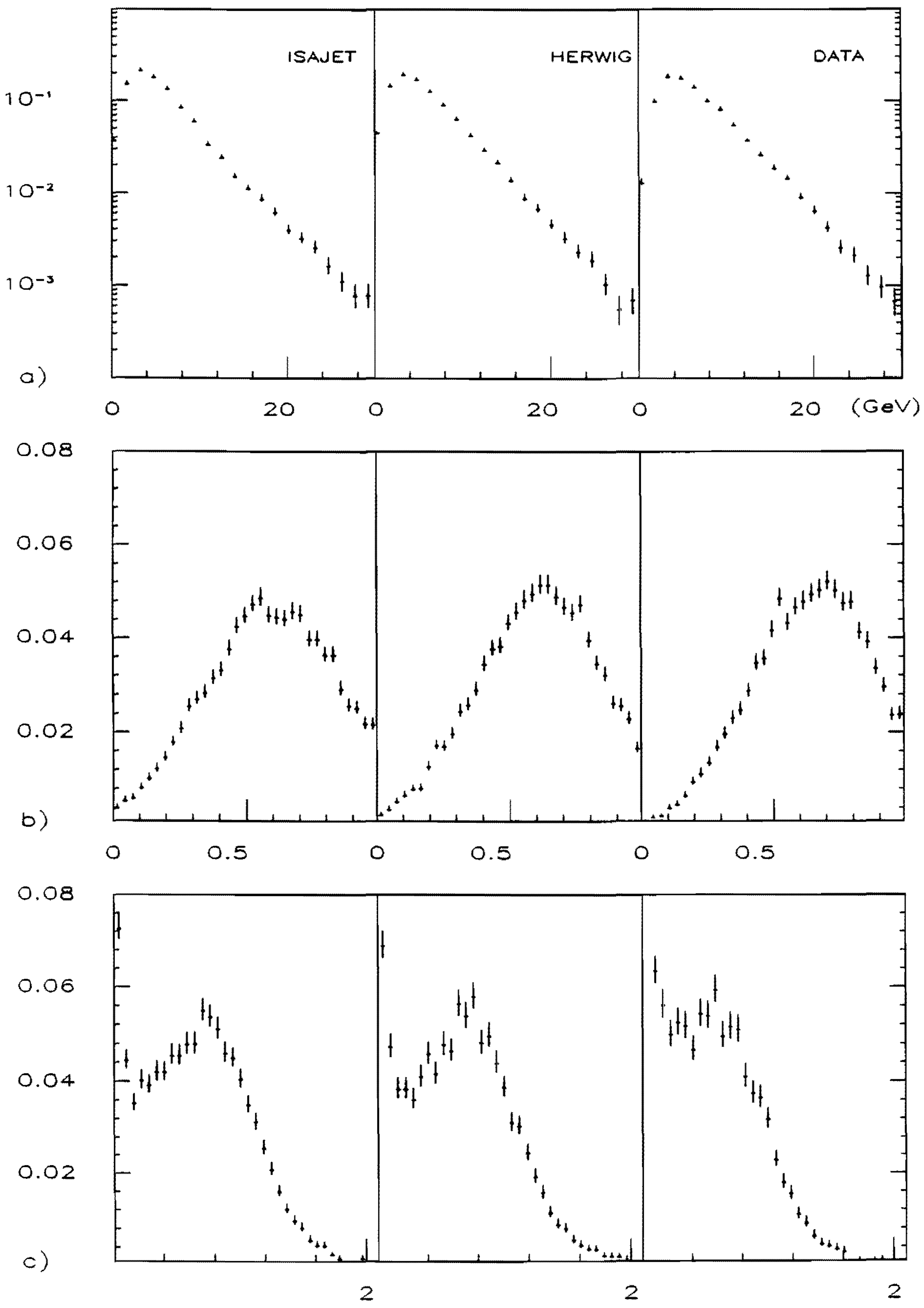

Fig 5.13 — a) Invariant mass $M_3$, b) EM fraction $EMF_3$ and c) Charged fraction $CHF_3$ distributions of 3rd jets for ISAJET, HERWIG and DATA respectively

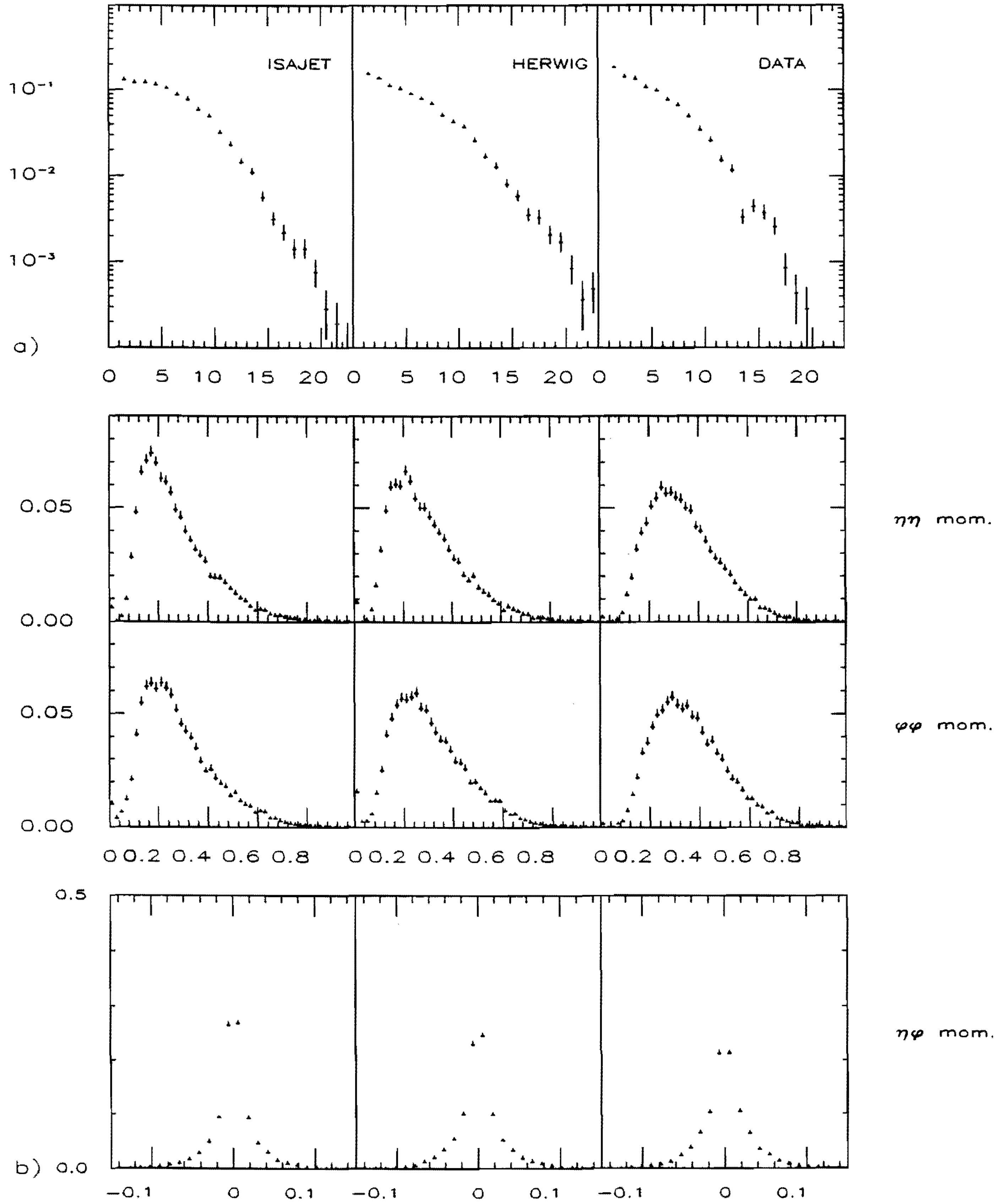

Fig 5.14 — a) Number of charged tracks $NTRK_3$ and b) Second moments distributions of 3rd jets for ISAJET, HERWIG and DATA respectively

In addition we compared experimental and simulated distributions for the following variables describing the internal structure of the third jet:

Invariant mass $M_3 = E_3^2 - |\vec{P}_3|^2$

Electromagnetic fraction $EMF_3$ and charged fraction $CHF_3$ [1]

Number of charged tracks $NTRK_3$[2]

Second moments[3] in the $\eta\phi$ plane

Figs. 5.13 and 5.14 summarize the results. For these quantities, strongly connected to fragmentation properties of the jet, a not perfect agreement is found between simulations and data. The disagreement seems small enough to give negligible consequences on the third jet spatial distribution. At any rate it is apparent that Isajet has more problems in predicting these characteristics than Herwig does. This hints that interference is important also for fragmentation properties, since fragmentation is strongly influenced by the shower development.

### 5.2.4 Angular distribution of the third jet around the second jet: the $R, \alpha$ space

As stated in sect. 5.1.2, to highlight the regions of radiation enhancement due to colour interference we study the spatial distribution of the third jet with respect to the second [79]. In the scatter plot of fig. 5.15a) the horizontal axis reports the azimuthal distance $(\phi_3 - \phi_2)$ . On the vertical axis the pseudorapidity distance $sign(\eta_2) \cdot (\eta_3 - \eta_2)$ is reported. Let's call these variables $\Phi$ and $H$ respectively. The range for $\Phi$ is $[-\pi, \pi]$ while $H$ ranges over the calorimeter acceptance.

With this choice for the sign, $H > 0$ means that the third jet direction is inside the convex cone defined by the second jet and the beam direction, while $H < 0$

---

[1] Both $EMF_J$ and $CHF_J$ are defined in Chap. 3 sect. 2.2

[2] Number of Charged tracks found pointing to the jet cluster

[3] Tower-$E_t$ weighted second moments in the $\eta - \phi$ space, giving a measure of the jet shape.

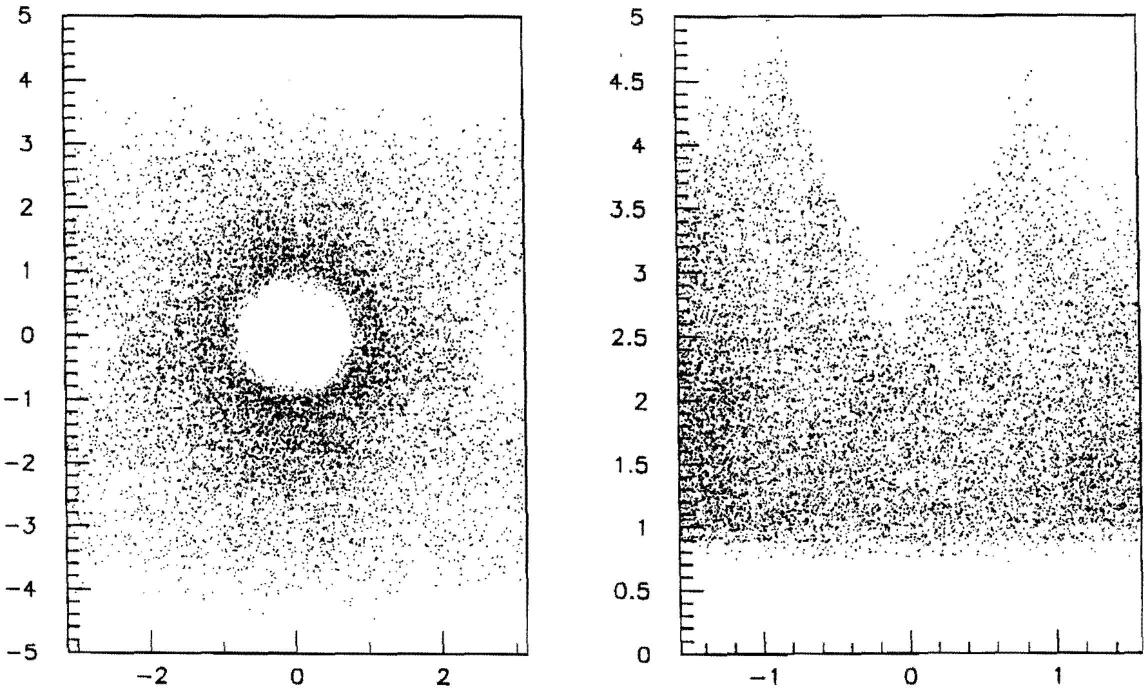

Fig. 5.15 – a)Scatter plot H–Φ of 3rd jet with respect to the 2nd. b)Scatter plot R–α of 3rd jet with respect to the 2nd

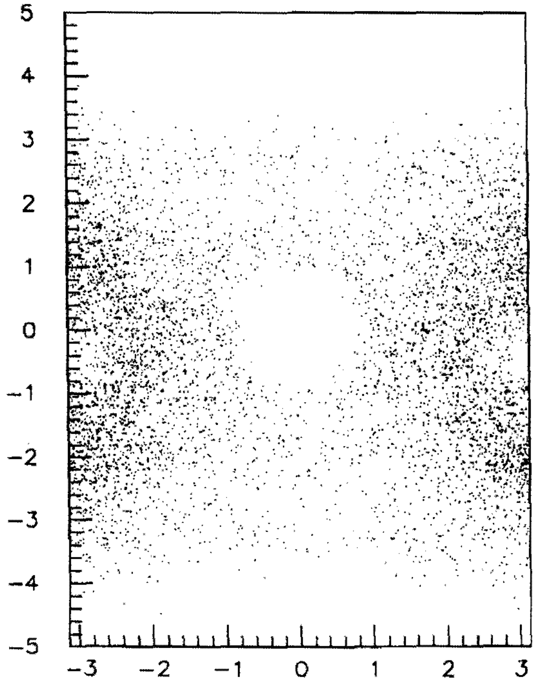

Fig. 5.16 – Scatter plot H–Φ of 3rd jet with respect to the 1st

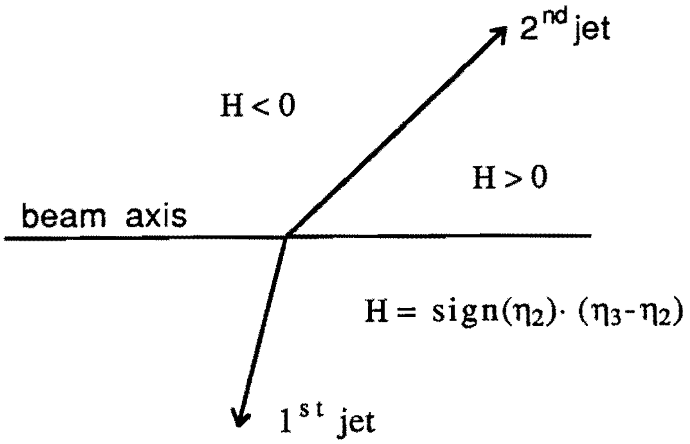

Figure 5.17: $H > 0$ marks the region of expected radiation enhancement (compare to fig. 5.7).

means the third jet direction falls outside of it, as shown in fig. 5.17. By comparison with fig. 5.7 we expect in this way to tag the regions of radiation enhancement.

In fig. 5.15a) the second jet position is at the origin, while the first jet is expected to be more or less back to back in $\phi$, that is near the edges $\Phi = \pm\pi$. As can be clearly seen from the scatter plot, a circular region (of radius $= R_{cone}$) in the $H, \Phi$ space around the second jet axis is forbidden to other jets by the clustering algorithm (see section 1.1 of Chap. 3). Therefore a set of "polar" variables turns out to be useful. We define $R = \sqrt{\Phi^2 + H^2}$ and $\alpha = \arctan(H/|\Phi|)$ as our variables of choice. Since we have complete mirror symmetry, the sign of the difference $\phi_3 - \phi_2$ would give no new information, while lowering the statistics by dispersing events over a larger interval. Choosing $|\Phi|$ in the definition of $\alpha$ corresponds to folding the scatter plot in fig. 5.15a) along the $\Phi = 0$ axis. The range for $R$ is $[0, \infty)$ (actually the upper limit is given by the calorimeter acceptance) while the range for $\alpha$ is $[-\pi/2, \pi/2]$. These variables give a one to one correspondance of the $H, |\Phi|$ plane, mapping the clustering cone boundary (the circle around the point $H = 0$, $\Phi = 0$ in fig. 5.15a) to a straight line in fig. 5.15b).

For completeness the scatter plot of fig. 5.16 shows the position of the third jet with respect to the first one. This time the first jet is at the origin of the scatter plot. Comparing fig. 5.15a) to fig. 5.16 it is clear that the third jet will most likely stay near the second one. This feature is in agreement with our hypotesis that the second jet is more correlated to the final state radiation than the first one. This will be further investigated in the next paragraph.

### 5.2.5 Study of $R$, the distance between the $3^{rd}$ jet and the $2^{nd}$ jet in the $\eta, \phi$ space

Fig. 5.18 shows the $R$ distribution (projection normalized to unit area of the scatter plot 5.15b) on its vertical axis) superimposed to the predictions from the Montecarlos. The overall behaviour of the data is reproduced by both simulations. Actually Isajet shows some bigger discrepancies, particularly for $R > 3$. The difference between Isajet and Herwig triggers our attention and suggests a possible effect of the colour interference. Unfortunately the two simulated distributions are qualitatively similar, and there is no striking difference between the two patterns. In addition the biggest effect is at large $R$ getting contribution from the forward/backward gas calorimeters, the most delicate to be simulated. For these reasons we discarded the possibility of searching colour interference in the small quantitative difference between the two simulated R distributions, looking for more suitable variables.

The analysis in the following sections rests on the hypothesis that we can tag the final state emitting parton by selecting the second jet in the event. We now want to check this hypothesis.

The existence of additional jets and the detector resolution (expecially the influence of the cracks see Chap. 3 sect. 1.3) are the main effects that could hide the correlation between the second jet and the third jet. We believe that these effects are small being respectively suppressed by additional powers of $\alpha_s$ and by the selection of the leading jets in the central calorimeter. We also believe that the amount of energy radiated by the final state, compared to that of the initial state,

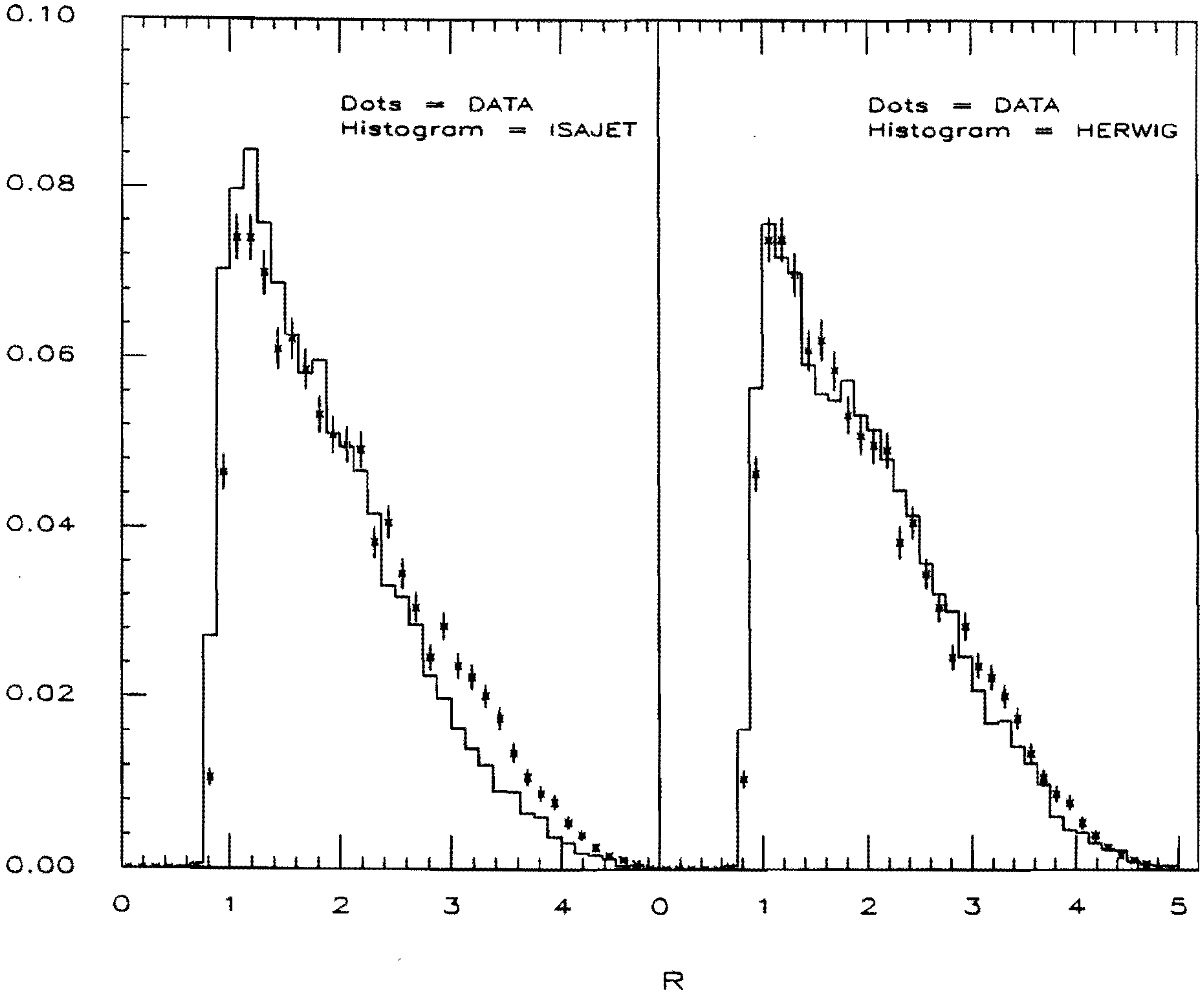

Fig. 5.18 — Projection on the R axis of the scatter plot of fig. 5.14b. Superimposed histograms are Montecarlo predictions

is large enough to give a sensible interference. These assumptions are confirmed by the shape of the distribution in fig. 5.18, peaked near the cluster boundary of the second jet, that shows the role of the second jet in the creation of the third one. We can verify this assertion, using the Montecarlos to understand which partons the third jet energy comes from.

To this purpose we define the variables $f_1$, $f_2$ as the fractions of third jet energy radiated by the final state parton respectively associated to the first and to the second jet. Fig. 5.19 shows the scatter plots $f_2 vs. R$ from the two Montecarlos. The event clusters in the regions with $f_2 \approx 1$ and $f_2 \approx 0$ indicate that most of the third jets fall in two categories: those essentially originated by radiation of the second jet, and those with negligible contribution from the second jet. Moreover the third jets belonging to the first category show a spatial correlation with the second jet, which is absent in the second category. This is even clearer in fig. 5.20, showing the $R$ distributions for the two categories: the solid line represents the jets with $f_2 < 0.35$ while the dotted line refers to jets with $f_2 > 0.35$.

As a check fig. 5.21 and fig. 5.22 show the scatter plot $f_1 vs. R'$ and the $R'$ distributions for third jets with $f_1 < 0.35$ and $f_1 > 0.35$ ($R'$ being now the distance from the first jet). It is clear that the contribution to third jets from radiation of the first jet is small. In summary we can state that:

- the contribution of the final state radiation to the third jets is relevant;
- we can tag the final state parton involved in the radiation of the third jet by selecting the second jet;
- the third jet radiated by the second jet shows a spatial correlation with the direction of the second jet.

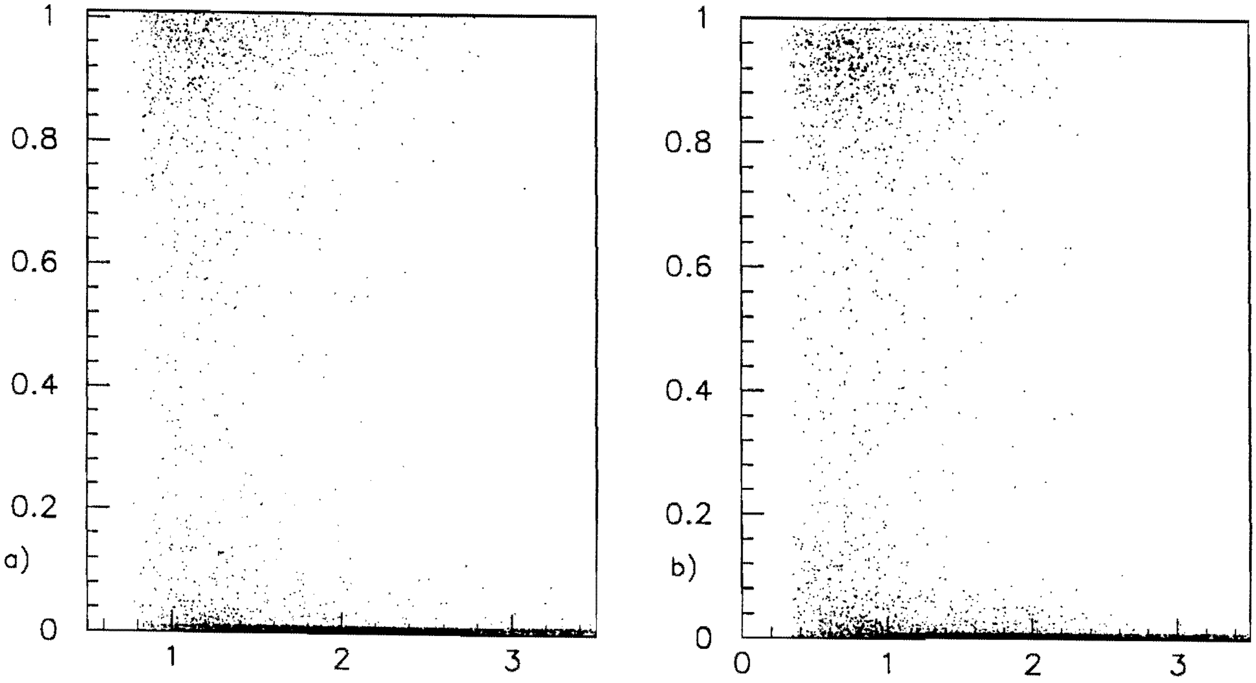

Fig. 5.19 – Scatter plots of $f_2$ vs. R for a)HERWIG and b) ISAJET

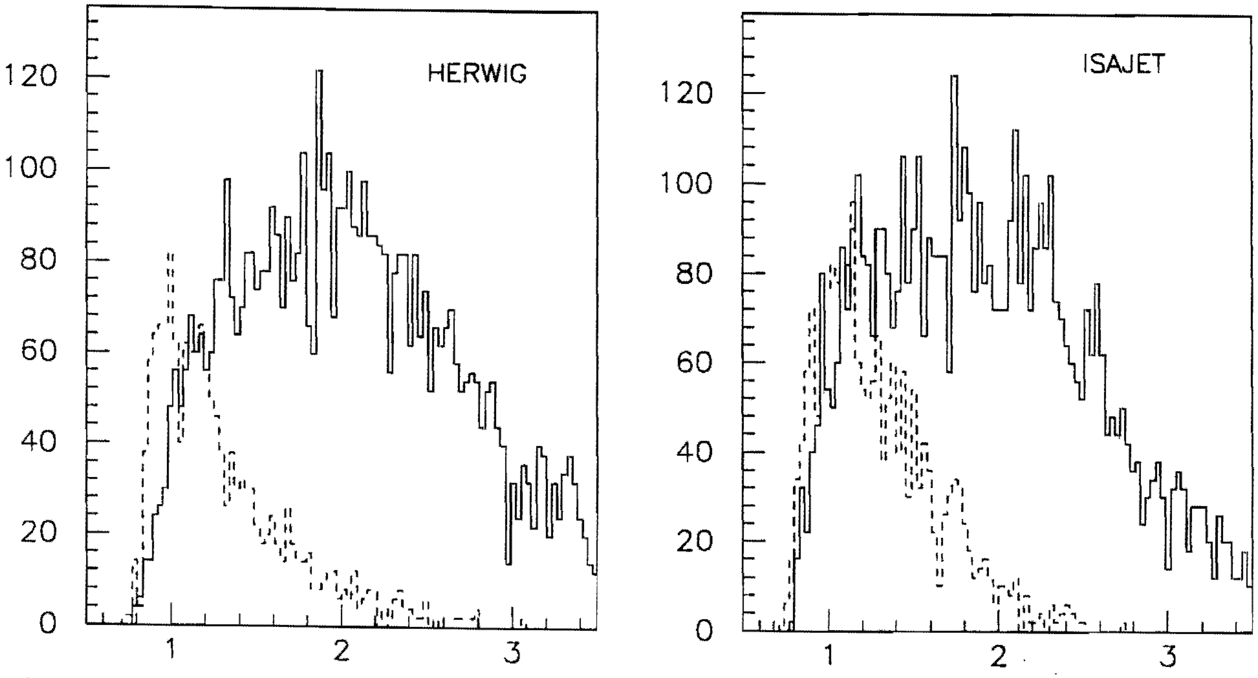

Fig. 5.20 – R distributions for $f_2<0.35$ (solid)and $f_2>0.35$ (dotted).

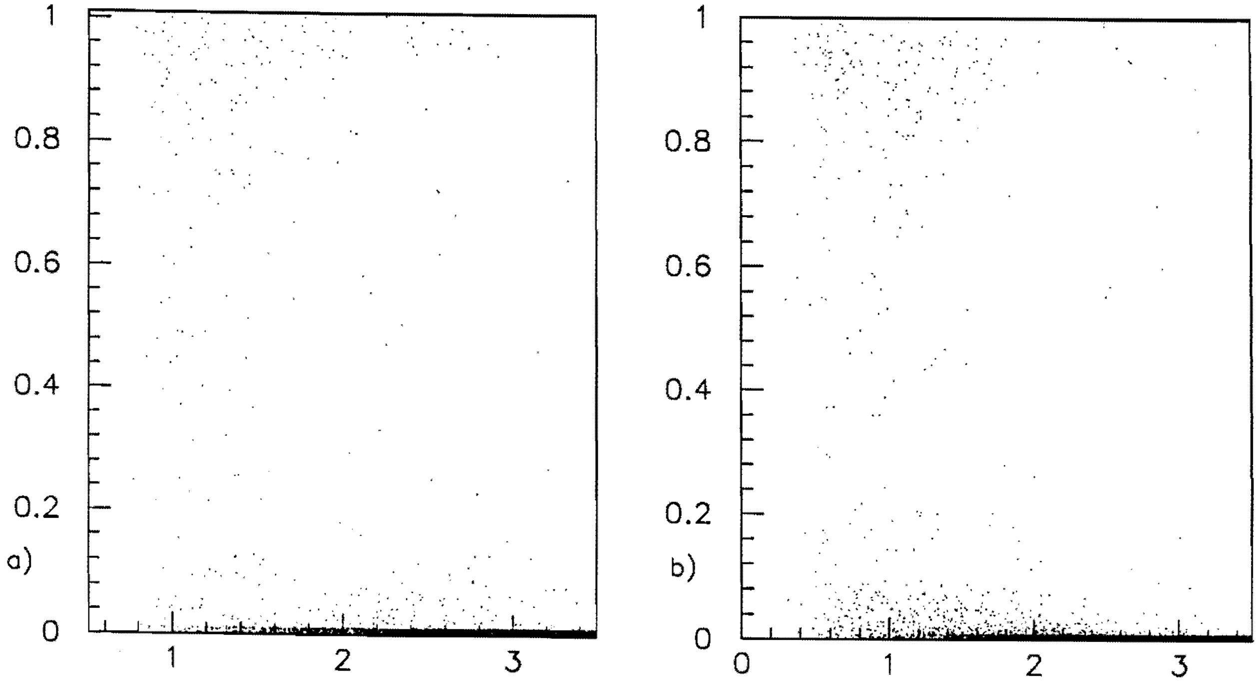

Fig. 5.21 – Scatter plots of $f_1$ vs. $R'$ for a) HERWIG and b) ISAJET

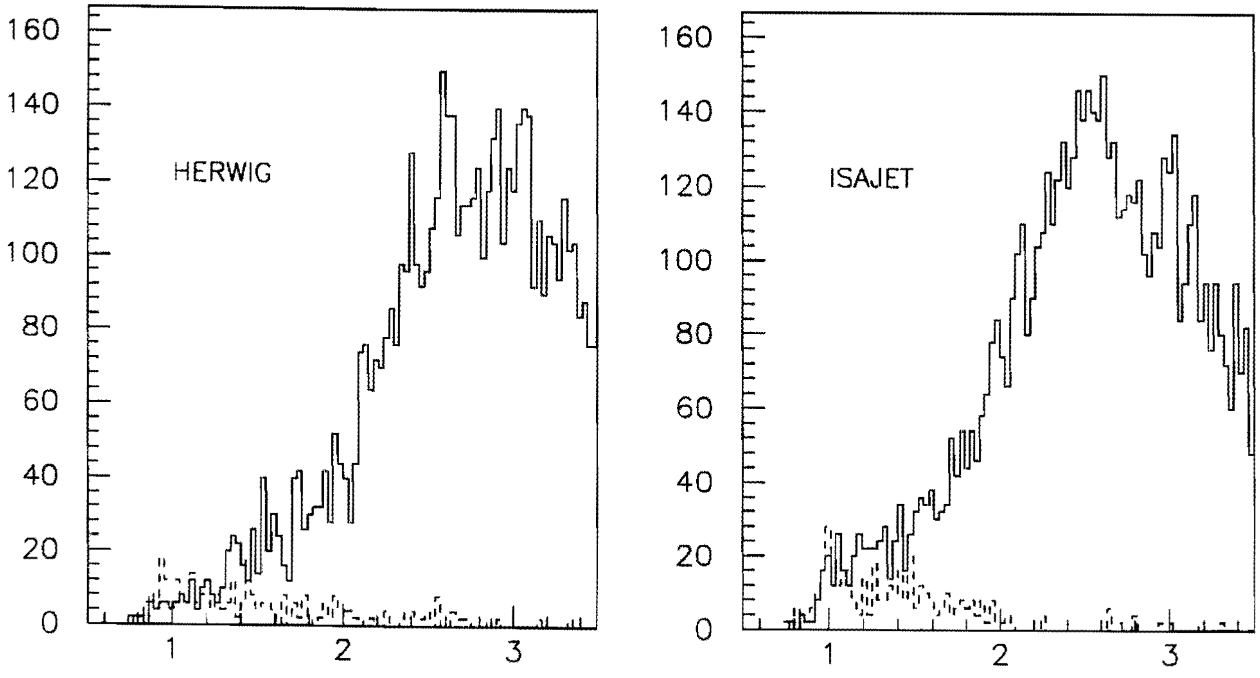

Fig. 5.22 – $R'$ distributions for $f_1<0.35$ (solid) and $f_1>0.35$ (dotted).

### 5.2.6 A variable sensitive to the colour interference

To complete the study of the third jet angular distribution, we examine now the variable $\alpha$ (complementary to $R$) of fig. 5.15b) Before looking at the $\alpha$ distribution we want to cut a rectangular region of uniform acceptance in the scatter plot $R$ vs. $\alpha$. We choose from fig. 5.18 $R > 1.1$ to get rid of the sharp rise due to the clustering algorithm. We also require $R < \pi$ to discard the upper region of $\alpha$ depending acceptance in fig. 5.15b). In fig. 5.23 we plot the $\alpha$ distribution for the jets with $1.1 < R < \pi$. This plot starts with a general decrease from left to right and, as $\alpha \rightarrow \pi/2$, a density enhancement results in a change of slope.

We note that $\alpha = \pi/2$ (that is $\Phi = 0$ and $H > 0$) corresponds to the third jet being on the half plane defined by the second jet and the beam axis ($\Phi = 0$) and in the convex region between the second jet and the beam axis, ($H > 0$). As stated in sect. 5.1.2 this region is probably favored by colour interference. In conclusion we expect that some excess of events for $\alpha \rightarrow \pi/2$ is the desired detectable feature of the interference. To confirm this hypotesis we need to compare the data with the Montecarlo predictions, looking for differences betwen Isajet and Herwig.

### 5.2.7 Comparison of the measured $\alpha$ distribution with the Herwig and Isajet simulations

We now turn to compare our experimental $\alpha$ distribution to Isajet and Herwig predictions. This should allow us to highlight interference effects which, as already said, Herwig takes into account while Isajet does not.

In fig. 5.24 we plot the $\alpha$ distributions (for jets with $1.1 < R < \pi$) from Isajet and Herwig. The qualitative agreement is much better between Herwig and data, while Isajet shows a behaviour which is seemingly incompatible to those of Herwig and of the data as well. Herwig reproduces the change of slope and the rise shown by the data in the region $\alpha > 0$, while the Isajet distribution is monotonically decreasing from $\alpha = -\pi/2$ to $\alpha = \pi/2$. To put the comparison to the data on a

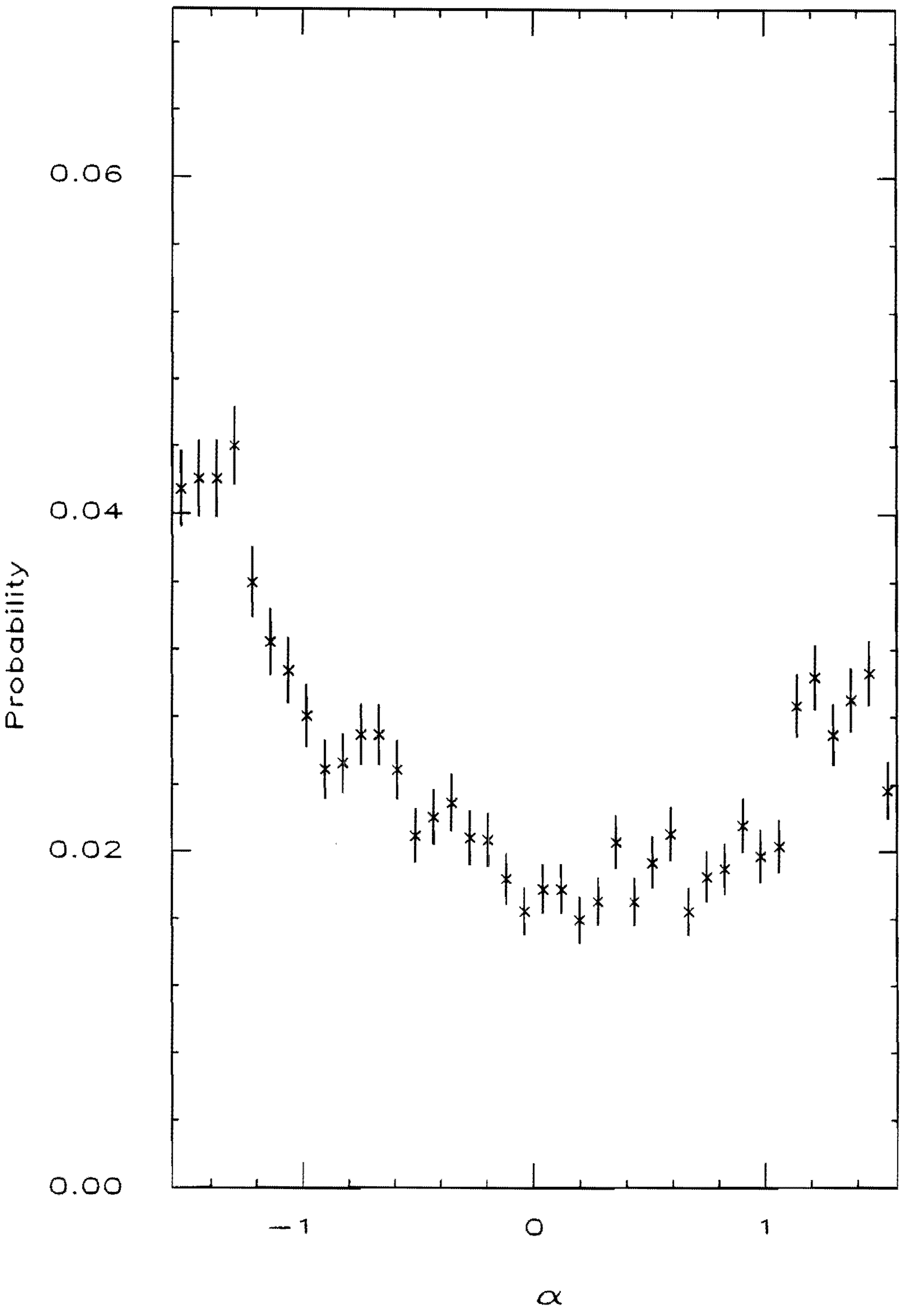

Fig. 5.23 — α distribution for 3rd jets with 1.1<R<π.

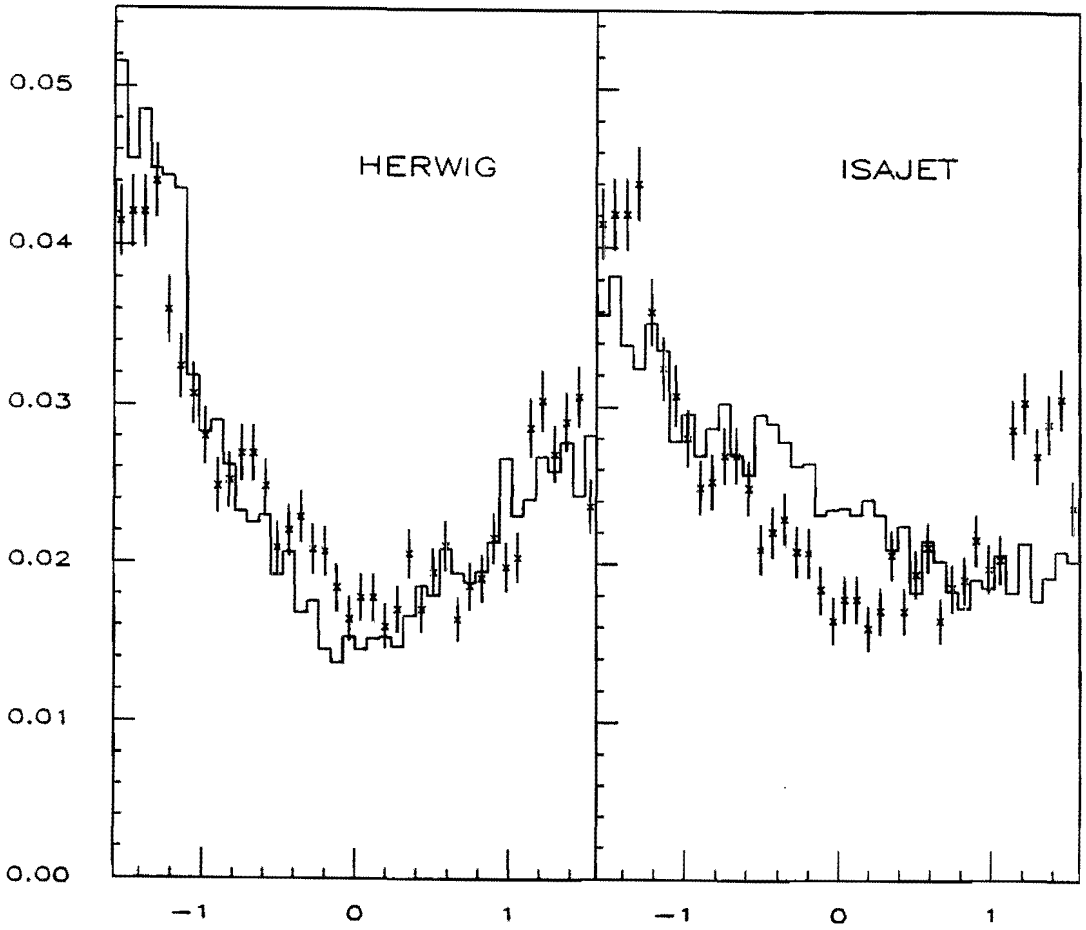

Fig. 5.24 — $\alpha$ distributions for HERWIG and ISAJET (histograms) superimposed to the data (points).

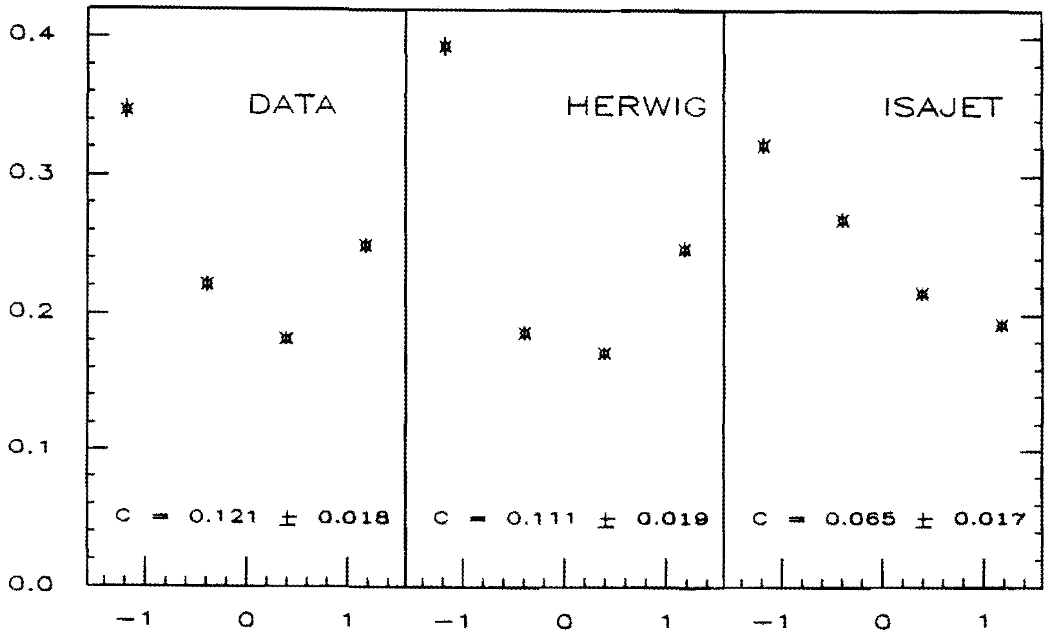

Fig. 5.25 — 4−bin $\alpha$ distributions

numerical ground, we calculate the $\chi^2$'s for both Isajet and Herwig distributions. The results are:

Isajet - data: $\chi^2 = 223.0$ (40 points)

Herwig - data: $\chi^2 = 107.8$ (40 points)

Although Herwig unequivocally gives a better agreement than Isajet, the $\chi^2$ is still poor, marking failure in the exact reproduction of the shape details in the $\alpha$ distribution. (In particular a careful comparison of the plots of fig. 5.24 suggests that the greatest contribution to the $\chi^2$ of Herwig comes from the first few bins on the left side). This fault might indicate some inadequacy in the physical description of the Montecarlo. For instance one of the sources of the discrepancy could be the fact that LLA does not account for all the NLO diagrams, which are relevant in generating the third jet [80]. Additional examples of potential sources of distortion for the $\alpha$ distribution are inaccuracies of the detector simulation on one side, and insufficient approximations to the proton structure functions on the other side. Nonetheless, the slope change is a sensible property reproduced by Herwig and the different $\chi^2$ values for the two Montecarlos, indicating that the overall behaviour of the $\alpha$ distribution is better simulated by Herwig, reasonably support the inference that the data rise for $\alpha \to \pi/2$ is attributable to colour interference.

To put in evidence the variation in slope as $\alpha \to \pi/2$, the original plot binning of the $\alpha$ distribution was reduced to 4 bins in fig. 5.25. The quantity $C$ (remindful of "convexity"):

$$C = \frac{(bin(4) - bin(3)) - (bin(3) - bin(2))}{bin(2) + bin(3) + bin(4)}$$

was then evaluated for the three samples. This gives an estimate of the change in slope, being essentially proportional to the second derivative of the distribution. We find:

Data: $C = 0.121 \pm 0.018$

Isajet: $C = 0.065 \pm 0.017$

Herwig: $C = 0.111 \pm 0.019$

$C$ values for Herwig and data are in good agreement, while Isajet yields a different value.

### 5.2.8 Sensitivity to $R_{cone}$ and to the $\Delta\phi$ cut

A question we left unsolved concerned the effects of changes in the cone radius of the clustering algorithm on our observation. In fact, rising the value of $R_{cone}$, should result in a more inclusive clustering algorithm, which would then be less sensible to radiation effects. To probe the sensitivity of our effect to this parameter we used the same simulated and data samples produced with $R_{cone} = 0.4$ and $R_{cone} = 1.0$ in the clustering algorithm.

We then derived the new $E_t$ thresholds for the first jet in the event, to avoid the trigger bias. We select $E_{t1} > 130$ GeV for the sample obtained with the cone size 1.0 and $E_{t1} > 100$ GeV for the sample of cone size 0.4.

Then the cuts on the distance $R$ between the $3^{rd}$ and $2^{nd}$ jets are adjusted taking into account the different bias introduced by the clustering algorithm when different cone sizes are adopted. Clearly the cone size 0.4 has the advantage of a smaller leading jet phase space occupancy, causing more space available to the third jet. Following the same criteria described in sect. 5.2.6 we choose $R > 0.6$ for the cone 0.4 sample and $R > 1.6$ for the cone 1.0 sample. The $\alpha$ distributions for these values appear in fig. 5.26: superimposed to the data points are the two Montecarlos. We see a much better agreement of Herwig than Isajet to the data points for both values of $R_{cone}$; again as pointed out above the most striking disagreement between Isajet and data is found in the region $\alpha \to \pi/2$. Values of $\chi^2$ for comparison of Montecarlo to data distribution, for the two values of cone size, are found in tab. 5.2.

| **Cone size** | **Herwig** | **Isajet** | **points** |
|---|---|---|---|
| 0.4 | $\chi^2 = 56.0$ | $\chi^2 = 138.9$ | 40 |
| 1.0 | $\chi^2 = 48.7$ | $\chi^2 = 162.1$ | 40 |

Table 5.2: $\chi^2$ for comparison of Montecarlo $\alpha$ distributions to data distributions

Observing the distributions for cone size 1.0 we note a strong depletion around $\alpha = 0$, which corresponds to $\Delta\eta = 0$, that is a second and third jet with the same rapidity. Since using a cone size $R = 1.0$ in the clustering algorithm the phase space influenced by a jet is extended up to $R = 1.6$ and because the two leading jets are constrained to be close in rapidity from the request $|\eta_1|, |\eta_2| < 0.7$ (see sect. 2.3 of Chap. 3), the central region is depleted by the two big cones belonging to the leading jets and little room is left for a third jet.

Fig. 5.27 shows the dependence of $C$ from $R_{cone}$. While Isajet fails in predicting the values of $C$, Herwig gives acceptable values (the first point is out less than two standard deviations).

We now come to check the dependence on $\Delta\phi_{cut}$, described in sect. 2.2 of Chap. 3. In fig. 5.28 the values of $C$ for different values of $\Delta\phi_{cut}$ are shown for both data and simulations. The lowering of the statistics does not allow to go down to angles smaller than $5^o$. The value of $C$ observed in the data increases at small $\Delta\phi_{cut}$. A tentative interpretation is that demanding approximate collinearity of the leading jets in the transverse plane favours the third jets which are also collinear in the transverse plane. These jets fall near the plane containing the second jet and the beam, where we expect our interference pattern to be more evident.

To conclude, the important issue is that the observed pattern of data and Herwig points, which are in remarkable agreement, makes us gain confidence in our interpretation, when compared to the much different behaviour of Isajet points.

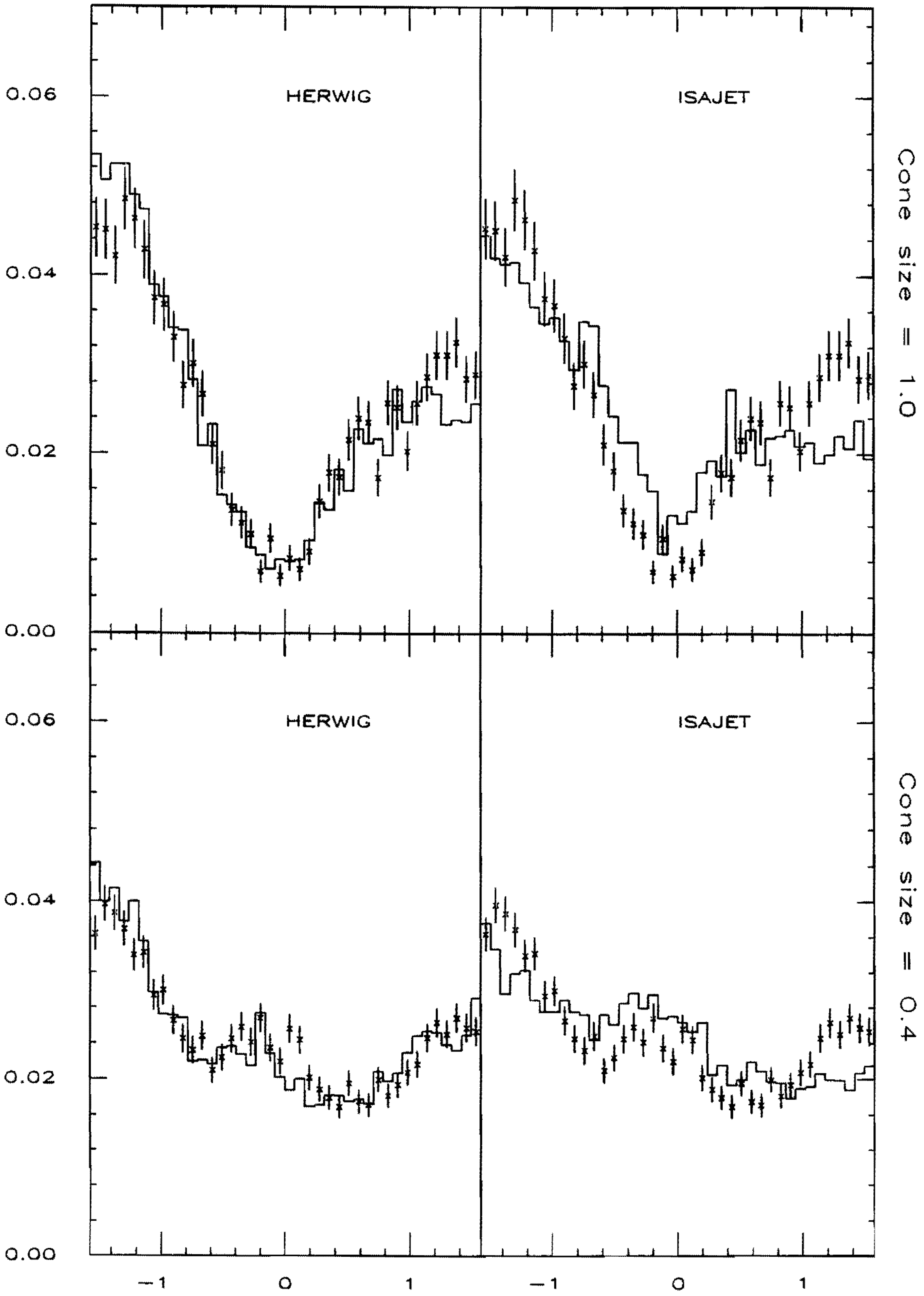

Fig. 5.26 — $\alpha$ distributions for different cone sizes Montecarlo predictions (histograms) are superimposed to the data (points).

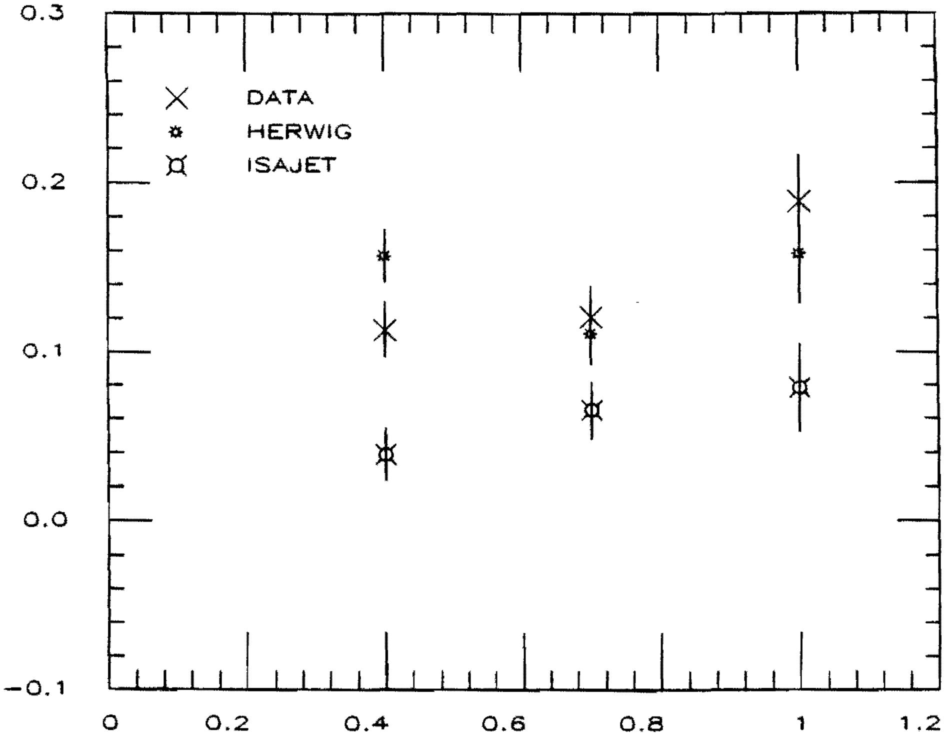

Fig. 5.27 — $R_{cone}$ dependence of C

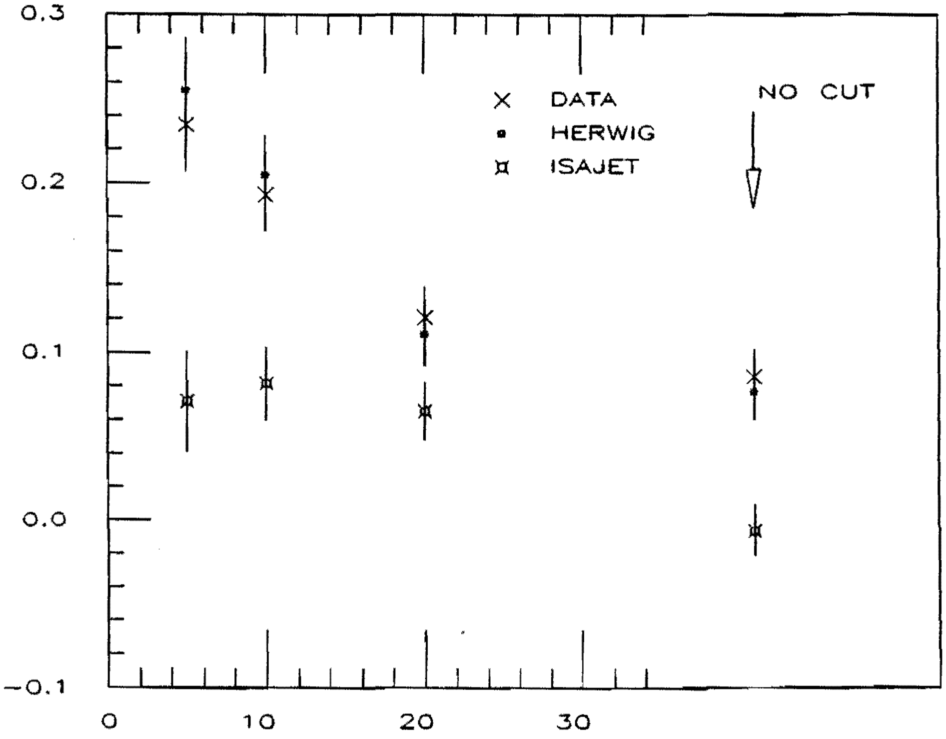

Fig. 5.28 — $\Delta\varphi_{cut}$ dependence of C

### 5.2.9 Selection of coherent and incoherent hard subprocesses: $\alpha$ distributions for selected samples

We have so far shown that Herwig reproduces much better some features of the $\alpha$ distribution then Isajet does. It could however be argued that the discrepancies found between the predictions of the two Montecarlos might be attributed to something else than interference, say e.g. other differences in the implementation of the LLA not directly connected with interference itself. Here we try to answer these questions by looking more deeply into the Herwig sample.

As explained in section 5.1 the hard subprocesses may or may not present initial-final state interference depending on the colour configurations available for each of them. In particular a coherent colour line is to be traced from the initial state to the final state in order for the interference to take place. To check our hypotesis which attributes the peculiar behaviour of the $\alpha$ distribution to interference effects, we separated the Herwig events in two samples. The first sample contains the events with a colour line connecting the initial to the final state (*coherent sample*). The second sample contains the remaining events (*incoherent sample*). The events with a colour line connecting the initial to the final state are easily identified by the existence in the event of at least one particle (colour singlet) that is generated by the combination of two quarks, of which the first is produced in the shower development of the initial state and the second in the shower of the final state (see fig. 5.29) [73]. The incoherent sample was thus selected by requiring that no such particles are present in the event, using the Montecarlo information on the particle "parents".

The two subsamples were then analyzed separately. After application of exactly the same cuts used before, the 4-bin $\alpha$ distributions of fig. 5.30 were obtained for a) coherent and b) incoherent subsample respectively. As expected we have a completely different behaviour in the two subsamples. The incoherent sample distribution does not show the raise for $\alpha \to \pi/2$ and its behaviour is close to that

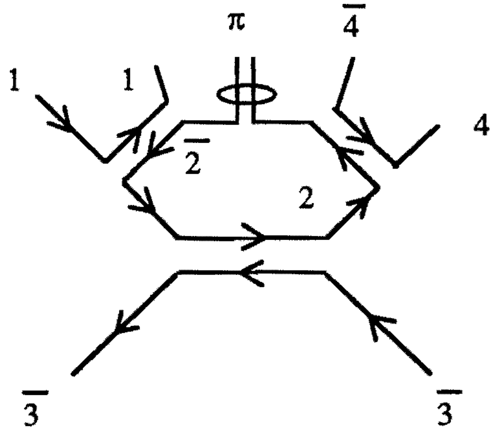

Figure 5.29: If the event has a colour line connecting the initial to the final state, at least one particle is generated from two quarks one of which is produced in the shower evolution of the initial state and the other in the shower evolution of the final state

of Isajet (superimposed as histogram in the figure). The overall behaviour of the coherent subsample distribution is clearly not compatible with Isajet. Selecting the Herwig events, on the basis of the gluons (g) and quarks (q) involved in the 2 → 2 process, gave the number of events summarized in tab. 5.3. This amounts to saying that most of the coherent sample involves gluons, as expected. A question might then arise if our coherent/incoherent selection does not simply take into account the different dynamical behaviour of gluons with respect to quarks. To answer the above question we took on a separate study of quark-only events, applying again our criteria for the selection of the coherent sample.

After application of all the usual cuts, the 4-bin $\alpha$ distribution of fig. 5.31 was obtained. Again the Isajet distribution of the quark-only subsample is superimposed as histogram. Comparing fig. 5.31 to fig. 5.30 we find a general agreement of the $\alpha$ distribution of the quark-only coherent subsample to that obtained from the full coherent subsample.

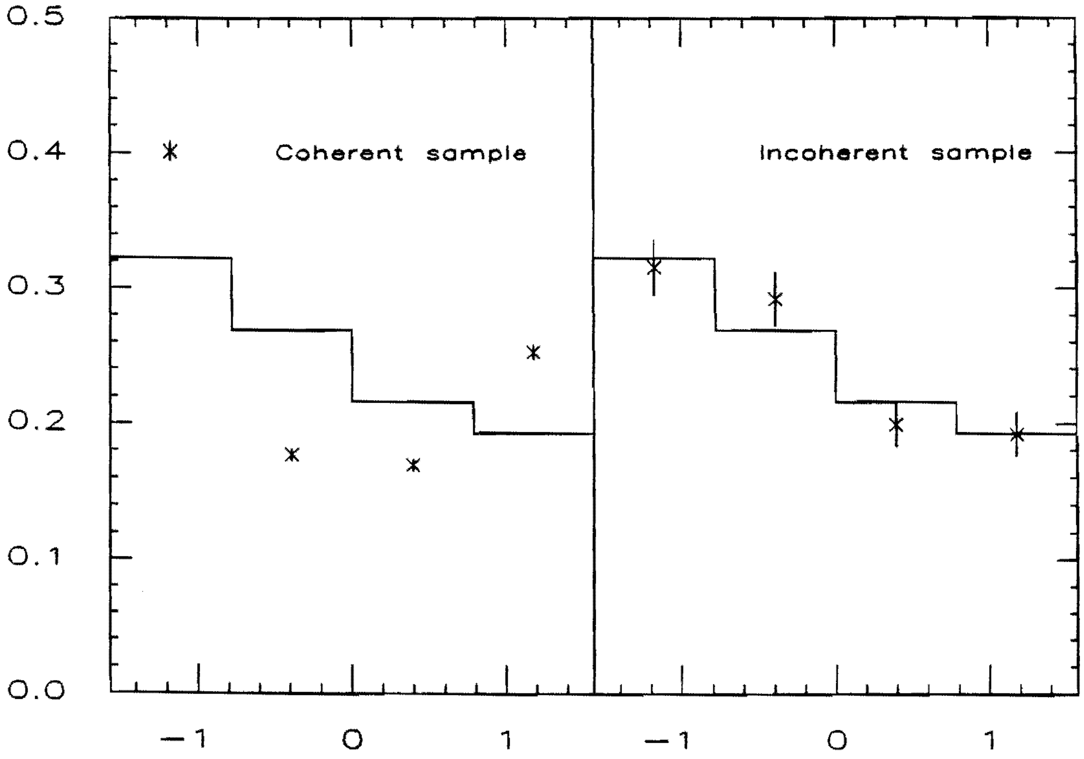

Fig. 5.30 — 4—bin $\alpha$ distributions of $3^{rd}$ jets for coherent/incoherent events from HERWIG. ISAJET prediction is superimposed as histogram

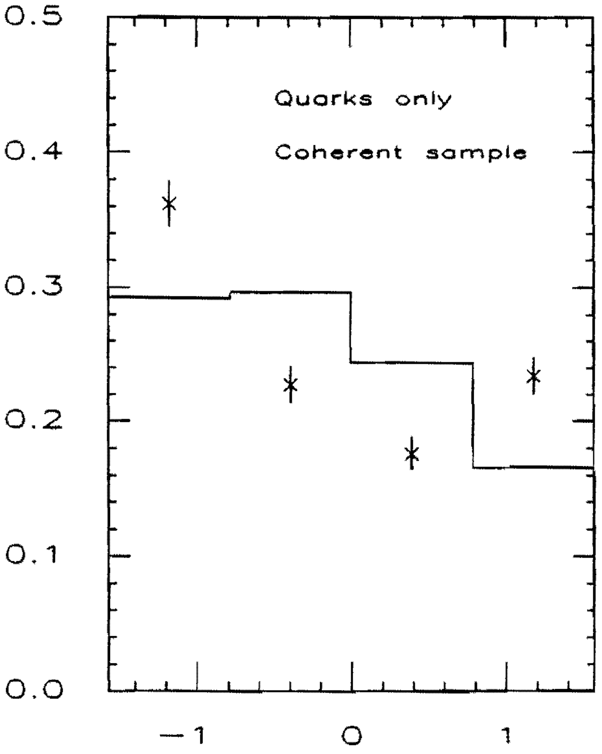

Fig. 5.31 — 4—bin $\alpha$ distributions of $3^{rd}$ jets for quark—only, coherent events from HERWIG. ISAJET prediction is superimposed as histogram.

| *Subprocess* | *Coherent sample* | *Incoherent sample* |
|---|---|---|
| $gg \to gg$ | 4360 | 0 |
| $gq \to gq$ | 6157 | 0 |
| $gg \to qq$ | 327 | 0 |
| $qq \to gg$ | 77 | 0 |
| $qq \to qq$ | 691 | 1316 |
| Total | 11612 | 1316 |

Table 5.3: Subprocesses frequencies in the *coherent* and *incoherent* subsamples

### 5.2.10 Pseudorapidity of the third jet

Looking at fig. 5.24 we observe that Isajet has a systematic eccess of third jets for $\alpha = 0$, while in the regions $\alpha = \pm\pi/2$ the third jet density is systematically depleted compared to the data. The region $\alpha = 0$ corresponds to $H = 0$, that is $\eta_3 = \eta_2$. This means that the third jet is confined to the central calorimeter because the second jet is required to stay there. The region $\alpha = \pm\pi/2$, instead, corresponds to $\Phi = 0$, that is $\phi_3 = \phi_2$ and $R = H$. Because the third jet must fall outside the clustering cone around the second jet, it is constrained in this case to have a pseudorapidity distance from the second at least equal to the cone radius. Then for $\alpha = \pm\pi/2$ non central rapidities are clearly favorite. We come to the conclusion that the difference in fig. 5.12 between the third jet $\eta$ distribution simulated by Isajet and that of the data could be mainly due to the effect of the colour interference. To double check this conclusion we look at the third jet $\eta$ distribution of the Herwig incoherent sample. Fig. 5.32 shows that the third jets of the incoherent sample are really distributed like those of Isajet. Summarizing: the results of this section strongly suggest that the interference cannot be neglected to correctly describe the pseudorapidity distribution of the third jet.

### 5.2.11 Quarks and gluons in the $\alpha$ spectrum

Since the variable $\alpha$ has been shown to be sensitive to initial-final bremsstrahlung interference, and since we have shown in sect. 5.1.1 that the only hard processes

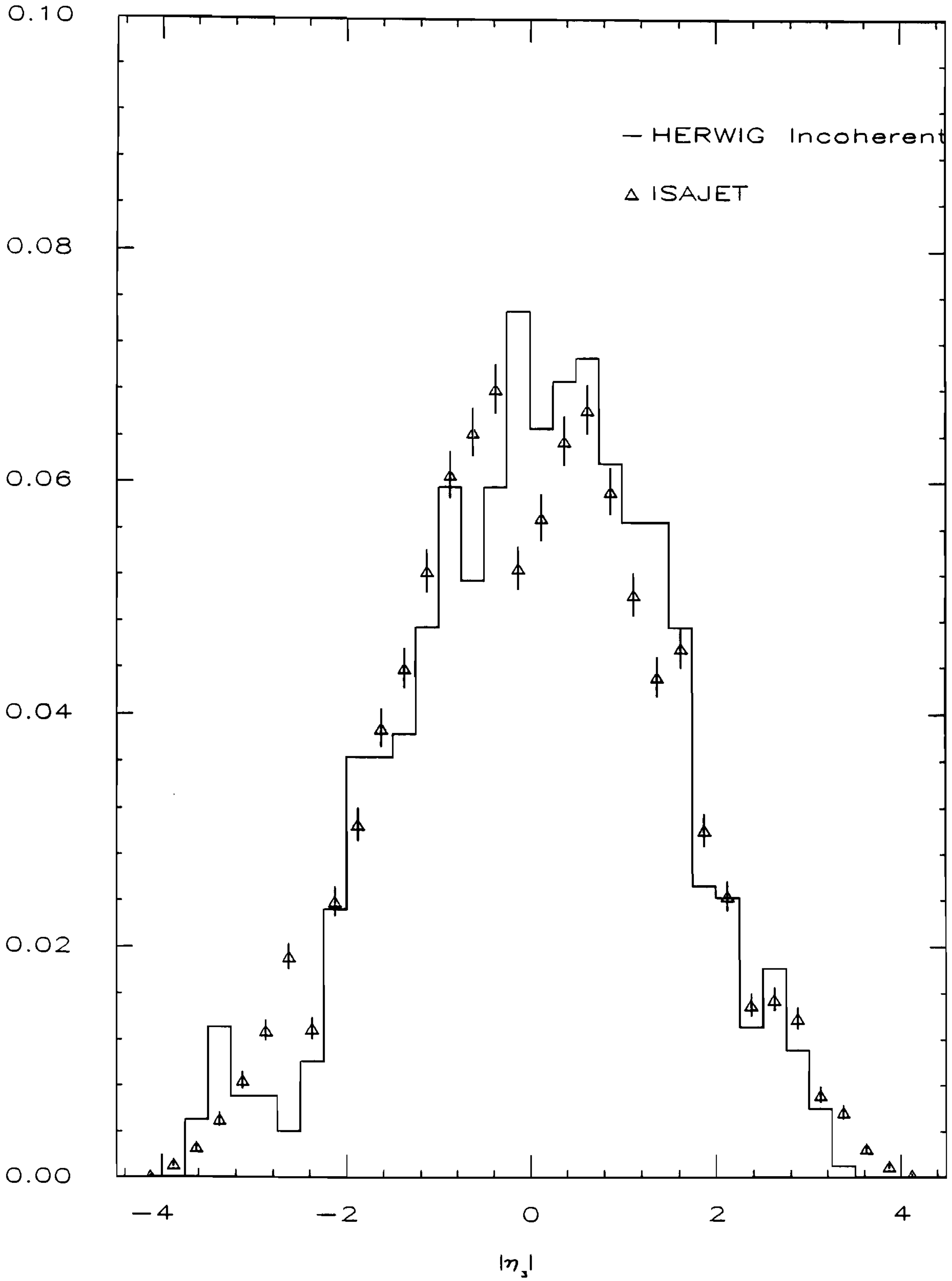

Fig. 5.32 — Pseudorapidity distribution of the third jets for the incoherent Herwig sample superimposed as histogram to the Isajet sample distribution.

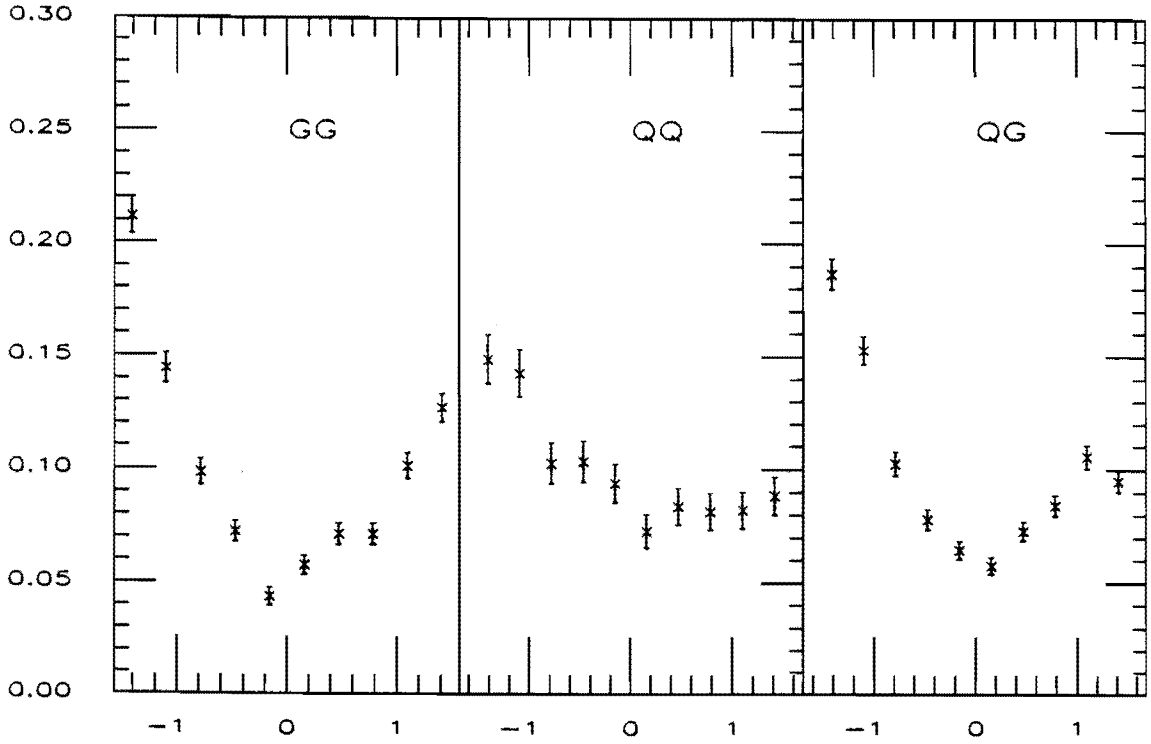

Fig. 5.33 — $\alpha$ distributions for different final states

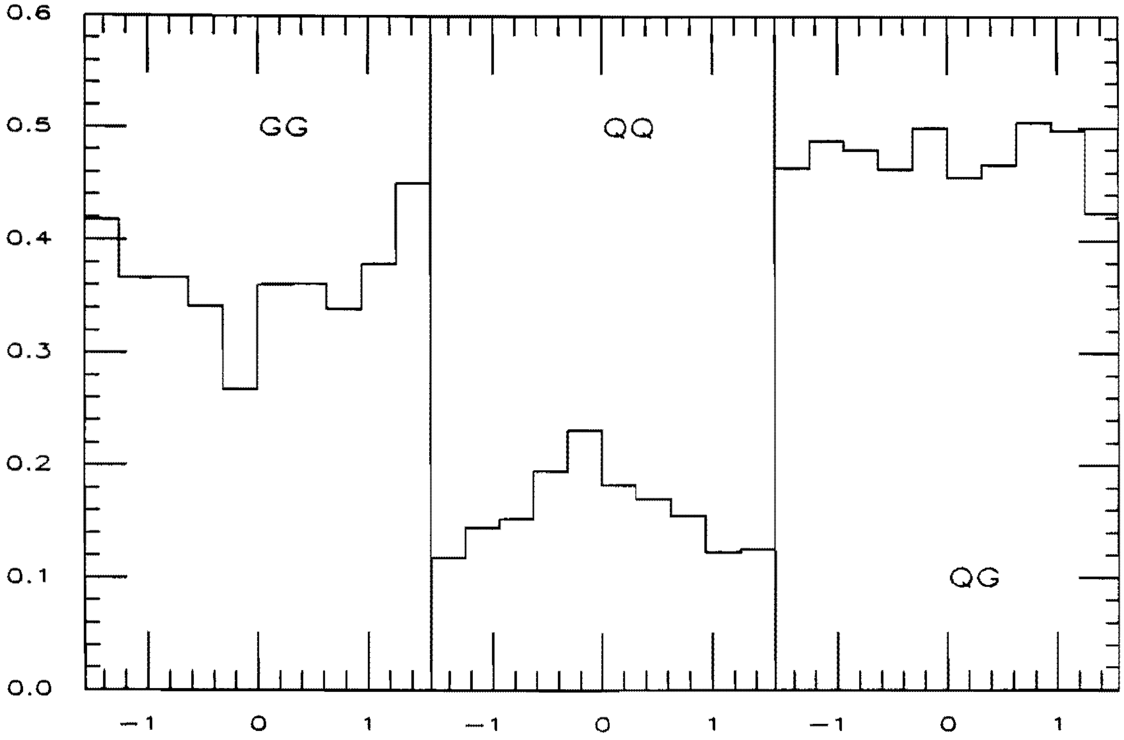

Fig. 5.34 — Gluon and quark event fractions in the $\alpha$ distribution.

for which this interference is absent are quark-only scatterings, an attemp can be made to use $\alpha$ as a tool to enhance the quark content in jet events. In the plots of fig. 5.33 the $\alpha$ distributions for different final states of the Herwig sample are shown, normalized to unit area. Because of incoherent processes the central plot for qq final state shows a patent difference with the other two plots for gg and qg final states. Fig. 5.34 shows, as functions of $\alpha$, the fractions of events for gg, qq, and qg final states respectively. From these histograms we can conclude that in the region around $\alpha = 0$ our sample is enriched in qq final state events and is depleted in gg final states.

## 5.3 Conclusions

Our starting hypotesis was that enhancement of third jet density in certain regions of phase-space will occur due to colour interference. This is consistent with differences found between Isajet and Herwig predictions, in that the second shows a positive slope for $\alpha \to \pi/2$ in the $\alpha$ distribution while the first does not. Since the data sample $\alpha$ distribution does turn on a positive slope for $\alpha \to \pi/2$, and the change in slope is consistent with Herwig predictions, we conclude that the expected enhancement due to colour interference is in fact observed experimentally. The study of Herwig coherent and incoherent subsamples indicates that the raise for $\alpha \to \pi/2$ is a characteristic pattern of the initial-final bremsstrahlung interference as implemented in Herwig. It disappears when selecting events coloured in such a way as to destroy the interference. The pseudorapidity distribution of the third jet is also sensitive to the phase space reduction operated by Herwig to take into account the colour interference. Because of the different colour pattern generated by quarks and gluons, the variable $\alpha$ can also be used as a tool to enhance the quark content in jet events.

# Bibliography

[1] P. A. M. Dirac, *Proceedings of the Royal Society of London*, **A 114**, 243 (1927).

[2] S. L. Glashow, Nucl. Phys. **22**,579 (1961);

S. Weinberg, Phys. Rev. Lett.**19**, 1264 (1967);

A. Salam, Nobel Symposium **8**, *edited by* N. Svartholm - Stockholm, Almqvist and Wiksell (1968), p. 367.

[3] W. A. Bardeen, H. Fritzsch and M. Gell-Mann in *Scale and Conformal Symmetry in Hadron Physics* ed. by R. Gatto, Wiley - New York (1973)

D. J. Gross and F. Wilczek, Phys. Rev. **D8**, 3633 (1973)

S. Weinberg, Phys. Rev. Lett.**31**, 494 (1973)

[4] H. D. Politzer, Phys. Rev. Lett.**30**, 1346 (1973);

D. J. Gross and F. A. Wiclzek, Phys. Rev. Lett.**30**, 1343 (1973);

[5] H. Fritzsch, M. Gell-Mann, and H. Leutwyler, Phys. Lett. **B47**, 365 (1973).

[6] H. D. Politzer, Phys. Rep. **14C**, 129 (1974).

[7] Deep inelastic electron-nucleon scattering experiments at SLAC are described in:

A. Bodek *et al.* , Phys. Rev. **D20**, 1471 (1979)

Neutrino-nucleon scattering experiment at CERN are described in:

H. Abramowicz *et al.* , Z. Phys. **C13**, 199 (1982)

H. Abramowicz *et al.* , Z. Phys. **C17**, 283 (1983)

The theory of DIS is discussed in:

J. D. Bjorken, Phys. Rev. **D5** (179), 1547 (1969);

R. P. Feynman, Phys. Rev. Lett.**23**, 1415 (1969);

S. Berman, J. D. Bjorken and J. Kogut, Phys. Rev. **D11** (4), 4 (1971).

[8] R. P. Feynman, *Photon-Hadron Interactions* - W. A. Benjamin, (1972).

[9] V. Barger and R. Phillips, *Collider Physics*, Ch. 7 p.193 - Addison Wesley (1987).

[10] J. C. Collins, D. E. Soper and G. Sterman, *Factorization of hard processes in QCD* in "Perturbative QCD" ed. by E. Mueller - World Scientific - Singapore, p. 1

[11] R. K. Ellis *et al.* , Nucl. Phys. **B152**, 285 (1979)

[12] E. Eichten *et al.* Rev. of Mod. Phys. **56**, 579 (1984).

[13] G. Altarelli and G. Parisi, Nucl. Phys. **B126**, 298 (1977).

[14] D. Duke and J. Owens, Phys. Rev. **D30**, 49 (1984).

[15] M. Diemoz *et al.* , Z. Phys. **C39**, 21 (1988).

[16] P. N. Harriman *et al.* , Phys. Rev. **D42**, 798 (1990).

[17] W. Tung and J. G. Morfin, Fermilab PUB-90/74, IIT-PUB-90/11 (1990), to appear on Z. Phys.

[18] R. P. Feynman, *Quantum Electrodynamics* - Benjamin/Cummings (1961).

[19] B. L. Combridge, J. Kripfganz and J. Ranft, Phys. Lett. **B70**, 234 (1977).

[20] B. Hubbard, Ph.D. Thesis - University of California (1989)

[21] B. R. Webber, Nucl. Phys. **B238**, 492 (1984);

K. Konishi, A. Ukawa and G. Veneziano, Nucl. Phys. **B157**, 45 (1979).

[22] COJETS: R. odorico, Comp. Phys. Comm. **32**, 139 (1984);

BIGWIG: G. Marchesini and B. R. Webber, Nucl. Phys. **B238**, 1 (1984); B. R. Webber, Nucl. Phys. **B238**, 492 (1984);

PYTHIA: H.-U. Bengtsson and G. Ingelman, Comp. Phys. Comm. **34**, 251 (1985);

FIELDAJET: R. D. Field, Nucl. Phys. **B264**, 687 (1986);

ISAJET: F. Paige and S. D. Protopopescu, BNL-38034 (1986);

JETSET: T. Sjöstrand and M. Bengtsson, Comp. Phys. Comm. **43**, 367 (1987);

EUROJET: A. Ali, B. van Eijk and E. Pietarinen (see B. van Eijk thesis, Amsterdam (1987);

HERWIG: G. Marchesini and B. R. Webber, Nucl. Phys. **B310**, 461 (1988).

[23] also B. R. Webber, Ann. Rev. of Nucl. Sci. **36**, 253 (1986).

[24] J. Gunion and Z. Kunszt, Phys. Lett. **B161**, 333 (1985);

R. Kleiss and W. J. Stirling, Nucl. Phys. **B262**, 235 (1985);

S. Parke and T. Taylor, Nucl. Phys. **B269**, 410 (1986);

M. Mangano, S. Parke and Z. Xu, Nucl. Phys. **B298**, 653 (1988);

K. Hagiwara and D. Zeppenfeld, Nucl. Phys. **B313**, 560 (1989);

F. A. Berends, W. T. Giele and H. Kuijf, Nucl. Phys. **B321**, 39 (1989).

[25] C. J. Maxwell, Phys. Lett. **B192**, 190 (1987);

M. Mangano and S. J. Parke, Phys. Rev. **D39**, 758 (1989).

[26] F. A. Berends, W. T. Giele and H. Kuijf ,to be published on Phys. Lett **B**.

[27] R. K. Ellis and J. C. Sexton, Nucl. Phys. **B269**, 445 (1986)

[28] M. Aversa, P. Chiappetta, M. Greco and J.-M. Guillet, Phys. Lett. **B210**, 225 (1988);

S. Ellis, Z. Kunszt and D. Soper, Phys. Rev. Lett.**62**, 726 (1989);

S. Ellis, Z. Kunszt and D. Soper, Phys. Rev. **D40**, 2188 (1989).

[29] R. M. Harris, Ph.D. Thesis - University of California - Lawrence Berkeley Laboratory, (1989).

[30] R. D. St.Denis, Ph.D. Thesis - Harvard University, (1988).

[31] F. Abe *et al.* , Nucl. Inst. & Meth.**A271**, 387 (1988)

[32] L. Balka *et al.* , Nucl. Inst. & Meth.**A267**, 272 (1988).

R. G. Wagner *et al.* , Nucl. Inst. & Meth.**A267**, 330(1988).

[33] S. Bertolucci *et al.* , Nucl. Inst. & Meth.**A267**, 301 (1988).

[34] Y. Fukui *et al.* , Nucl. Inst. & Meth.**A267**, 280 (1988).

[35] C. Haber LBL/CDF 87-02, (1987).

[36] G. Brandenburg *et al.* , Nucl. Inst. & Meth.**A267**, 257 (1988);

[37] S. Cihangir *et al.* , Nucl. Inst. & Meth.**A267**, 249 (1988).

[38] F. Snider *et al.* , Nucl. Inst. & Meth.**A268**, 75 (1988).

[39] F. Bedeschi *et al.* , Nucl. Inst. & Meth.**A268**, 50 (1988).

[40] T. Liss CDF internal note 552, (1988).

[41] E. Barsotti *et al.* , Nucl. Inst. & Meth.**A269**, 82 (1988).

[42] D. Amidei *et al.* , Nucl. Inst. & Meth.**A269**, 51 (1988).

[43] E. Meschi, A. Tollestrup and H. Frisch., CDF internal note 764.

[44] See, for example, R. Cashmore, S. Ozaki, G. Trilling *et sequitur* in *Proceedings of the Workshop on Experiments, Detectors and Experimental Areas for the Supercollider*, July 7-17, 1987, Berkeley CA. - edited by R. Donaldson and G. Gilchrisie, World Scientific, Singapore (1988).

[45] In *Proceedings of the Workshop on Calorimetry for the SSC*, Tuscaloosa, AL, 1989 - edited by R. Donaldson and G. Gilchrisie, World Scientific, Singapore (1988).

[46] S. Ellis, Z. Kunszt, and D. Soper, Phys. Rev. **D40**, 2188 (1989); University of Oregon Preprints OITS 436 (1990).

[47] B. Flaugher and K. Meier - In *Proceedings of the 1990 Summer Study on High Energy Physics* - Research Directions for the Decade - Snowmass, CO., June 25 - July 13, 1990.

[48] F. Aversa, P. Chiappetta, M. Greco and J. Guillet, Phys. Lett. **B210**, 225 (1988)

[49] R. Ellis and J. Sexton Nucl. Phys. **B269** 445 (1986)

[50] G. Sterman and S. Weinberg, Phys. Rev. Lett.**39**, 1436 (1977);

S. Ellis *et al.* , Oregon Preprints OITS 395, 396 (1988)

[51] J. Alitti *et al.* , CERN Preprint CERN-PPE/90-105 (1990); submitted to Z. Phys. C.

[52] J. Huth *et al.* - In *Proceedings of the 1990 Summer Study on High Energy Physics* - Research Directions for the Decade - Snowmass, CO., June 25 - July 13, 1990.

[53] F. Abe *et al.* (CDF Collaboration), Phys. Rev. Lett.**62**, 613 (1988).

[54] P. Bagnaia *et al.* (UA2 Collaboration), Phys. Lett. **B144**, 283 (1984).

[55] A. Roodman, S. Behrends and M. Shapiro, CDF internal note 1344 (1991).

[56] S.Kuhlmann *et al.* , CDF internal note 686, (1988).

[57] B. Hubbard Ph.D. Thesis (november 1989) and Phys. Rev. Lett.**65** 8, 968 (1990).

[58] D. Brown and S. Kannappan, CDF internal note 873 (1989).

[59] M. Roach and S. Behrends, CDF internal note 1361 (1991).

[60] D. Brown, CDF internal note 835, 755, (1989);

B.Flaugher CDF internal note 1340, (1991).

[61] T. Hessing, CDF internal note 1247 (1991);

F. Abe *et al.* (CDF Collaboration), to be submitted to Phys. Rev. **D**

T. Hessing, Ph.D. Thesis - Texas A&M University, College Station (1990)

[62] D. Brown and M. Franklin, CDF internal note 811 (1988);

P. Hurst and M. Franklin, CDF internal note 847 (1988)

P. Hurst, M. Franklin and T. Kamon, CDF internal note 848 (1988)

T. Kamon, P. Hurst, M. Franklin and Y. Funayama, CDF internal note 900, (1989).

[63] S. Kuhlmann and J Yoh, CDF internal note 548 (1987)

T. Hessing, CDF internal note 957 (1989)

[64] T.Kamon CDF internal note 979 (1989)

[65] G. Redlinger and Y. D. Tsai, CDF internal note 521 (1987)

[66] A. Roodman, S. Behrends and M. Shapiro, CDF internal note 1344

[67] F. Abe *et al.* (CDF collaboration), Phys. Rev. Lett.**62**, 3020 (1989);

F. Abe *et al.* (CDF collaboration), Phys. Rev. Lett.**64**, 157 (1990);

P. Bagnaia *et al.* (UA2 Collaboration), Phys. Lett. **B138**, 1430 (1984);

F. Abe *et al.* (CDF collaboration), Phys. Rev. **D41**, 1722 (1990).

[68] S. Dell'Agnello *et al.* , CDF internal note 1058, (1989);

M. Dell'Orso *et al.* , CDF internal note 1378, (1991).

[69] M. Dell'Orso, P. Giannetti and M. Incagli, CDF internal note 1393, (1991).

[70] M. Dell'Orso and P. Giannetti, CDF internal note 1377, (1991).

[71] P. Giannetti In *Proceedings Les rencontres de la Vallee d'Aoste*, La Thuile - Italy (1991)

[72] S. D. Ellis *et al.* , ETH-TH/90-**3** (1990);

F. Aversa *et al.* , LNF-90/**012** PT (1990).

[73] The first Montecarlo to implement colour coherence was Bigwig described in: G. Marchesini and B. R. Webber, Nucl. Phys. **B238**, 1 (1984);

B. R. Webber, Nucl. Phys. **B238**, 492 (1984).

Herwig is described in: G. Marchesini and B. R. Webber, Nucl. Phys. **B310**, 461 (1988).

[74] R. K. Ellis. G. Marchesini and B. R. Webber, Nucl. Phys. **B286**, 643 (1987) and references therein.

[75] See for example R. L. Stratonovich, Topics in the theory of random noise - vol.1 Ch. 4 (1963); by Markov process we mean that at each branching of the shower development, the probability of gluon emission depends only on the immediately preceding branching.

[76] On the angular ordering to implement coherent branching in time-like evolution (final state evolution) see A. Bassetto, M. Ciafaloni and G. Marchesini, Phys. Rep. **100**(4), 201 (1983) and references therein.

[77] On the evolution of the space-like cascade see:

S. Catani, M.Ciafaloni and G. Marchesini, Nucl. Phys. **B264**, 588 (1986);

M. Ciafaloni, In Proceedings of the 23rd Int. Conf on High Energy Physics - Berkeley (1986)

[78] F. E. Paige and S. D. Protopopescu, BNL Report 37066.

[79] S. Dell'Agnello et al., CDF internal note 1055 (1989)

[80] M. Mangano, In *Proceedings of the 8th Workshop on Proton- Antiproton Collider Physics*, Castiglione della Pescaia (GR) (1989) and references therein.

[81] A. H. Mueller, Phys. Lett. 104B, 161 (1981); A. Bassetto et al. , Nucl. Phys. B207, 189 (1982); Yu. L. Dokshitzer et al. , Z. Phys. C15, 325 (1983); C18, 37 (1983).

[82] For a review on coherence effects in the physics of jets see:

Yu. L. Dokshitzer, V. A. Khoze and S. I. Troyan, Coherence and Physics of jets - In *Perturbative QCD*, ed. by A. Mueller - World Scientific - Singapore.